Katalysis LIKAT Leibniz-Institut für Katalyse e.V.

Universität Rostock

Traditio et Innovatio

2022

Influence of light on ad- and desorption processes on oxidic semiconductor surfaces

Einfluss von Licht auf Ad- und Desorptionsprozesse an oxidischen Halbleiteroberflächen

DISSERTATION

Zur Erlangung des akademischen Grades
doctor rerum naturalium (Dr. rer. nat.)

der mathematisch-naturwissenschaftlichen Fakultät der Universität Rostock

Eingereicht am 19.04.2022
Verteidigt am 18.10.2022
von

Pawel Naliwajko
Matrikel-Nr. 21800352
Geb. am 28. September 1991 in Sumy, Ukraine

https://doi.org/10.18453/rosdok_id00004025

I. Eidesstattliche Erklärung

Hiermit versichere ich, Pawel Naliwajko, an Eides statt, dass ich die vorliegende Arbeit eigenständig und nur unter Zuhilfenahme der im Quellen- und Literaturverzeichnis genannten Werke angefertigt habe. Jede Textpassage, die wörtlich oder dem Sinn nach auf fremdes Gedankengut zurückgreift, ist als solche kenntlich gemacht.

Rostock, 19.04.2022

Pawel Naliwajko

Dekan: Prof. Dr. Klaus Neymeyr

1. **Gutachter:**

Prof. Dr. rer. Nat. habil. Jennifer Strunk
Bereichsleiterin Heterogene Photokatalyse, Leibniz Institut für Katalyse e.V. Rostock
Professorin für Katalyse, MNF, Universität Rostock

2. **Gutachter:**

Prof. Dr. Guido Mul
Faculty of Science and Technology, Photokatalytic Synthesis
University of Twente

Jahr der Einreichung: 2022
Jahr der Verteidigung: 2022

II. Zusammenfassung

Der weltweit wachsende Energiebedarf und der ansteigende Gehalt an Kohlendioxid (CO_2) in der Atmosphäre: Das sind zwei der größten Probleme, denen wir uns heute stellen müssen. Erneuerbare Energien werden in diesem Zusammenhang seit der Ölkrise in den späten 1970er Jahren immer wichtiger. Für eine zuverlässige und konstante Nutzung von Erneuerbaren Energien muss jedoch das bestehende Energienetzwerk modernisiert, ausgebaut und optimiert werden. Die direkte Speicherung von Solarenergie durch die Nutzbarmachung – und die damit einhergehende Verminderung – des atmosphärischen CO_2 könnte eine Lösung für beide Probleme bedeuten. Metalloxid-basierte Halbleiter Materialien wie Zinkoxid (ZnO) und Titandioxid (TiO_2) haben sich in den letzten Jahrzehnten als mögliche Kandidaten für Katalysatoren – notwendig für die Energiekonversion – gezeigt. Neben der Umwandlung spielen Prozesse wie Adsorption und Desorption eine wichtige Rolle bei einer katalytischen Reaktion. Fouriertransformationsinfrarot-Spektroskopie (FT-IR) bietet die Möglichkeit molekulare Spezies, welche während der o.g. Prozesse auf der Oberfläche der Katalysatoren ausgebildet werden, zu untersuchen. Dies kann zum besseren Verständnis sowie Optimierung der Reaktionen beitragen. Obwohl das Feld rund um CO_2 Ad- und Desorption auf fast 100 Jahre Forschung zurückblickt, sind vor allem die Auswirkungen des Lichts auf diese Prozesse nicht vollständig erkundet. Eine umfassende Recherche in den Archiven aus der Mitte des 20. Jahrhundert deckte weitreichende Erkenntnisse von Wissenschaftlern aus der damaligen Sowjetunion über lichtinduzierte Ereignisse in metall-oxidischen Halbleitern auf. Des Weiteren wurde eine kritische Betrachtung der in der Literatur verfügbaren Interpretationen von FT-IR Untersuchungen angefertigt.

Das Ad- und Desorptionsverhalten von CO_2 unter Einfluss von Licht wurden auf verschiedenen ZnO, TiO_2 und $Ce_xZr_{1-x}O_2$ (Cer-zirkonium-oxid) Nanomaterialien mittels diffuser Reflexion FT-IR Spektroskopie sowie Temperatur programmierten Desorptionsmethode untersucht. Das Phänomen des „IR-Schwärzens“ wurde für ZnO als Resultat der Bestrahlung oder Erhitzung in reduktiver Atmosphäre beobachtet. Für ein besseres Verständnis der Ereignisse, denen die Interaktion von Phononen und Elektronen zugrunde liegt, wurde das Feld der theoretischen Festkörperphysik zur Rate gezogen. Kein direkter Einfluss der UV-Bestrahlung auf die Adsorption von CO_2 auf ZnO konnte festgestellt werden, da die Menge sowie das Desorptionsverhalten größtenteils unbeeinflusst blieben. Auf TiO_2 Materialien veränderte sich unter UV-Bestrahlung die Präferenz der ausgebildeten Spezies. So wurden auf Anatase vermehrt Carbonate sowie Bicarbonate – und auf P25 und m-TiO_2 Formatspezies – nachgewiesen. Bestrahlung von $Ce_xZr_{1-x}O_2$ zeigte keinen Einfluss auf das Desorptionsverhalten von CO_2.

III. Abstract

The worldwide growing energy demand alongside the increasing amount of carbon dioxide (CO_2) in the atmosphere: these are two of the biggest problems we must face today. In this context renewable energies became more important since the oil crisis in the late 1970s. However, for a reliable and constant utilization of renewable energies the existing energy network needs to be modernized, extended, and improved. The direct storage of solar energy utilizing – and thus decreasing – of atmospheric CO_2 is a possible solution for both problems. In the recent decades metal oxide-based semiconductor materials such as zinc oxide (ZnO) and titanium dioxide (TiO_2) have shown to be good contenders for catalysts needed for the energy conversion reactions. Besides the conversion, processes like adsorption and desorption play an important role during catalytic reactions. Fourier transformation infrared spectroscopy offers the possibility to investigate molecular species which are formed on the surface of the catalyst. This may lead to a better understanding and thus improvement of the conversion reaction. Although the field of CO_2 ad- and desorption features nearly 100 years of research history, the influence of light on the processes is not fully discovered.

An extensive literature research in the archives of early and mid-20th century revealed insights of researchers from the former Sowjet Union dealing with light induced events in metal oxidic semiconductors. Furthermore, a critical discussion of interpretations of research works by means of FT-IR spectroscopy available from the recent literature was prepared.

The ad- and desorption behavior of CO_2 under influence of light was investigated of different ZnO, TiO_2 and $Ce_xZr_{1-x}O_2$ (cerium zirconium oxide) nanomaterials by means of diffuse reflectance FT-IR spectroscopy as well as temperature programmed desorption method. The phenomenon of "IR-Blackening" was observed for ZnO upon irradiation or heating in reductive atmosphere. For a better understanding of the observations, which are caused by the interaction between phonons and electrons, the scientific field of theoretical physics was additionally studied.

No direct influence of UV-Irradiation on adsorption of CO_2 on ZnO was established, as the amount and the desorption behavior remained mostly unaffected.

On TiO_2 the preference for formation of surface species changed under irradiation. On Anatase increasingly carbonates and bicarbonates were formed, while P25 and m-TiO_2 materials showed additional formation of formate species.

Irradiation of $Ce_xZr_{1-x}O_2$ was found not to influence the desorption of CO_2.

IV. Danksagung

Zunächst möchte ich mich bei **Prof. Jennifer Strunk** für die Aufnahme in ihrer Forschungsgruppe der *heterogenen Photokatalyse*, sowie die Möglichkeit diese Arbeit dort anzufertigen, bedanken. Sie gab mir die Freiheiten den Bereich mit auf- und auszubauen und hatte stets Vertrauen in mich und meine Fähigkeiten.

Dr. Tim Peppel danke ich im besonders hohen Maße für die stets ins Ziel treffende Unterstützung sowohl auf fachlicher als auch auf persönlicher Ebene.

Dr. Nikolaos Moustakas, **Dr. Marcus Klahn** und **Dr. Alexander Zapf** danke ich für den kollegialen und warmen Umgang, aber auch ihre Ideen, Geschichten und Weisheiten, die Sie mit mir teilten.

Des Weiteren bedanke ich mich bei allen anderen Kollegen und Mitarbeitern des Fachbereiches für die angenehme Zusammenarbeit. Darüber hinaus danke ich **Dr. Sebastian Wohlrab** für die im Rahmen des Supreme Projekts stattgefundene wissenschaftliche Zusammenarbeit.

Weiterhin geht ein großer Dank an die technischen Mitarbeiter – insbesondere an **Andreas Hutter** und **Thomas Rall** – für deren schnelle und professionelle Unterstützung. Darüber hinaus danke ich dem analytischen Bereich für die Charakterisierung der angefertigten Materialien.

Meinem besten Freund **Dr. Jakob Böker** danke ich für die große Hilfestellung mit Literaturhinweisen, aber auch Rat und Tat bei der Erarbeitung des Feldes der theoretischen Festkörperphysik. Darüber hinaus haben mir Spielesitzungen und Unterhaltungen mit ihm, aber auch mit **Damian Schiller** den einen oder anderen Abend sehr versüßt.

Generell danke ich all meinen Freunden in Bochum, die trotz meines Exils in Rostock, zu mir gehalten haben.

Weiterhin danke ich **Julius Zimmermann** für die Freundschaft, die wir in Rostock geknüpft haben. Die Diskussionen über unsere Arbeiten, die Welt und das richtige Mindset waren stets eine Bereicherung.

Der wohl wichtigste Dank geht an meine Eltern für all ihren Mut und Stärke, die sie aufbrachten, um all die Einschränkungen und Hürden zu überwinden, um meiner Schwester und mir eine bessere Zukunft zu ermöglichen. Natürlich danke ich meiner Schwester dafür, dass sie einfach ein toller Mensch und eine super Schwester ist. Ihrem Mann und seinen Eltern danke ich für die stetige Unterstützung und das Vertrauen, dass sie in mich hatten – mit ihnen ist unsere Familie größer geworden.

Zuletzt bedanke ich mich bei meiner Madame Elisabeth für ihr großes Herz und all die Liebe, die sie mir entgegenbringt. Dank ihr war alles EZ.

V. Content

1 INTRODUCTION 1

2 THEORY AND STATE OF THE ART 5

2.1 ZnO 5

2.2 A Brief dive into solid-state physics 8

2.2.1 Reciprocal lattice and k-space 8

2.2.2 Electronic band structure of semiconductors 9

2.2.3 Plasmons 11

2.2.4 Phonons 12

2.2.5 Interaction of phonons with other particles 14

2.2.6 Link to macroscopic reality 15

2.3 CO_2 adsorption on metal oxide-based materials 17

2.3.1 Investigation of CO_2 adsorption by means of FT-IR Spectroscopy 20

2.4 Side note: photocatalytic CO_2 reduction 26

2.5 Thermal and Photo-induced effects on ZnO: 28

2.5.1 Introduction 28

2.5.2 Early sorption experiments on ZnO 29

2.5.3 Photogalvanic effects in ZnO 32

2.5.4 Influence of UV irradiation on the IR spectrum 32

2.5.5 Influence of UV irradiation on the adsorbate bond strength 34

2.5.6 Detecting and distinguishing oxygen surface species 34

2.5.7 On the mechanism of oxygen photodesorption 37

2.5.8 Fluorescence quenching through adsorption of gas molecules 39

3 RESULTS AND DISCUSSION 41

3.1 Design, modification and verification of test stands 41

3.1.1 Piping for gas supply 41

3.1.2 Illumination sorce 42

3.1.3 In-situ DRIFTS set-up 43

3.1.4 Photo TPD set-up 45

3.2 Experimental procedure 47

3.3 Synthesis of ZnO materials 48
3.4 Characterization of ZnO Nanostructures 49
3.5 Surface plane determination via Hydroxyl group analysis by means of DRIFTS 54
3.6 Influence of light and heat on DRIFT spectra 57
3.7 CO_2 adsorption on ZnO materials 66
3.8 Influence of UV-illumination on CO_2 adsorption on TiO_2-based materials 73
3.9 Influence of Illumination on desorption of adsorbates on $Ce_xZr_{1-x}O_2$ 84

4 SUMMARY 91

5 OUTLOOK 93

6 LIST OF REFERENCES 95

7 APPENDIX 100

7.1 Characterization methods 100
7.1.1 Powder X-ray diffraction 100
7.1.2 Surface area determination according to Brunauer-Emmett-Teller (BET) theory 102
7.1.3 UV/Vis Spectroscopy 103
7.1.3.1 Diffuse reflectance UV/Vis spectroscopy 104
7.1.4 Infrared Spectroscopy 105
7.1.4.1 Diffuse reflectance infrared Fourier-transform spectroscopy (DRIFTS) 107
7.1.5 Scanning electron microscopy 108
7.1.6 Temperature programmed desorption 108
7.1.7 Mass spectrometry 109
7.2 Supporting DRIFT spectra 110

VI. List of Figures

Figure 1: Schematic depiction of the construction of reciprocal lattice (dashed orange lines) and the Brillouin zone (solid orange square) inside the real lattice (black dots). 8

Figure 2: Schematic depiction of the band model for insulator, semiconductor, and conductor. 10

Figure 3: Schematic depiction of phonon dispersion inside the Brillouin Zone. 12

Figure 4: Simplified representation of possible types of electronic excitons in solid induced by absorption of electromagnetic irradiation. (modified from Ref. [32]) 16

Figure 5: Photo induced processes on the surface and in the near surface area of wide band gap semiconductor photocatalysts. (modified from Ref. 32) 17

Figure 6: Number of scientific publications dealing with photoreduction of CO_2 between 1980 and 2021 according to Web of Science™. (Search conducted on 14.04.2022 as following: "carbon dioxide"(topic) and "photocataly*"(topic) or "CO2" (topic) and "photocataly*"(topic)) 18

Figure 7: Schematic depiction of carbonate species formed on the surface of a metal oxide material as result of CO_2 adsorption. 19

Figure 8: Four main normal vibration modes within a carbonate moiety 20

Figure 9: Schematic visualization of feature assignment to vibrational modes in different carbonate species formed on metal oxide materials due to adsorption of CO_2 according to the summary of literature sources up to 1992 by Turek and Wachs.[56] 22

Figure 10: Schematic visualization of feature assignment to vibrational modes in different carbonate species formed on TiO_2 samples due to adsorption of CO_2 according to literature sources of the last 30 years as summarized in Table 1. 23

Figure 11: A comparison of spectral features assignment to vibrational modes in carbonate moieties with suggestions based on experimental works and new findings based on theoretical calculations. Width of bars does not give exact but roughly estimated ranges. 24

Figure 12: Conduction band, valence band potentials, and band gap energies of various semiconductor photocatalysts relative to the redox potentials at pH 7 of compounds involved in CO2 reduction. Adapted from Ref [13]. 26

Figure 13: Overview of events occurring during UV irradiation of ZnO, the resulting effects and the respective scientists who observed these effects as discussed in this chapter. 31

Figure 14: Schematic depiction of reasons for increased IR absorption in ZnO: (a) ground state, (b) UV irradiation or thermal treatment in reductive atmosphere, (c) desorption of adsorbed species (e.g. oxygen), (d) adsorption of electronegative gas phase molecules. 33

Figure 15: Thermal desorption (TD) spectra of O_2 on non-illuminated (1, green) and illuminated (2, blue; 3, orange) samples. Isotopic content of thermodesorbed O_2 after adsorption in the dark (1), adsorption in the dark with subsequent holding in O_2 (2), adsorption of O_2 in the dark with subsequent holding in ^{18}O-rich O_2 (3) Figure reproduced and modified from literature[116] 35

Figure 16: Temperature-programmed desorption (TPD) spectra of molecular O_2, adsorbed at 300 K on non-irradiated sample (1), on irradiated sample (2), and after illumination of the sample with adsorbed oxygen (3). Figure reproduced from literature.[100] 36

Figure 17: schematic depiction of the installed gas lines leading to the main controlling unit of three MFCs. 41

Figure 18: (i) LUMATEC Superlite S04 lamp utilized for the illumination of the sample during CO_2 adsorption and other experiments; (ii), (iii) spectral properties of the light source at the selected device settings. 42

Figure 19: Schematic depiction of the FT-IR set-up including MFC controlling the gas flow, water saturators, FT-IR device and QMS 43

Figure 20: (i) Harrick in-situ high temperature cell, (ii) top view and (iii) bottom view on hemispherical stainless-steel dome with three windows. 44

Figure 21: Praying Mantis Mirror geometry utilized for measurements of DRIFT spectra: (left) photograph, front view; (right) schematic depiction, back view (modified from Ref. [127]) Blue: incident IR beam, orange: cumulated diffuse reflected IR beam after having contact with the sample and carrying information to the detector. 45

Figure 22: (i) Copper heating block inside the stainless-steel box; (ii) quartz sample holder 46

Figure 23: Air cooling of the Photo TPD set-up by two 120 mm PC fans mounted to a 3D-Printed double funnel(orange) channeling air into a flexible 50 mm steel pipe. 47

Figure 24: Schematic depiction of the experimental procedure. 48

Figure 25: XRD patterns of ZnO samples synthesized during the course of this work as well as reference pattern NIST. 49

Figure 26: SEM images of all ZnO samples investigated in the work at hand: (i) particles (top left), (ii) rods (top right), (iii) flowers (middle left), (iv) flakes (middle right), (v) SSS (bottom). Images (i) to (iv) were recorded at a magnification of 25 000 and 3 kV; image (v) at a magnification of 1 000 and 5 kV. 51

Figure 27: Graphical determination of the band gap values from measured DR-UV/Vis-spectra of all ZnO materials. 52

Figure 28: DRIFT Spectra of all as synthesized ZnO nanomaterials as well as commercial ZnO particles. 53

Figure 29: DRIFT spectra of as synthesized samples recorded during thermal treatment in Ar flow: (i) particles (top left), (ii) rods (top middle), (iii) flakes (top right), (iv) flowers (bottom left), (v) SSS (bottom right). The range was cut down for better determination of hydroxide groups for characterization of exposed surfaces present on the material. 55

Figure 30: comparison of behavior of hydroxyl groups during thermal pretreatment of commercial particles in (i) Ar or (ii) 15% O_2 atmosphere. 56

Figure 31: Comparison of behavior of hydroxyl groups during thermal pretreatment of as synthesized rods in (i) Ar or (ii) 15% O_2atmosphere. 57

Figure 32: Comparison of 3D spectra of ZnO particles recorded during thermal pretreatment with heating rates of (i) 1 $Kmin^{-1}$, (ii) 2 $Kmin^{-1}$, (iii) 5 $Kmin^{-1}$ and (iv) 10 $Kmin^{-1}$ in 30 ml/min Ar flow. Target temperature of 450 °C was reached at (i) 425 min , (ii) 210 min, (iii) 85 min, (iv) 45 min followed by holding the sample for 1h at 450 °C and cooling down to room temperature 58

Figure 33: Schematic depiction of electrical current versus time in an ZnO sample in regard to darkness and illumination(i)[95]; Band intensity at 1800 cm-1 in DRIFTS measurements of (ii) unpretreated ZnO particles(np) and rods(nr) in Ar or synthetic air atmosphere in dependence of illumination with light of 380-520 nm wavelength; (iii) thermal treatment of ZnO particles and rods in argon or oxygen containing atmosphere to 450°C; (iv) thermal treatment of ZnO particles in argon or oxygen containing atmosphere to 600°C. 60

Figure 34: 3D depiction of series spectra recorded during thermal treatment of ZnO samples: (i) particles, (ii) rods, (iii) flowers, (iv) flakes, (v) SSS. A uniform heating procedure in 30 ml/min Ar flow was applied during all measurements: 0-50 min: heating from RT to 450°C with 10K/min; 50-110 min: holding at 450°C for 1 hour; 110 min – end: cooling down to room temperature. 62

Figure 35: Schematic depiction of abstract consideration of charge carrier distribution and overall conductivity in ZnO materials with different morphologies 63

Figure 36: Schematic depiction of events leading to increased IR absorption of ZnO after thermal treatment in reductive atmosphere or illumination with UV light. 65

Figure 37: Normalized TCD signal recorded during the temperature programmed CO_2 desorption experiment after adsorbing CO_2 at 50°C(black) and 175°C(blue) on ZnO particles sample. Red curve belongs to the secondary y-axis and gives the temperature detected in the reaction chamber. 66

Figure 38: (left)desorbed CO2 amount after adsorption of CO_2 at 20% CO2 in Ar and 175°C or 50°C on ZnO particles sample thermally pretreated in (left) pure Ar or (right) 20% O_2 in Ar; (right) results of CO_2 adsorption presented by Lyashenko and Gorokhovatskii[142]. A comparison between (1) photocatalytic not active sample, due to thermal pretreatment in vacuum at 200 °C for 3h and (2) photocatalytic active sample, pretreated at 520 °C in 88 mm Hg (0.117 bar) for 10 h; additional comparison between adsorption (blank) with additional illumination and (filled,´) without.....67

Figure 39: DRIFT difference spectra recorded during CO_2 adsorption and subsequent purging with Ar on ZnO particles sample after thermal pretreatment in Ar. 68

Figure 40: Mass traces for effluent CO_2 recorded during the thermal treatment after adsorption of CO_2 under illumination(yellow) and in the dark (black). All concentrations were normalized by the surface area of the respective material. 70

Figure 41: Summarized results of CO_2 desorption experiments after thermal treatment at 450 °C in Argon and CO_2 adsorption at room temperature. The DRIFTS set-up was unitized for all measurements. 71

Figure 42: Summarized results of CO_2 desorption experiments after thermal treatment at 450 °C in Argon and CO_2 adsorption at room temperature in the dark or under illumination. The photo-TPD set-up was unitized for all measurements.....72

Figure 43: Schematic visualization of feature assignment to vibrational modes in different carbonate species formed on TiO_2 samples due to adsorption of CO_2 according to literature sources of last 30 years summarized in Table 1. An exemplary DRIFT spectrum of adsorbed CO_2 on TiO_2 was added additionally. 74

Figure 44: Difference DRIFT spectra recorded during the CO_2 adsorption experiment in dark(i) and under illumination(ii) as well as the subsequent thermal treatment((iii), (iv)) of the anatase sample. The last spectra of the top depictions (red) are the first spectra of the bottom depictions (dark teal).....76

Figure 45: Difference DRIFT spectra recorded during the CO_2 adsorption experiment in dark(i) and under illumination(ii) as well as the subsequent thermal treatment((iii), (iv)) of the P25 sample. The last spectra of the top depictions (red) are the first spectra of the bottom depictions (dark teal).....79

Figure 46: Difference DRIFT spectra recorded during the CO_2 adsorption experiment in dark(i) and under illumination(ii) as well as the subsequent thermal treatment((iii), (iv)) of the m-TiO_2 sample. The last spectra of the top depictions (red) are the first spectra of the bottom depictions (dark teal).....81

Figure 47: (i) Graphical determination of the band gap value from measured DR-UV/Vis-spectra and (ii) a photograph of the $Ce_xZr_{1-x}O_2$ sample.....85

Figure 48: Weight normalized mass traces for CO_2 in the effluent stream recorded with the QMS during thermal treatment tests of $Ce_xZr_{1-x}O_2$ sample in the Harrick cell in Ar. (black) Thermal treatment in dark; (orange) illuminated thermal treatment with additional illumination (400-700 nm, 225 $mWcm^{-2}$). 86

Figure 49: Mass traces for CO_2 and H_2O in the effluent stream recorded with the QMS during initial irradiation tests of untreated $Ce_xZr_{1-x}O_2$ sample in the Harrick cell. 87

Figure 50: Schematic depiction of the four-step experiment for a direct comparison between illumination and thermally assisted desorption.....88

Figure 51: Mass traces of CO_2, H_2O and O_2 recorded by the QMS from the effluent gas stream of Ar during the thermal pre-treatment of the sample. 88

Figure 52: (i) Weight normalized mass traces of CO_2 recorded by the QMS from the effluent gas stream during the illumination with light (orange) of the spectral range 400-700 nm (225 $mWcm^{-1}$) and thermal treatment in Ar at 45 °C (black); (ii) Weight normalized mass traces of CO_2 recorded during final thermal post treatment after illumination of the pretreated sample with light (orange) or holding the sample at 45 °C for 2 h (black).....89

VII. List of Tables

Table 1: Summary of feature assignment to vibrational modes in different carbonate species formed on TiO_2 samples due to adsorption of CO_2 according to literature sources of last 30 years. 25

Table 2: Relevant steps in photocatalytic CO_2 conversion and respective chemical potentials versus NHE. 27

Table 3: Summary of synthesized nanostructured samples. 52

Table 4: Band positions of adsorbed hydroxyl groups on ZnO surface 54

Table 5: Summary vibrational modes and identified species formed during adsorption of CO_2 on ZnO particles in the dark. Corresponding wavenumbers are given in [cm^{-1}]....68

Table 6: Summary vibrational modes and identified species formed during adsorption of CO_2 on anatase. Corresponding wavenumbers are given in [cm^{-1}]....75

Table 7: Summary vibrational modes and identified species formed during adsorption of CO_2 on P25. Corresponding wavenumbers are given in [cm^{-1}]....78

Table 8: Summary vibrational modes and identified species formed during adsorption of CO_2 on m-TiO_2 material. Corresponding wavenumbers are given in [cm^{-1}]. 81

Table 9: summary of identification of formed adsorption species on different TiO_2 materials upon exposure of CO_2 in dark and under illumination 84

VIII. Symbols and Acronyms

Symbol	Quantity	Unit
a	distance between atoms in a (reciprocal) lattice	m
$\beta_{1/2}$	half-maximum breadth of diffraction life	
β_{hkl}	breadth of diffraction line (hkl)	
δ_i	deformation vibration of group i	
λ	wavelength	nm
μ	reduced mass	kg
ν	frequency	s^{-1}
$\tilde{\nu}$	wavenumber	cm^{-1}
ν_i	stretching vibration of group i	
ω	phonon frequency	s^{-1}
ϱ_i	density of state i	
θ	*Bragg* diffraction angle	°
d(hkl)	lattice plane spacing	
e/e^-	electron	
e^0	exciton	
e^0_{tr}	bound exciton	
E_C	energy of the bottom conduction band edge	
E_g	band gap energy	eV
E_n	vibration energy levels	
E_F	*Fermi* energy	
E_J	rotation energy levels	
E^0_{redox}	chemical potential versus normal hydrogen electrode	
E_V	energy of the top valence band edge	
h	(electron)hole	
$\hbar$	*Planck* constant	Js
hkl	*Millar* indices	
I	moment of inertia	
J	rotational quantum number	
k	force constant of vibrating bond	Nm^{-1}
k	momentum of a particle	$kgms^{-1}$
k	wave vector	

k_B	*Boltzmann* constant	$m^2kgs^{-2}K^{-1}$
m	mass	g
n	molar amount	mol
n	vibrational quantum number	
N_A	*Avogadro* number	
p	pressure	Pa
r	bond length	nm
r_{eq}	equilibrium bold legth	
R	gas constant	$JK^{-1}mol^{-1}$
R_J	rotational energy levels	
S_{BET}	specific surface area by means of BET method	m^2g^{-1}
T	temperature	°C / K

Akronyms	
BET	*Brunauer-Emmet-Teller*
DRIFTS	Diffuse reflectance infrared *Fourier* transform spectroscopy
DRS	UV/Vis diffuse reflectance spectroscopy
FT	*Fourier* transform
IR	infrared
MFC	mass flow controller
np	nanoparticles
nr	nanorods
P25	mixed-phase TiO_2 (~80% anatase and ~20% rutile)
QMS	quadrupole mass spectrometer
RT	room temperature
SEM	scanning electron multiplier
TPD	temperature programmed desorption
UV	ultraviolet
Vis	visible
XRD	X-ray diffraction

1 Introduction

In 1976 98% of total energy supply relied on combustion of fossil fuels like oil, coal, and gas thus being the main contributor to the rising CO_2 level in the atmosphere.[1] By that time the atmospheric CO_2 reached 310 to 330 ppm, which already meant an increase by 15% compared to the pre-industrial revolution age around 1850. During the "Workshop on the global effects of carbon dioxide from fossil fuels" in 1979 Bacastow and Keeling presented calculations estimating a further increase of CO_2 to 430 ppm by the year 2020,[2] which came shockingly close to today's amount of CO2 in the atmosphere of 414 ppm. Due to extensive use of fossil fuels this meant an increase by over 30% over the last 70 years.[1,3] CO_2 being one of the main greenhouse gases contributes to the global temperature increase. Even if the rise in CO_2 level will be limited, the fossil fuel based infrastructures present nowadays would still end in a global warming by 1.5 to 2 K by the end of the century.[4] It is therefore of crucial importance to reduce the atmospheric amount of CO_2 in addition to a decrease in emissions. Search for alternative ways to cover energy needs emerged in the time of oil crisis in the beginning of 1970s. Since coal was assumed to last much longer than oil, liquefaction of coal was suggested as a possible solution. However, due to a lower hydrogen and much higher aromatic polycyclic hydrocarbons content, but especially due to 10 to 20 times more carcinogen compounds like benzo(a)pyrene, utilization of this technique was limited. Another route implemented the search for plants storing CO_2 and thus forming energy-dens hydrocarbons. In 1912 already Giacomo Ciamician criticized human civilization' focus on using exhaustible *fossil solar energy* i.e., coal, while it is much handier to use everlasting radiant energy of the sun directly.[5] In his work he presented the idea of converting biomass into gaseous fuels with the goal of efficient and economic fuel production from renewable biomass resources. In 1938 G. A. Frick mentioned utilization of gasoline-like liquids from cactoids *Euphorbias* as a possible solution to Italy's problems of oil shortage and alternative source for fuel for the automotive sector.[6] In the 1970 sugar cane plantations were suggested for ethanol production as a source of fuel and stock chemicals for the petrochemical industry. Refining the process and domesticating

the wild plants was supposed to lead to a total of 20 barrels of oil out of 1 acre. However, these techniques would compete for agricultural space also required for food production.

In 1978 J. R. Bolton published a detailed calculation on thermodynamic limitations for conversion of light to work within natural photosynthesis systems.[7] For a spectrum ranging from 300 to 840 nm an efficiency of about 28-32 % was suggested. Adding additional losses like storage losses and further kinetic limitations yielded in a maximum efficiency under kinetic control of 21 %, while net yield of products in a photochemical energy storage reaction is unlikely to be greater than 12-13 %. Assuming optimal conditions like all photons of this spectral region are absorbed, and 8 photons per O2 molecule evolved – 13.3 % is reached. While utilizing a threshold of 360 to 700 nm (upper limit of 720 nm is possible due to thermal activation) photosynthesis observed in nature comes quite close to the "perfect" systems. Calculated efficiency of solar energy storage in nature are at about 9.2 ± 0.8 % which was in good comparison with other works.[8,9] However, adding the real values for dark respiration and photorespiration results in a net efficiency of about 5.6 ± 1.2 %. As further limitations may decrease the efficiency even further nature was "forced" to use two consecutive photosystems. As a consequence, an ultimate artificial photosynthesis reaction would employ two coupled reactions so that two protons are used for every electron transfer - especially by utilization of abundant photons in the visible region.[10]

Despite in 1978 J. K. Thomas urged the scientific community to improve conventional and to seek alternate sources of energy, suggesting storage of solar energy and conversion to heat, chemical compounds of high energy, or electric power, it took nearly 20 years until in the beginning of 2000's the chemical storage of solar energy started to gain the awareness it deserves. The still ongoing rise in global energy demand, restrictions to carbon emissions and the use of fossil fuels once again emerge in the need in renewable and environmentally friendly energy sources. A possible solution for both problems is to directly utilize CO_2 as an agent for storage of excess energy resulted from temporal overproduction by renewable energy sources such as wind turbines. An even more direct approach is to utilize CO_2 as a feedstock for photocatalytic conversion of the solar energy to valuable products such as platform chemicals or fuels. In this way three problems can be addressed at once. Numerous CO_2 valorization approaches are discussed in the scope of different Power-To-X technologies and projects dealing with the main goal of chemical storage of excess energy from renewable sources. While some discuss the production of CO_2 based stock chemicals, other see in so called "e-fuels" the future of circular carbon economy without a need in abundant fossil carbon sources.

In 1972 Fujishima and Honda reported successful dissociation of water into hydrogen and oxygen due to an applied bias on a combination of Pt and n-type TiO_2 which was capable of producing a

photovoltage under illumination with UV light. The idea behind it was the eventual capability of improved semiconducting materials to catalyze water dissociation under influence of solar irradiation only.[11] Over the last years metal oxide-based materials were found to show good photocatalytic activity not only in water splitting, but also in conversion of CO_2.[12-15] TiO_2 and ZnO are two of the most famous semiconductor materials and offer a wide research base. Still, the photocatalytic conversion efficiency of CO_2 is very low, since not all conversion and reaction mechanisms are well understood today. Events like quenching result in unwanted processes like cycloadditions, free radical or radical ion reactions, polar substitutions, or additions.[13,16] Simple back reactions lead moreover to waste of energy and result in no net chemistry. Even though redox chemistry proceeding from light-induced electron transfer reactions has been subject of research for a long time, the understanding of reaction processes and thus rate of efficiency for artificial photosynthesis systems is quite low. Especially the influence of illumination on the adsorption and desorption of CO_2 on metal oxide-based materials is a point of debate.[17] Hence, the investigation of CO_2 adsorption on metal oxide-based materials was set as the topic. Being quite widely spread possible directions concerning the material of choice as well as its design were outlined quickly. For this purpose, different ZnO, TiO_2 and $Ce_xZr_{1-x}O_2$ material were chosen since all show very good CO_2 adsorption properties, are of low toxicity and offer a wide base of scientific literature due to nearly 100 years of research. However, despite adsorption of CO_2 on semiconductor materials has been investigated for such a long time, especially in the last decades numerous scientific works appeared showing insufficient literature research combined with poor understanding of spectroscopic methods as well as results, leading to accumulation of questionable postulations. Thus, a short critical review was prepared in the course of this work outlining poor literature sources, providing possible corrections and hopefully increasing the awareness of the readers towards importance of good (literature) research work.

Thorough literature research was conducted on further topics. By this a huge scientific field dealing with influence of UV-irradiation on ZnO materials was uncovered. In the early 20th century especially scientists in former Soviet Union conducted numerous scientific works on this topic which – due to Cold War conflicts – were rarely published in English language. As these works were originally available in printed media only and hardly any were transferred into the digital form, they slowly disappeared in shelfs of library archives while the precious knowledge is being forgotten with them. Since most of the past but also modern works deal with certain irradiation iduced phenomena in semiconductor materials from the point of view of solid-state physics, greater effort was put into the study of this specific field in order to better understand and explain observations and events occurring during the experimental work.

2 Theory and State of the Art

2.1 ZnO

Zinc oxide (ZnO) is a II-VI wide band gap semiconductor featuring a bandgap of ~3.44 eV at 0 K and 3.37 eV at room temperature, respectively. In nature one can find ZnO as the rare mineral called zincite. Due to natural doping by other atoms like Fe and Mn zincite usually appears in a color range from red to yellow. Synthetic ZnO, however, is colorless, which is also according to its band gap in the near UV region. Similarly to some IV, III-V, II-VI and VII semiconductor compounds ZnO usually crystallizes in the wurtzite type structure with tetrahedral coordination of the Zn atoms. This is unlike other II-VI group compounds like ZnS featuring both hexagonal (wurtzite) and cubic (sphalerite or zinc blende) space groups in the crystal structure.

Commercial ZnO has been known for a very long time. One of the oldest patents to find is dated to 1879 and deals with the utilization of ZnO as paint additive for the creation of white paint called "zinc-white".[18,19] In the beginning of the 20th century ZnO gained a lot of interest especially among natural scientists, mainly due to its versatile properties and thus wide range of application possibilities, but also because of its large scale availability and easy synthesis. The importance of research on ZnO is best described by the story of Erich Mollwo (1909-1993), who was one of the German pioneers in spectroscopic investigations of ZnO. After the World War II he had to promise to the allied forces to never do research on ZnO again, as it was considered as systematically relevant. Interestingly, when he in 1949 was called to a newly founded research institute in Erlangen, his research focused nearly completely on ZnO.[20] Another example is the Russian scientist Aleksandr Nikolaevich Terenin (1896-1967), whose leading work on ZnO starting as early as 1925 paved the way towards deeper understanding of semiconductor materials among soviet scientists, but also all around the world and who was granted among numerous other awards the title of "Hero of Socialist Labor" in the 1966.[21]

The general peak in research was reached in the time between 1960s and 1980s, where main topics were electronic and optical properties of ZnO. However, the interest dropped due to some difficulties. While n-doping by Al, Ga or In was achieved easily, p-doping turned out to be very

difficult. Ambipolar doping was hardly possible, which is a *prerequisite* for utilization in semiconductor or optoelectronic applications. During that time ZnO was a promising contender for the creation of semiconductor laser-diodes covering spectral ranges in the blue, violet and/or near UV region. Furthermore, the increasing successes in the research in materials featuring structures of reduced dimensionality i.e., superlattices as well as quantum-wells, -wires and -dots, which substituted the need of p-type doped ZnO and thus led to a temporal drop in interest. In the beginning of the 21st century ZnO regained much of its earlier interest and experienced a renaissance in research. Since a lot of former scientific findings have been forgotten over the years, some part of the research was a repetition of previous works. In 2010 C. F. Klingshirn wrote in his textbook "Zinc Oxide":

"[…] not a too small fraction of papers […] are overinterpreted, without taking too much care about consistency or plausibly of their interpretations nor of past results. […] Ambitious young scientists frequently either simply do not know or do not bother about the fact that many things, which they enthusiastically want to present as new, are actually known since decades."[22]

Due to the long presence and returning interest numerous detailed review article on ZnO are available from different points of time throughout the 20th and meanwhile also the 21st century so new scientists entering the research field are advised to undertake a thorough literature research phase in order to properly contribute to the evolution of the material as well as its application and use cases. Nevertheless, the loss in knowledge as well as the presence of the Iron Curtain throughout a large part of the 20th century and its contribution to the research barriers will be addressed in a separate chapter.

Still, new achievements have been made in the recent decades like the successful and reproducible p-type doping and following development of light emitting diodes and lasers or growth of nanostructures. While in the early years of research ZnO was mostly synthesized by simple calcination of organic zinc precursors at temperatures near 1200 K and resulted in large crystals, nowadays the geometrical appearance of nanostructured ZnO has virtually no limits. Over the years researchers managed to synthesize ZnO in numerous different nanostructures with interesting and often unique properties allowing the utilization of the material in a broad field of applications. On this occasion Klingshirn wrote in his textbook (mentioned earlier) a very matching description of the research on ZnO nanostructure synthesis:

"Additionally ZnO has a strong tendency for self-organized growth of nanostructures, above all of nano-rods but also of many other types of nano-structures like tetrapods (or fourlings), nano-belts, -ribbons, -nails, -combs, -flowers, -walls, -castles, -tubes, -wool, -corals, or -cabbage, etc., depending on the imagination of the respective author and from which especially the last mentioned ones are frequently nothing but an unsuccessful (and often hardly reproducible) attempt to grow high quality epitaxial layers."

Due to its diverse properties ZnO can be found in a broad range of applications for example in industrial productions of rubber, textile, pharmaceuticals, cosmetics, electronics but also other applications. Out of the annual production of ~10^5 tons of ZnO the largest part is utilized by the rubber industry for the production of different kinds of cross-linked rubbers.[23] Przybyszwska *et al.* have shown for example that the morphology of ZnO particles has a strong effect on the crosslinking process of rubber.[24] Addition of ZnO particles to the manufacturing process results in the production of vulcanizates featuring increased density of crosslinking and thus superior mechanical properties. However, as ZnO is toxic to aquatic systems in higher dosage[25], some research is focused on decreasing the environmental impact of rubber industry by modifying and/or reducing the amount of used ZnO[26] as well as finding appropriate alternatives in manufacturing processes.[27]

In ZnO one can find four low index diamond structures according to Miller notation: two non-polar surfaces $(10\bar{1}0)$ and $(11\bar{2}0)$ as well as two polar surfaces; (0001) being the zinc-terminated and $(000\bar{1})$ the oxygen terminated one. Despite the latter two being polar, these are stable. Theoretical calculation of Mora-Monz suggested the presence of microscopic states of similar energy, but also reconstruction into ordered geometries on both faces as possible reasons for their stability.[28] While on zinc terminated surface zinc ions are suggested to move between first and second layer freely and thus contributing to a vivid reconstruction of the facet, oxygen terminated surface is found to be more steady. Movement of O ions between layers is found, when the top Zn layer is fully occupied only, and every vacancy is filled by an O ion. Reconstruction into triangular patterns on Zn terminated surface and into hexagonal on oxygen faces was calculated theoretically while also being in good agreement with experimental works of other scientists. As a possible reason for the formation of organized patterns the authors name particular values of chemical potential and associated surface energy distribution.[28]

Numerous applications of ZnO as photocatalyst can be found published every day. Lee *et al.* have summarized some of the achievements in utilization of modified ZnO photocatalysts in waste water treatment as well as pollutant and contaminants degradation.[29] However, some number of the reported use cases are presumably rather substitutions, the according research group came up

with in order to be able to publish their work at all, resulting from unsuccessful attempts challenging a huge problem in modern environmental chemistry. One of the most pursued aims in ZnO utilization is the photocatalytic CO_2 reduction. As mentioned earlier CO_2 being a large contributor to the climate change offers at the same time a virtually endless feedstock of carbon. Simultaneous utilization and chemical storage of solar energy for direct conversion of CO_2 to valuable stock chemicals promises to open the route to slowing down, stopping, and maybe even reversing human-made climate change (and thus bringing eternal glory to the first one to successfully achieve this goal in an economically viable process).

2.2 A Brief dive into solid-state physics

Following chapters shall be an introduction into physical principles of solid-state materials. It is a summary of different parts of textbooks dealing in detail with topics of general quantum mechanics and solid-state physics, thus the reader is being advised to refer to sources [22,30,31] for a deeper insight.

2.2.1 Reciprocal lattice and k-space

In solid materials the real space lattice is not always the appropriate starting point for discussion of all electronic properties, since it provides information about the position, but not the energy of electrons or other particles. For an alternative description, using Fourier transformation, the real space is converted to an energy space being referred to as reciprocal space (in solid-state physics more common: momentum- or k-space). It provides a useful platform to describe electronic energy states in solids, but also momentum transfer in collision and scattering processes. The reciprocal space features a reciprocal lattice (which is also used for description of diffraction phenomenon in

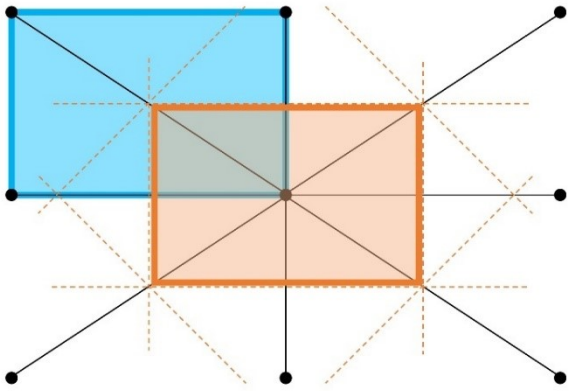

Figure 1: Schematic depiction of the construction of reciprocal lattice (dashed orange lines) and the Brillouin zone (solid orange square) inside the real lattice (black dots).

a crystal) build up by reciprocal lattice vectors between lattice points (atoms). One can draw perpendicular planes halfway between each lattice point dividing the reciprocal space into zones of equal volume i.e., first Brillouin zone which is a Wigner-Seitz cell of reciprocal space (s. Figure 1). It has the same volume as the basic unit cell in the lattice but encloses only one lattice point. Due to a periodicity of the crystal lattice the first Brillouin zone is periodic as well. Since in each of these periodically repeating cells the same physical events take place, the Brillouin zone is therefore sufficient for the characterization of electronic material properties like phonons, dealing with interactions between phonons or phonons and electromagnetic radiation, as well as distinction between energetic states of energy bands (band structure). At the boundary of the Brillouin zone electrons feature a "jump" in their energy dispersion known as energy- or band gap. For a simple cubic lattice with a lattice constant "a", the Brillouin zone has a cubic shape in the reciprocal space as well, but with a, edge length of π/a.

In reciprocal space each momentum **k** is related to an energy by the electronic energy dispersion E(**k**). The Fermi surface is a contour of constant energy in the reciprocal space, where E(**k**) has the value of the Fermi energy (E_F) – which is the energy of the weakest bound nucleon. Considering the Fermi-Dirac distribution which describes a gas of free fermions, at T = 0 K the highest occupied energy state in a system is called Fermi edge. A certain number of electrons cannot occupy an infinitesimal small volume in the k-space. Consequently, the k-space is being divided into cells of a fixed size occupied by only two electrons with the same energy (but different spin) which is in accordance with the Pauli exclusion principle. A free electron in k-space at 0 K represents the minimal volume and is often depicted as a ball shaped space i.e., the Fermi surface. With other words, at zero temperature an electron occupies all the states up to the fermi level which, when observed as the fermi wave vector in 3D, leads in a fermi sphere in reciprocal space. In a periodic potential of a crystal lattice the energy is anisotropic which leads to a deformation of the ball shape. The Fermi surface is the outer surface of this space and separates electrons in ground state from unoccupied levels in the k-space at 0 K. Following the Fermi-Dirac statistics at temperatures higher than 0 K, states above E_F can be occupied by electrons with $k > k_F$ due to thermal excitation. A resulting empty space represents a missing electron. Therefore, an empty space at k_F is being enclosed in the k-space featuring an empty electron pot i.e., a hole.

2.2.2 Electronic band structure of semiconductors

In a solid material with a periodic crystal structure the entirety of similar energetic states is summarized into density of states which according to the band theory are better known as "bands". Many of those materials feature a so-called valence and a conduction band, which represent the

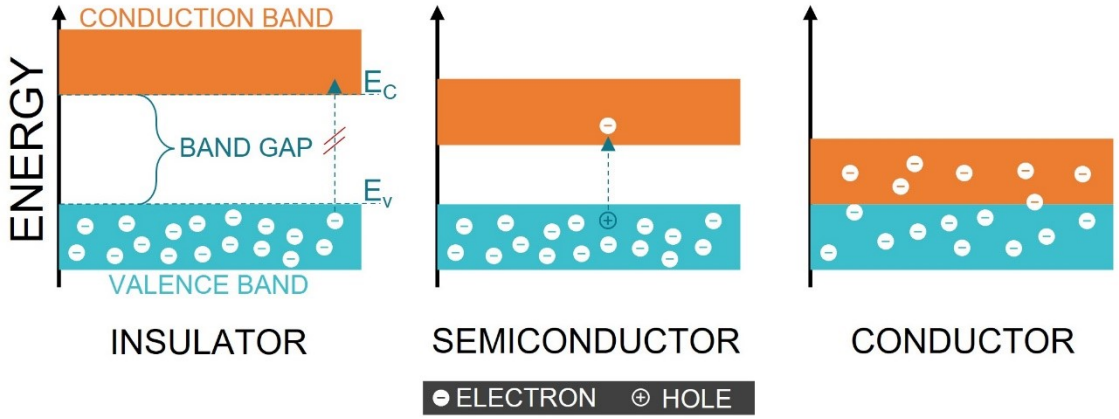

Figure 2: Schematic depiction of the band model for insulator, semiconductor, and conductor.

entirety of all highest occupied atomic orbitals (or density of states) and lowest unoccupied atomic orbitals, respectively. The Conduction band usually accommodates mobile charge carries i.e., electrons which then contribute to the current conducted through a solid material. The bottom edge of the valence band features the zero-energy level, while the upper edge is referred to as E_v. The lower conduction band edge is denoted as E_c and often $E_c > E_v$. The energy gap between these two determines among other properties the conductivity of the material. In conductors like metals valence- and conduction band overlap, while semiconductors and insulators exhibit an energy gap between these two bands which is also called "band gap", which is schematically depicted in Figure 2. Depending on the size of the band gap externally introduced energy can be utilized to bridge the energy gap while being absorbed by electrons and thus lead to an excitation from the valence band to the conduction band. Usually, semiconductors feature a band gap of some eV – in general however much larger than the scale factor k_BT (k_B: Boltzmann constant; T: temperature). Consequently, electrons that are to be thermally excited must overcome the band gap energy. More often, the excitation is achieved by electromagnetic radiation, however, only above certain frequency of $\nu_{min} = E_g/\hbar$ (E_g: Band gap energy; $\hbar$: Planck constant). Like metals, semiconductors feature a broad range of absorption. When an electron is excited from its ground state, the excited state can be described by a coexistence of an electron above the Fermi edge (outside the Fermi surface) and a hole (or deflectron) below it, as shown in Figure 2. The original repulsive Coulomb interaction turns in the electron-hole framework into an attractive interaction between a negatively charged excited electron in the conduction band and a positively charged hole in the valence band. Here electrons and holes both can be considered as free particles with opposite charges and masses m_e and m_h. The masses are often also referred to as m_c and m_v due to the dependence of the particles to the respective conduction or valence band. However, due to (shielded) Coulomb

attraction they often appear as a single particle. In general, pairs of electrons and holes are bound to each other and are often referred to as quasi-particles called excitons. Exciton states are well described by a hydrogen single particle model and thus electron-hole pairs may move as free particles. However, in the lowest excited states neither there are quasi-free electrons in the conduction band nor quasi-free holes in the valence band, but – due to strong Coulomb interactions – there are energetically low immobilized exciton levels. In an excited system the number of excited electrons in the conduction band equals the number of holes (i.e., unoccupied electron states) in the valence band. Formation of excitons may cause a shift, a splitting or a change in intensity of spectral lines of a material. Excitons may be stationary or mobile – latter influence the energetic levels of a system and are followed by an interaction between particles of a crystal. The interaction is caused by the interaction between the transition dipole moments of an excitation. Depending on how strong the interaction is, the speed of the migration of an exciton can be between fast and stationary. In a molecule an electric dipole transition – caused by a transition dipole casting a certain force on neighboring molecules – leads to a charge shift. Parallel orientation of dipoles is energetically rather unfavorable, which means an absorption occurs at higher frequencies than in an isolated molecule. When the dipoles are joined head to tail, they are energetically more favorable, hence the transition occurs at lower frequencies than in an isolated molecule.

The chemical potential of a system corresponds to the energy required to add a particle to the system and is often located within the band gap, but not necessarily in the middle of it. Its position depends on the effective mass ratio of electrons and holes present in the system, and thus also on the density of states (i.e. $\varrho_{C,V}(E)$) of the conduction and valence bands as well as on the temperature. At T = 0 K the chemical potential equals the Fermi energy of a material which also leads to the population of the valence band only, while the conduction band states are unoccupied. At temperatures above 0 K thermal excitation leads to an increase on the chemical potential over E_F. In an intrinsic semiconductor with a band gap of 1 eV and 10^{23} electrons at room temperature, approximately 10^7 electrons would be positioned in the conduction band resulting in a higher chemical potential than at T = 0 K.

2.2.3 Plasmons

Excitation of electrons and thus creation of excitons can occur not only for a single electron-hole pair. A certain momentum q can lead to collective electron-hole excitations. While single excitons may exist also in a system completely free of interactions (or in a system of uncharged fermions), a collective excitation of the entirety of electrons of a system may also occur. Deflection of the

electron gas can occur to a certain distance from the positively charged background system, which leads to a polarization and thus creation of an electrical field of a volume unit. As there is still a repulsive force acting on the electron gas, this leads to a movement similar to a harmonic oscillator i.e., harmonic oscillation of the electron gas as a whole around the equilibrium state. The characteristic frequency for a collective oscillation is called plasma frequency also known as Langmuir waves. consequently, a collective excitation of an electron system as a whole leads to a quantized plasma oscillation excitation and is better known as a "plasmon".

2.2.4 Phonons

While photons are quanta of an electromagnetic field, phonons are elementary quanta of lattice vibrations in a solid material with a crystal lattice structure. The distribution of photons in a thermodynamic equilibrium (undistinguishable particles of an ideal gas) can be described by Planck's law. Here phonons and photon gas (blackbody radiation) show some analogies in the thermodynamic properties, as both are bosons and follow the same Bose-Einstein statistics. Vibrations of the lattice, on the other hand, assuming harmonic and adiabatic approximation and after choosing proper phonon coordinates, are described as an ensemble of non-coupled oscillators. The energy momentum relation of normal-mode lattice waves, which is better known as the phonon dispersion relation (s. Figure 3), represents one of the fundamental physical properties of materials with crystalline structure. The dispersion relation for phonons relates the phonon frequency to the wave vector k, where each k features a discrete energy of lattice vibrations depending on the dispersion branch. There are two different dispersion branches describing optical- and acoustic phonons. In a unit cell, atoms can vibrate out of phase or in phase. At wave vector k = 0 non vanishing frequencies exist which means they can be excited in the visible region of electromagnetic irradiation i.e., optically. Thus, optical phonons are elementary excitations of

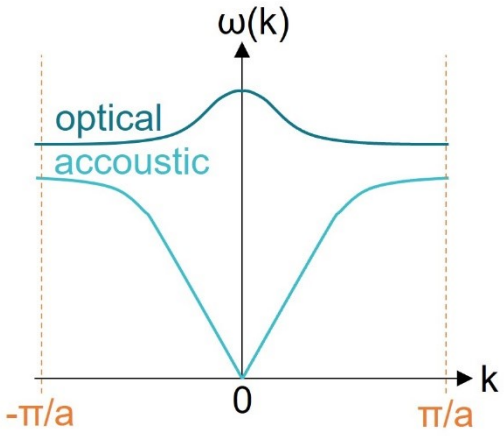

Figure 3: Schematic depiction of phonon dispersion inside the Brillouin Zone.

optical lattice vibrations. On the other hand, acoustic phonons correspond to lattice vibrations following the acoustic branch of the dispersion relation. In a unit cell, atoms can be deflected in phase from their ground state or equilibrium position which means a collective deflection of the ionic charge density takes place. Electrons staying in their own equilibrium state results in a collective plasma vibration of the ionic system around its equilibrium state. However, this contradicts to the dispersion relation of acoustic phonons in the long-wavelength limit, where the eigenfrequency must disappear. Consequently, electrons adjust their state according to the motion of ions resulting in an instant shielding of possibly appearing polarization. As a result, acoustic phonons are uniformly deflected and oscillate. That means, acoustic phonons equal lattice vibrations which are excited by sound waves, and which also transport sound through the crystal. In a phonon gas a heat source with periodically changing temperature induces a wavelike fluctuation in temperature and thus in entropy which may transport energy due to fluctuation of local energy densities. This effect is often referred to as second sound. Contrary propagation of sound in a classical gas shows energy transport due to wave like fluctuation in the local density of mass. Additional one distinguishes between longitudinal and transversal phonons for each branch depending on the wave vector k. However, an unambiguous distinction is not always possible.

Lattice vibrations can cause energetic transitions such as scattering processes on phonons which feature quasi-momentum and energy conservation. In harmonic approximation phonons behave like quasiparticles, featuring attributes like an infinite lifetime, a quasi-momentum, no particle number conservation, and no chemical potential. As there is no effective movement of center of gravity during a general excitation of atoms, phonons do not have a real momentum. If one adds the anharmonic contributions in the potential of the lattice restoring force (which is treated in the context of perturbation theory), phonons have a finite lifetime. Thus, anharmonic interactions with lattice defects, crystal edges and electrons are possible. These interactions are also responsible for the exchange of energy in a photon gas and determine the thermal and electronic transport properties in a solid. In general, anharmonic effects are thermal expansion, temperature, and pressure dependence of elastic constants, but also a deviation from the Dulong-Petit law at high temperatures. Considering the conservation of quasi-momentum, anharmonic phonon-phonon interactions may be seen as the cause for momentum transport (at low temperatures as well) and in metals sometimes a contribution to the conductivity.

In a Born-Oppenheimer approximation one can discuss following either the time scale or mass ratios. Compared to electrons, the movement of ions/atomic cores is very slow, which means that electrons have time to adjust to changes. Looking at the system from the electron perspective, the core- or ion-system appears to be a time independent stationary system. Still, a coupling of electrons

and lattice dynamics cannot be neglected. In standard perturbation theory lattice vibrations feature typical energies which are smaller than typical electron energies by the factor of $\sqrt{m/M}$.

2.2.5 Interaction of phonons with other particles

Depending on the model assumptions, electrons and phonons can be considered as coupled or decoupled. Here we consider the case where electrons are influenced by the attractive coulomb potential of lattice ions or atom nuclei. Consequently, one can treat the electron-phonon interactions like the electrostatic Coulomb potential, however shielded by other electrons (for example in lower shells). Over the years different kinds of interactions between phonons and electrons have been discovered and investigated. One of those is an elementary electron-phonon vertex with a phonon absorption or emission. Here due to a collision of an electron with a lattice ion a phonon is either created or absorbed following the rule of momentum conservation (limited to small momenta in the first Brillouin zone). Depending on the transferred momentum (electron and phonon) a reciprocal lattice vector needs to be added to bring the momentum back into the first Brillouin zone – which means either Umklapp (flip-over) scattering or normal scattering is present. Transverse phonons which are perpendicular to the phonon vector give no contribution to the effective electron scattering, so there is only coupling of electrons with longitudinal phonons. In a model consisting of several energy bands/levels an inter-level scattering of electrons mediated by phonon absorption or emission is possible, which allows for coupling of both optical and acoustical phonons to electrons. In particular, deflection of differently charged atoms from their ground state and vibration against each other (which is the origin of optical phonons) creates long distance dipole fields to which electrons can couple. In general electron-phonon interaction has several consequences: (i) contribution to electrical resistance, (ii) modification of electronic properties such as eigenvalues and eigenstates of a single electron leading to the creation of polarons, (iii) mediated transition of effective electron-electron interactions and (iv) renormalization of phonon properties and effective frequencies due to a temporary absorption of propagating phonons by an electron. Moreover, in some solids phonons may cause an attractive interaction between electrons in a shell of the size of the Debye energy $\hbar\omega_D$ ($\hbar$: Planck constant, ω_D: Debye frequency) around the Fermi surface, which is a microscopic reason for superconductivity in a material. The drag effect is also known as phonon drag and is a thermoelectric transport effect known in semiconductor and metal materials. An electric current in a solid body is coupled to a shift in the Fermi surface of the electron system in the k-space. This shift is accompanied by an interaction between electrons and phonons, where phonons tend to remain in an equilibrium with the electronic system and thus being shifted in their own k-space.

Interactions between neutrons and X-ray diffraction are used to determine lattice structures. Measurements of the structural factor with neutron diffraction allows to determine the phonon spectrum of the material. Due to inelastic scattering character neutrons absorb or emit energy when scattered at the crystal lattice i.e., they can absorb and emit phonons. Higher diffraction contributions result in a continuous signal which leads to characteristic spectral peaks.

Even though the wavenumber of visible photons is much smaller than for phonons, visible light can be scattered under absorption or emission of phonons. Measurements of the Brillouin zone are performed under light diffraction, however only in the region of small wave vectors k. Visible light scattering at acoustical phonons is being referred to as Brillouin scattering, while scattering at optical phonons better known as Raman scattering. Moreover, phonon absorption leads to an increase in energy of the scattered light and contributes to the Anti-Stokes component of the scattering spectrum. Meanwhile phonon emission i.e., absorption of energy and momentum of a photon by the crystal lattice is referred to the Stokes contribution/component.

2.2.6 Link to macroscopic reality

Over the last decades experimental research has proven and extended the knowledge about phenomena induced by electromagnetic radiation or heat on semiconductor solids. In a study by V. Ryabchuk from 2004 the author summarized the findings concerning processes and existing particles on wide band gap semiconductors featuring a band gap of equally or larger than 3 eV. Thus, irradiation of solid semiconductor surfaces may lead to photogeneration of excitons or free charge carriers (s.Figure 4) being the origin of photoexcited surface reactions, while following different reaction and transformation pathways (s. Figure 5). Here charge carriers are generated due to absorption at fundamental absorption bands, intrinsic or extrinsic defect sites, as well as color center bands induced by UV light leading to the formation of active excited states responsible for photo adsorption and photo reaction. These states mostly feature trapped holes or electrons below the fundamental absorption threshold. This opens the possibility for wide band gap semiconductors to compete with relatively narrow band gap ones in respect to photocatalytic redox reactions. The presence of different surface states accompanied by strong coupling between electrons and phonons allow the formation of excitons at localized surface states which can transfer electronic excitation energy to reaction partners adsorbed on the surface. Therefore, complexes of excitons and adsorbates can be formed on the surface which can further react to products or intermediates. The formation of localized surface excitons and catalytically active centers going hand in hand with specific electronic pathways inside wide band gap semiconductors may show the similarity between heterogeneous photocatalysis and general semiconductor photochemistry.[32]

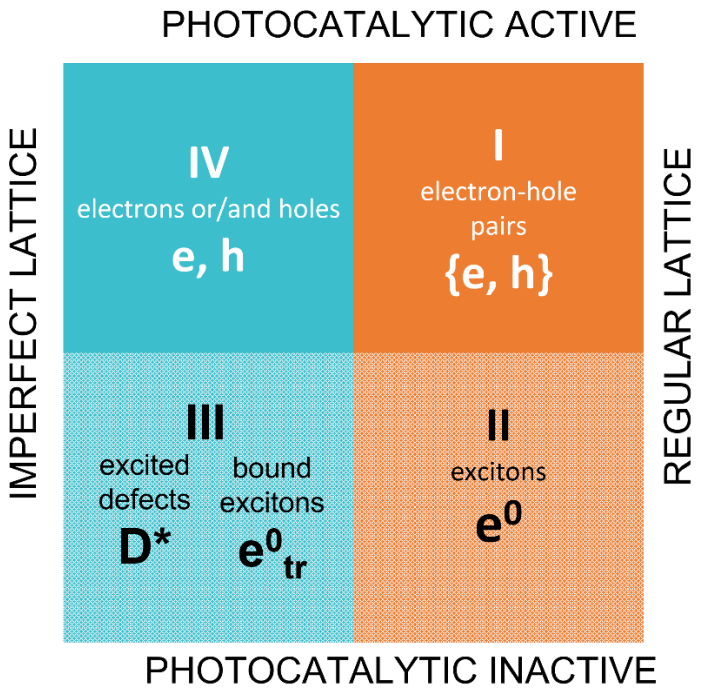

Figure 4: Simplified representation of possible types of electronic excitons in solid induced by absorption of electromagnetic irradiation. (modified from Ref. [32])

A crystalline lattice can show different kinds of imperfection influencing the X-ray beam by diffuse scattering. Besides impurities, defects, stress, or grain boundaries – for us one of the more interesting one is thermal vibrations of the crystalline lattice.[33] First mentions of it can be found as early as 1912. Sommerfeld *et al.* suggested the possibility of thermal motion of lattice atoms impairing the predicted diffraction patterns of Laue's subsequent X-ray diffraction experiment. However, Laue has proven them wrong. With proceeding time X-ray thermal diffuse scattering is being utilized to probe phonon dispersion relations, since it is directly connected to the lattice dynamics of the crystalline structure.

In 1967 Dawson suggested generalized structure factors for the crystal structure of ZnO wurtzite which also led to a detailed theoretical study of Mair & Barnea in 1975. Therein they investigated the origin of the pyroelectric properties of ZnO and suggested its connection to the anharmonic thermal vibrations of the atoms in the wurtzite-type structure, which is the separation between the mean position of an atom and its minimum potential. Moreover, an increase of the temperature led to a very small decrease of the axial ratio.[34,35] Kihara & Donnay extended the research and reported in 1985 that an increase in temperature from 293 to 473 K can lead to an increase in distance inclined to crystallographic *c* more than of the one parallel to *c*, while the angle of O-Zn-O bond remains constant.[36]

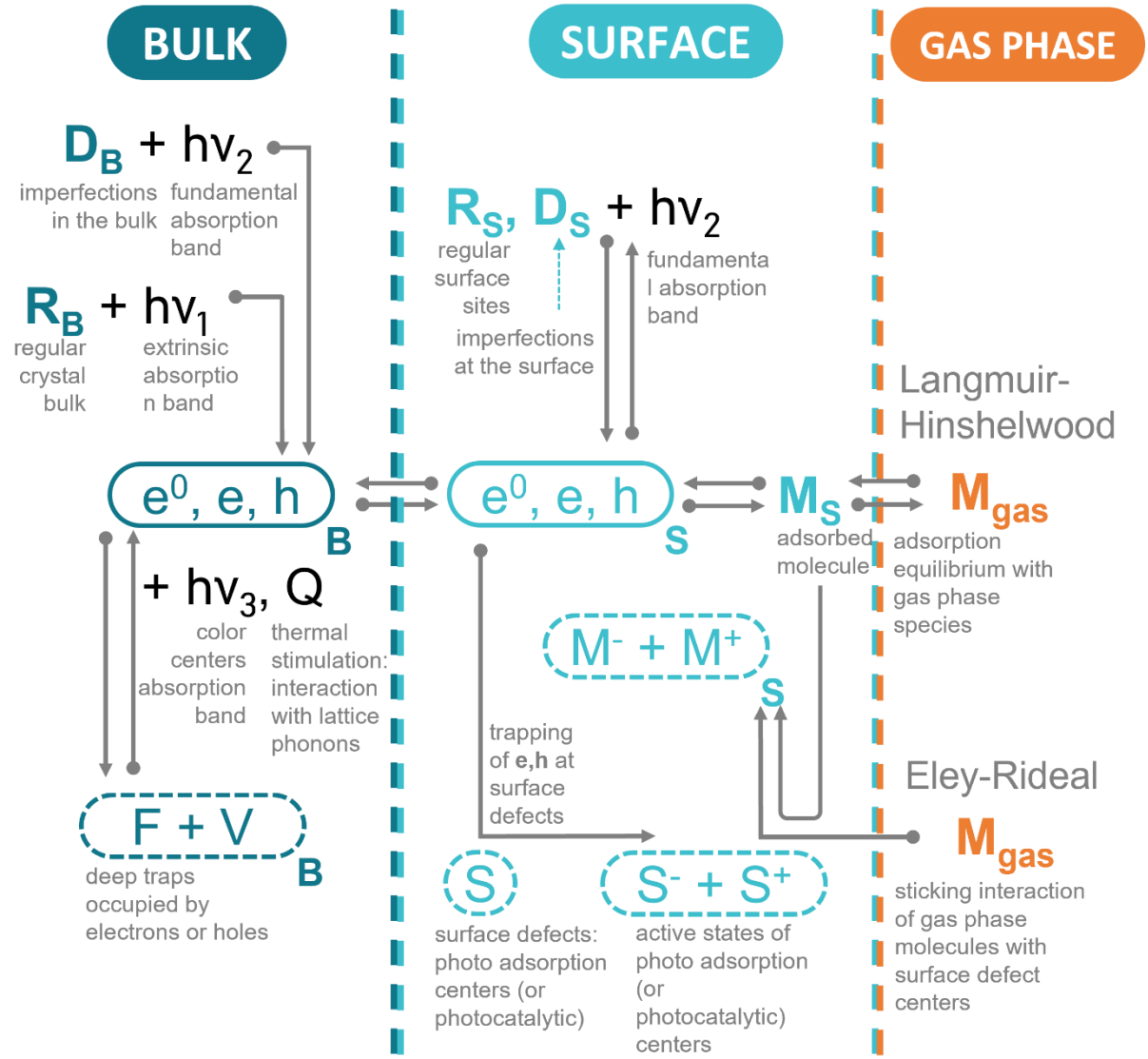

Figure 5: Photo induced processes on the surface and in the near surface area of wide band gap semiconductor photocatalysts. (modified from Ref. 32)

Surface phonon modes have been known for a long time. Yet in 1979 Hayashi made a first attempt to correlate features observed in infrared transmission spectroscopy with optical anisotropy and the shape of ZnO particles. Hayashi succeeded in providing theoretical estimation of ellipsoidal shapes which were in very good accordance with the results obtained from electron microscopy.[37]

2.3 CO_2 adsorption on metal oxide-based materials

Adsorption and desorption processes are two fundamental steps in heterogeneous catalytic reactions. Being often rate limiting steps, a lot of research dealing with them has been conducted over the last century. Investigations of adsorption of CO and CO_2 is therefore a topic which is being dealt with for more than 80 years.

Metal oxide materials have been of high interest for catalytic applications for a very long time. ZnO for example was utilized for the catalytic oxidation of CO e.g. in industrial waste gas treatment[38-40] or methanol synthsis.[41-48] The function of oxygen vacancies and defect sites(especially in latter example) is discussed, as they are supposed to be responsible for the catalytic activity in numerous reactions. In the recent years metal oxide materials have also been found to be active in (photocatalytic) reduction reactions.[16,49-52] As will be shown later (Chapter 2.4), in some proposed reaction pathways the first step of the photocatalytic reduction of CO_2 is the transfer of a single electron followed by the cleavage of a single oxygen atom and thus resulting in formation of CO.[13] Adsorption of CO_2 may lead to the formation of adsorbed carbonate species, which require lower initial energy due to change in structure – either due to bending of CO_2 and thus breaking the stable linear orientation of the molecule or the formation of carbonate and bicarbonate species utilizing the adsorbed hydroxide species present at the surface of metal oxides. It is supposed that oxygen vacancies and defect sites are very important for the photocatalytic reaction of CO_2, too.[49,53,54] Therefore, identification of adsorbed CO_2 and carbonate species may lead to finding reaction participants, intermediates, and adsorbed products, thus contribute to a better understanding of the reaction mechanism.

Despite several decades of research on adsorption mechanisms scientists all over the world were not able to surpass the ultimate efficiency of natures photocatalytic reduction of CO_2 i.e. photosynthesis conducted by plants. Nevertheless, this environmentally highly relevant research is continuing and every day numerous scientific works with minor breakthroughs are being published. Figure 6 gives an overview over the number of published articles dealing with this topic throughout the last 40 years. When CO_2 is present in the atmosphere it may adsorb on surfaces of metal oxide

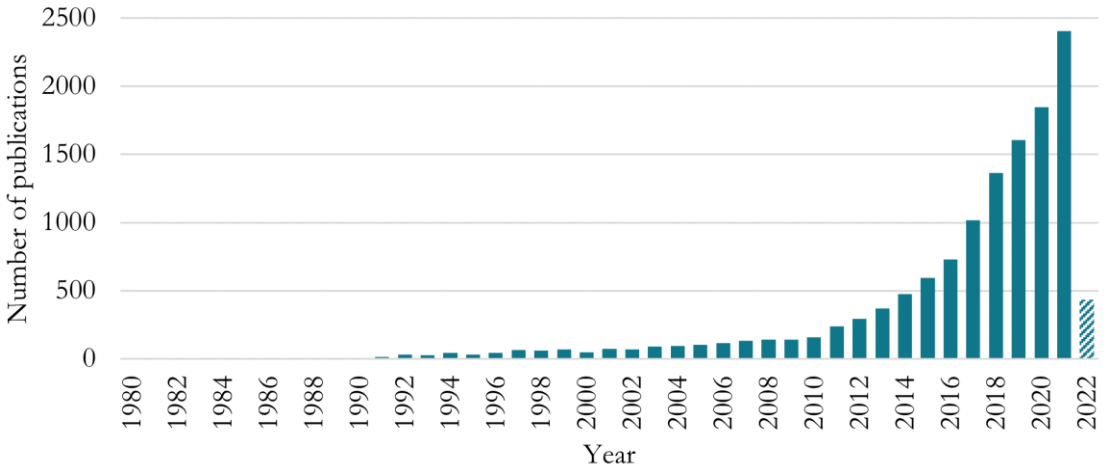

Figure 6: Number of scientific publications dealing with photoreduction of CO_2 between 1980 and 2021 according to Web of Science™. (Search conducted on 14.04.2022 as following: "carbon dioxide"(topic) and "photocataly*"(topic) or "CO2" (topic) and "photocataly*"(topic))

materials and while forming different kind of surface species, which are schematically summarized in Figure 7. CO_2 can be physisorbed retaining its unchanged linear orientation. Further, carboxylates and carbonates may be formed, while here one can distinguish between monodentate and bidentate carbonates. Surfaces which feature additional OH groups offer the possibility of monodentate and bidentate bicarbonates formation. Moreover, with increase in atmospheric CO_2 amount or exposure time different species may transform to other species, or already existing species may be rearranged to different and sometimes more stable ones. Changes in the system such as increased pressure, temperature or illumination with light covering the energy of e.g., the band gap of semiconductor material, may lead to formation of intermediates such as formate species.

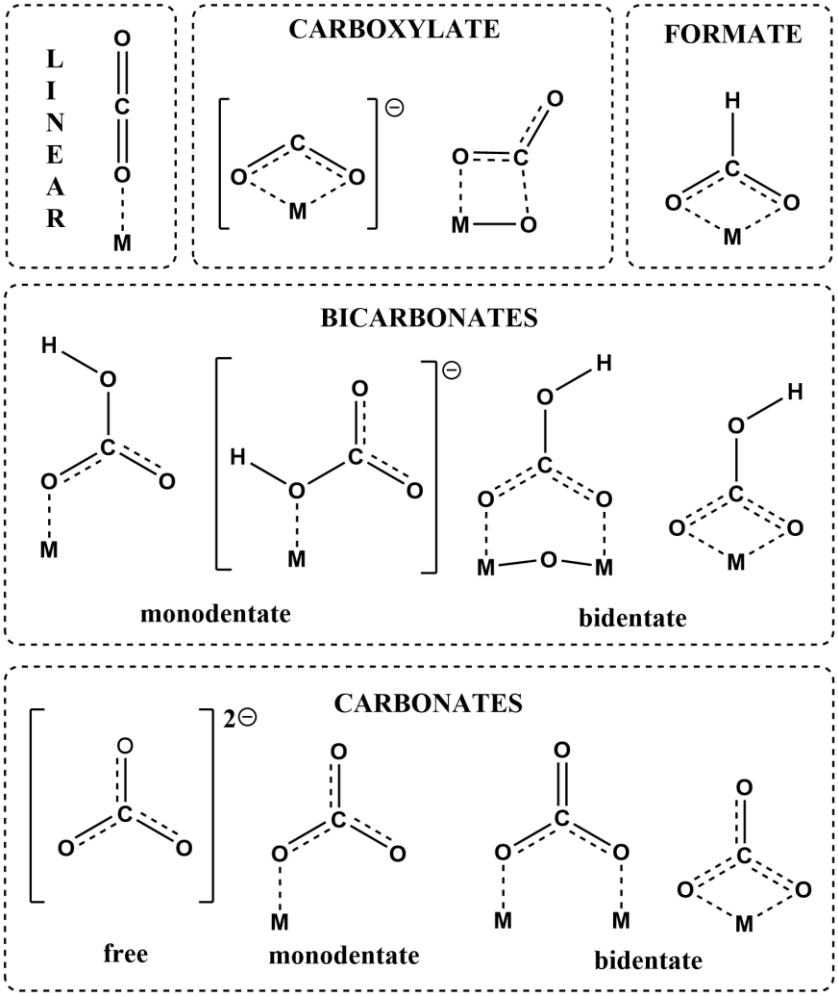

Figure 7: Schematic depiction of carbonate species formed on the surface of a metal oxide material as result of CO_2 adsorption.

2.3.1 Investigation of CO_2 adsorption by means of FT-IR Spectroscopy

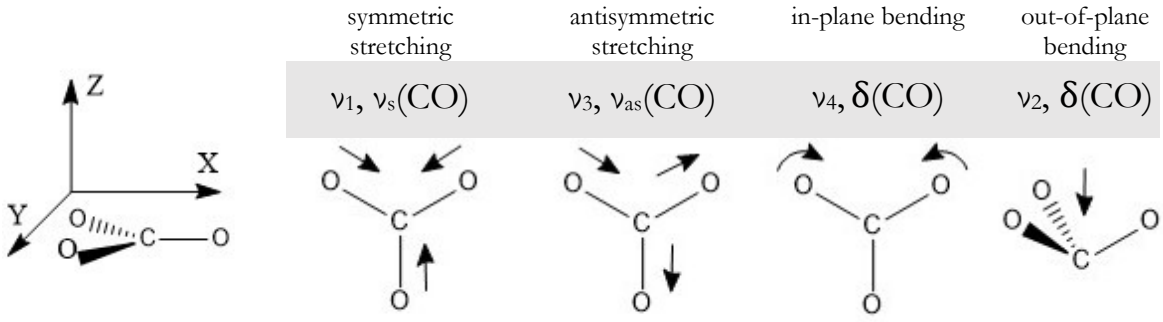

Figure 8: Four main normal vibration modes within a carbonate moiety.

Since FT-IR spectroscopy offers the possibility for investigation of molecular vibrations, it is a powerful tool for identification of organic species formed during CO_2 adsorption as well as reactions taking place on the catalyst surface. Selection rules for CO_3^{2-} leading to classification of the vibrational modes were first suggested by Nakamoto *et al.* in 1957.[55] Over the years this theory was refined leading to acceptance of four main normal vibration modes in a carbonate moiety which are also shown in Figure 8 in plane vibrations perpendicular to the z direction including a symmetric stretching(ν_1, ν_sCO), doubly degenerate antisymmetric stretching (ν_3, ν_{as}CO) and doubly degenerated in-plane bending (ν_4, δ(CO)), as well as out-of-plane bending (ν_2, δ(CO)) along the z direction. The author is well aware of the fact, that more than two atoms are required for a molecule to perform symmetrical as well as antisymmetrical vibration motions, i.e. ν_a(OCO) rather than ν_a(CO). However, here and in the following work the notation ν_a(CO) – which is very commonly used in literature – is utilized for antisymmetrical vibrations of CO molecular groups as with respect to further atoms or molecules connected to it. In addition to vibrational modes mentioned above deformation of CO-bonds or OH-bonds in COH groups as well as deformation of OH groups in (co-)adsorbed water molecules create spectral feature which are mostly found in the region of 600-1800 cm^{-1}.[56,57] Metal oxide-based materials may also interact with electromagnetic radiation and thus feature absorption bands mostly in the IR region below 1000 cm^{-1}. Hence, it is mostly possible to investigate molecular vibrations of adsorbed carbon containing species and organic compounds without any interference. However, some semiconductor materials may behave differently featuring strong absorption in the IR region above 1000 cm^{-1} e.g., when illuminated or heated. On one hand this phenomenon hinders identification of vibrational features, while on the other hand it may offer insights into electronic processes in semiconductor materials. It was therefore reviewed in a previous chapter and is a significant part of the work presented later.

As investigations of adsorption of CO_2 on metal oxide materials – and especially ZnO and TiO_2 – by means of FT-IR Spectroscopy has been done for many years, one could assume that numerous literature sources are available for the unambiguous assignment of features observed in the IR spectra to the corresponding vibrational modes which guide to the identification of adsorbed species. However, investigated materials reviewed in different studies often feature different (particle) morphologies and sizes with non-perfect surfaces rich in defects, steps, kinks and other adsorption sites. Moreover, adsorption temperature and coverage-dependent interactions between adsorbed carbonate species may influence the position of features. Theoretically, this results in slightly varying positions of features characteristic for specific vibrational modes of adsorbed molecules. Consequently, while exactly matching wavenumber values would be rarely available, a broad agreement on narrow spectral regions is expected. However, the reality is much worse as the assignment of features found in literature is often more or less random. While some works thoroughly assign the features to specific vibrational modes in each carbonate species[58], other do not even bother to mention the vibrational modes but just the species[59,60]. While in some studies adsorbed species are identified by the presence of e.g., only one vibrational mode[61] (leaving out the necessity of the discussion concerning any other vibrational mode), other adjust their assignment according to their spectrum moving the theoretical positions of features to questionable ranges, which however fit their needs[62]. While some authors precisely try to differentiate between bridging and chelating bidentate bicarbonates[58], some other summarize structurally different species like bidentate carbonates and bidentate bicarbonates under the name of bidentate carbonates only.[59] Consequently, over the years numerous suggestions for positions of certain characteristic features have been made of which some are summarized in Table 1(end of chapter, p. 25). Additionally, for a better visualization of the randomness in assignment Figure 9 and Figure 10 have been created. Figure 9 shows the wavenumbers reported for a range of metal oxide materials which certainly allows even more variability. Nevertheless, a rough trend which most assignments follow can be pointed out. Antisymmetric vibrational modes of OCO groups can be found at higher wavenumbers around 1550-1675 cm^{-1}. The corresponding symmetric vibrational modes of the same OCO groups is not always clearly apparent in IR spectra due to its low activity in IR measurements. Still, this feature is assumed to be positioned around 1350-1450 cm^{-1}. Additionally, as described earlier, some carbonate species might form bicarbonates which also feature an IR active deformation vibration of OH bond in COH groups producing a weak signal in the region of 1200-1250 cm^{-1}. Even though publications summarizing band assignments of adsorbed carbonate species on different metal oxide materials have been available since the 1990s[56,57],

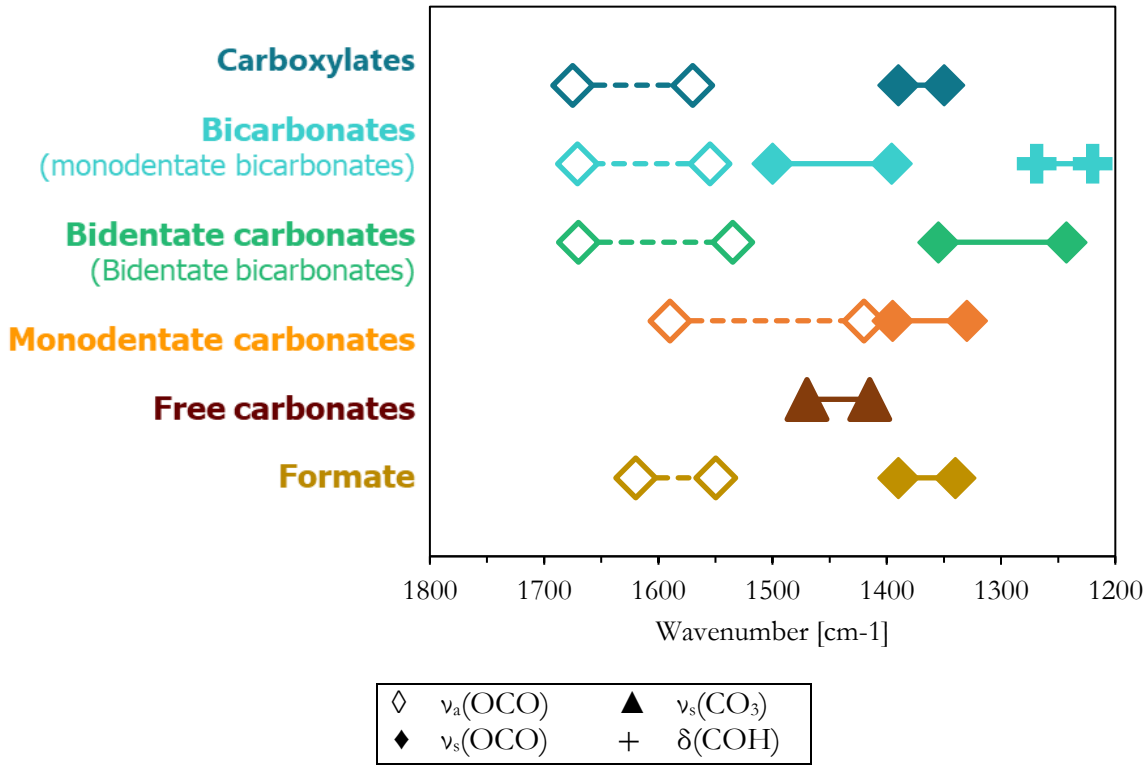

Figure 9: Schematic visualization of feature assignment to vibrational modes in different carbonate species formed on metal oxide materials due to adsorption of CO_2 according to the summary of literature sources up to 1992 by Turek and Wachs.[56]

wrong assignments have occurred in numerous works leading to propagation of wrong postulations. Figure 10 summarizes some assignments of characteristic features for adsorbed carbonate species on TiO_2 only which have been collected from literature sources published after 1992 (and with this after the study of Turek and Wachs shown in Figure 9). The author wants to point out especially the feature around 1245 cm^{-1} in Figure 10, which was assigned to a symmetrical vibration of the O-C-O bonding in a work conducted by Rasko *et al.*[63]. However, as this vibrational mode was suggested by other authors to be present in the region of 1400±50 cm^{-1}, this meant a massive shift of over 100 cm^{-1} compared to lowest reported value in previous works. It is reasonable to assume this to be a false assignment and to allocate this feature to a deformation vibration of an OH group instead. Moreover, this mistake led to a false assumption of carboxylate formation rather than (more reasonable) bicarbonate formation. Sadly, the work of Rasko *et al.*[63] was cited numerous times, resulting in propagation of a false assumption leading to suggestions of likely incorrect adsorption and reaction mechanisms.

However, even though the suggestions shown in Figure 9 were dominating the FTIR based research on CO_2 adsorption and carbonates for many decades, these are apparently not quite correct. Due to the rise of DFT calculations starting in the end of the 20th century it was shown

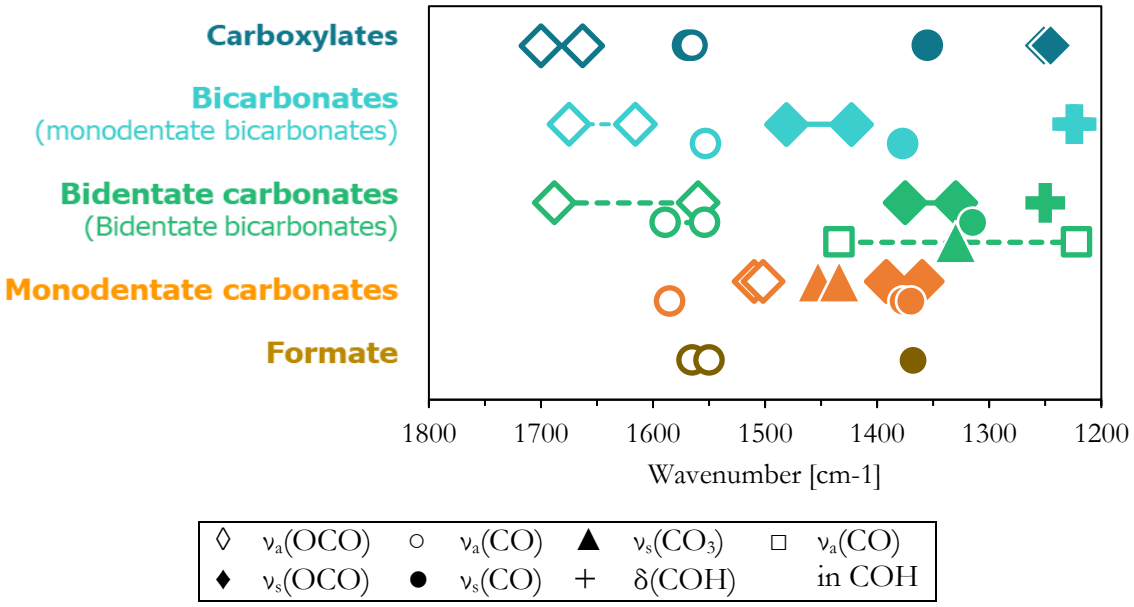

Figure 10: Schematic visualization of feature assignment to vibrational modes in different carbonate species formed on TiO_2 samples due to adsorption of CO_2 according to literature sources of the last 30 years as summarized in Table 1.

that even though the assignment of *groups* of spectral features to certain carbonates was not always wrong, the assignment of *single* spectral features to vibrational modes were partially wrong. Hence, two features at ~1600 and 1400 cm^{-1} do not originate from antisymmetric and symmetric stretching of the CO bond, respective, but rather from a splitting of the ν_3 antisymmetric vibration, as this vibrational mode is very sensitive to surroundings. While in studies dealing with CO_2 adsorption, more distinct features are observed for these vibrational modes, studies dealing with carbonate-based minerals such as calcinate[64] or cancrinite[65] observe rather broad signals with blue shifted weak signals. Therefore, the origin of the splitting has been a point of debate. Hellwege *et al.* suggested the appearance of an additional feature rather than splitting of a single feature due to combination of different Raman- and IR active lattice modes and internal vibrations.[66] Andersson *et al.* discussed the influence of surface-adsorbed water leading to an asymmetry of the ν_3 signal and thus to an additional feature blue-shifted with respect to the original band.[67] Additionally, small particle size of investigated samples affects shape, width and symmetry of IR features.[67-69] Further surface phenomena related to e.g. Ca-content in cancrinite was shown to influence the splitting and the position of the second signal originating from ν_3 mode.[70] However, while neglecting all of the previous suggestions, Xu *et al.*[64] were able to assign features found in experimental data using theoretical calculations at hand while accounting only for isotopic composition and the longitudinal optical – transversal optical (LO-TO) splitting. It is noted that research done by Xu *et al.*[64] deals with calcite ($CaCO_3$) but is still appropriate for discussion of single carbonate species. Further,

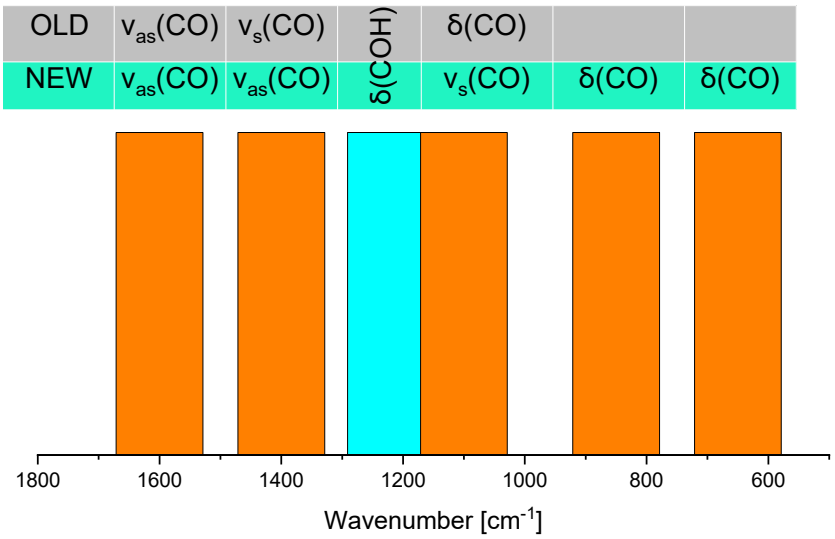

Figure 11: A comparison of spectral features assignment to vibrational modes in carbonate moieties with suggestions based on experimental works and new findings based on theoretical calculations. Width of bars does not give exact but roughly estimated ranges.

values for calculated frequencies deviate from experimental data by about 40 cm^{-1}. As they did not focus on exact numbers, but rather on band position *shifts* caused by isotopic substitutions, this systematic shift still allows qualitative analysis of the spectroscopic features. The results presented in this work are in good agreement with other computational investigations conducted earlier.[71] As already discussed earlier (Chapter 2.2.4), phonons contribute to vibrational spectroscopy. On the one hand electron-induced contribution to phonons may result in strong effects on the whole spectrum. On the other hand, single phonon modes may also contribute to vibrational modes of adsorbed molecular species. While contribution of TO phonons is detected in IR spectroscopy irrespective of incident angle and polarization of the IR beam, contribution of LO phonons is detectable only when a component of the IR beam is parallel to selected vibration.[64,72] During measurements of powdered samples featuring varying relative orientation of numerous particles a weak contribution of LO phonons is suggested to be observable anyway. Still, contribution to the splitting of the ν_3 feature by surface phenomena, combination modes and particle size dependence are not excluded and may be important secondary effects in quantitative and qualitative discussion of this phenomenon. Figure 11 shows the combined experimental and theoretical assignments of features found in IR spectra as a rough guideline when dealing with adsorbed CO_2 and especially carbonates formed on semiconductor surfaces. Here the assignment of two features at 1600 and 1400 cm^{-1} to two different vibrational modes being valid throughout the mid and end of 20th century is denoted as "old". "new" is represented by the more reasonable assumption of band splitting based on findings from geological and more recent computer simulated theoretical chemistry.

Table 1: Summary of feature assignment to vibrational modes in different carbonate species formed on TiO_2 samples due to adsorption of CO_2 according to literature sources of last 30 years.

	asCH	**sCH**	**asOCO**	**asCO**	**sOCO**	**asCO** in COH	**sCO3**	**sCO**	**dOH bCO** in COH
carboxylate			1700[79] 1675[62,63] 1671[82] 1670[75] 1663[81]	1569[76] 1565[79]	1251[62] 1245[59,75]			1355[76]	
bicarbonate			1675[77] 1667[76] 1623[62] 1616[79]	1553[59]	1481[81] 1434[60,75,76,81] 1423[59,62]			1377[59,61,63]	1222[73-75] 1224[76] 1226[59]
bidentate-carbonate			1688[59] 1675[60] 1639[76] 1566[62]	1589[75] 1585[61,77] 1573[59] 1554[81]	1375[59] 1363[81] 1355[62] 1330[81]	1434[58,80] 1222[58,60,62]	1330[61]	1315[54,60,75]	1250[49,59]
monodentate-carbonate			1510[62] 1502[79] 1465	1585[58,60,62]	1392[62] 1364[59] 1360[79]		1434[59] 1450[76] 1453[79]	1370[61] 1377[58-60,62,75,77]	
formate	2960[76] 2946[78] 2923[76]	2883[78] 2875[76]		1565[76] 1550[78]				1370[60,78] 1368[63,76]	

2.4 Side note: photocatalytic CO_2 reduction

According to Habisreutinger *et al.* photocatalytic reduction of CO_2 is not a catalytic reaction. Since it features energetically higher products than reactants, rather than being a downhill reaction with an activation barrier, one should refer to it as a sort of artificial photosynthesis. Unfortunately, the CO_2 molecule is due to its linear geometry, $D_{\infty h}$ symmetry and a closed shell electronic configuration a highly stable and inert molecule. The often suggested first step in the photoreduction reaction is a transfer of a single photogenerated electron to the carbon atom of the CO_2 molecule. This, however, would result in symmetry loss and repulsive interaction between the added electron and free electrons of oxygen and is therefore highly unfavorable. The required energy or chemical potential versus normal hydrogen electrode (NHE) for such a transfer is about -1.9 V, which cannot be provided by a single known semiconductor (s. Figure 12).

While a single electron transfer is virtually impossible, the photoreduction of CO_2 is achieved through mechanisms featuring several electron transfers – in natural as well as in artificial photosynthesis. It is supposed that adsorption of the CO_2 molecule to the surface of the semiconductor and the resulting interaction with surface atoms favors the formation of a $CO_2^{\delta-}$ adsorbate. Due to the bent structure the linear geometry is being broken, which leads to a lowering of the LUMO of CO_2 and thus a significantly lower energetic barrier for accepting a (photogenerated) electron. A large amount of research has been conducted (and still is) on adsorption of CO_2 on semiconductor materials throughout the last century and is being dealt with in the following chapter.

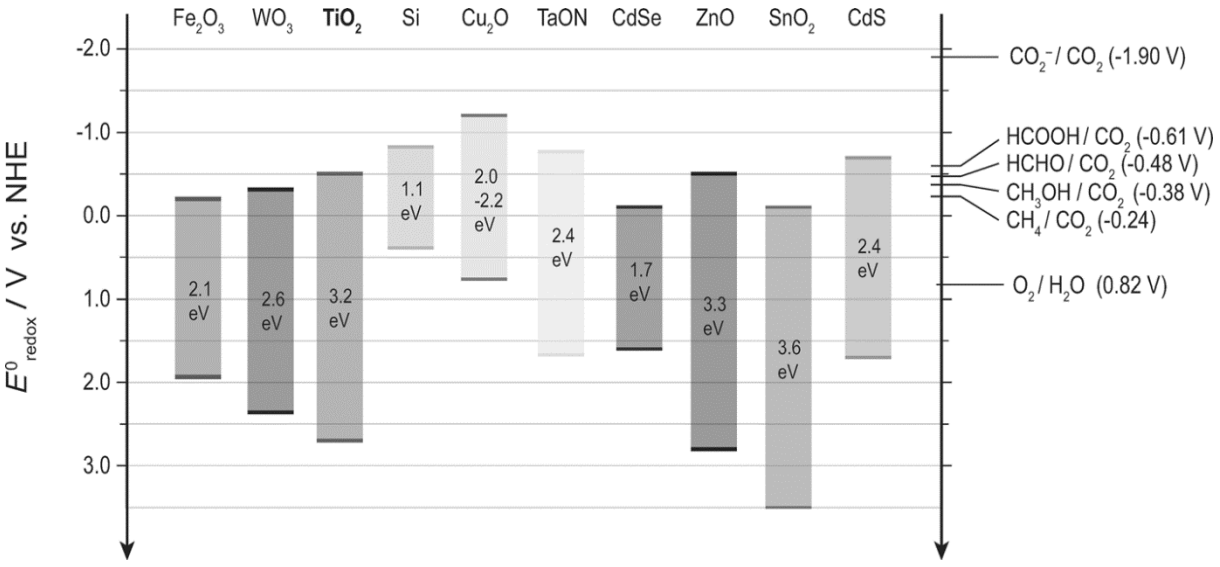

Figure 12: Conduction band, valence band potentials, and band gap energies of various semiconductor photocatalysts relative to the redox potentials at pH 7 of compounds involved in CO2 reduction. Adapted from Ref [13].

According to the state-of-the-art CO_2 photoreduction includes, apart from the very first electron transfer to the CO_2 molecule and depending on the reaction pathway, several one-electron transfer steps leading to a multistep process involving up to eight electrons and protons. Besides breaking existing C-O and formation of new C-H bonds the reaction results in formation of different products and intermediates. The reaction is often being conducted in presence of water i.e., liquid phase reaction or introduction of a water saturated gas stream. Here, however, the photogenerated electron is being consumed not only for the carbon reduction, but also for production of molecular hydrogen, which is therefore a direct competitor to the photoreduction of CO_2 and needs to be suppressed, if not needed. Table 2 summarizes most relevant reaction steps in the reduction of CO_2 and gives also the respective chemical potentials versus NHE.

While detection of CO, methane or methanol are often considered as proof of a successful reduction of CO_2, studies with a feedstock of $^{13}CO_2$ have shown also formation of ^{12}C products, which is probably due to residual carbon adsorbate coming from the synthesis procedure. Thus, attention is more and more drawn to proper catalyst preparation and cleaning of the surface prior to the photoreaction. Furthermore, it led to a rise in caution when reading about breakthroughs in CO_2 photoreduction reporting outstanding productivity numbers, which may simply be decomposition reactions of residual organics or UV-unstable rubber sealings without any proof of CO_2 consumption.

Table 2: Relevant steps in photocatalytic CO_2 conversion and respective chemical potentials versus NHE.

	$E^0_{redox}\ [V]$	transformation step
(1)	-1.90	$CO_2 + e^- \rightarrow CO_2^{\cdot -}$
(2)	-0.61	$CO_2 + 2H^+ + 2e^- \rightarrow HCOOH$
(3)	-0.53	$CO_2 + 2H^+ + 2e^- \rightarrow CO + H_2O$
(4)	-0.48	$CO_2 + 4H^+ + 4e^- \rightarrow HCHO + H_2O$
(5)	-0.38	$CO_2 + 6H^+ + 6e^- \rightarrow CH_3OH + H_2O$
(6)	-0.24	$CO_2 + 8H^+ + 8e^- \rightarrow CH_4 + 2H_2O$
(7)	-0.41	$2H^+ + 2e^- \rightarrow H_2$
(8)	0.82	$1/2\ O_2 + 2H^+ + 2e^- \rightarrow H_2O$

2.5 Thermal and Photo-induced effects on ZnO:

Following sub-chapters shall give a comprehensive and reliable view on the influence of UV light and heat on optical properties of ZnO mainly based on research conducted by scientists from Warsaw Pact countries throughout the 20th century. Moreover, the problems of language barrier and loss of knowledge are being addressed. An insight into processes of photodesorption and photoadsorption of oxygen and other gas phase molecules leading to changes in charge carrier states are outlined as well.

2.5.1 Introduction

In the course of the division after the Second World War a language barrier in chemistry emerged. Especially the Cold War was fostering new scientific communities which did not exchange scientific findings among each other due to political regulations.[83] The so-called Western Block consisting basically of the majority of countries allied with the USA published mainly in English, whereas the majority of the Warsaw Pact countries published in Russian. Therefore, over decades of scientific competition, exchange between the two systems became more and more hindered, following up to an almost non-citation policy of scientific papers from different systems at the end of the Cold War era. This mutual isolation inevitably led to the situation, that after the end of the Cold War, earlier work from the sphere of influence of the Soviet Union did not or barely find its way into science of the Western world basically due to a lack of language skills. In addition, even today scientists are not able to cite all original works from both systems because of the unavailability of printed of digitized original works from Warsaw Pact countries in most international libraries. Therefore, it is of highest importance to rediscover these scientific results by native speakers to ultimately overcome the language border and to broaden the scientific knowledge accessing all available sources.

The aim of this chapter is to restore scientific knowledge and fundamental findings in the thermal and light induced infrared (IR) blackening of zinc oxide (ZnO) from a variety of studies which had their origins nearly 100 years ago. Even though more recent studies on this topic are available, they often require a deeper understanding in the field of solid-state physics. Since most of the research conducted in the middle of the 20th century has been confirmed by more recent investigations featuring state-of-the-art equipment[84-91], insights into older literature offers a good basic understanding of some of these events and their origin, while being reliable.

A systematic study written in English that mentions IR-blackening of ZnO was published in 1985 by Rethwisch and Dumesic. Gas mixtures containing CO and CO_2 as well as CO, CO_2 H_2O were utilized to investigate the adsorption properties of metal oxide materials such as MgO, ZnO, Al_2O_3,

TiO_2 and SiO_2.[92] While most of these oxides were studied by means of IR spectroscopy at room as well as elevated temperatures (here up to 660 K), investigations of ZnO turned out to be fraught with difficulties. When heating the ZnO samples above 475 K the total transmittance decreased to 1% (so-called IR blackening) despite being transparent in air at temperatures below 475 K. Since this phenomenon occurred in both gas streams (CO + CO_2 and CO + CO_2 + H_2O in He), the formation of zinc carbonates was assumed to be the main reason for this phenomenon. Even though, by the year 1985 this effect had been well explored for over 50 years by Russian scientists, neither Rethwisch nor Dumesic, nor any of the reviewers apparently ever heard about it before, which led to the publication of false assumptions. Nowadays, the phenomenon of IR blackening of ZnO samples in reductive atmospheres or upon irradiation with UV light, respectively, is still being considered a novel and insufficiently investigated effect by many scientists in the western world.

2.5.2 Early sorption experiments on ZnO

Investigations on adsorption and desorption processes influenced by irradiation have been conducted as early as 1930. German solid-state physicist Erich Mollwo (1909-1993)[93-95] and his Russian physical chemist colleague Alexander Nikolaevich Terenin (Александр Николаевич Теренин, 1896-1967) were one of the first who thoroughly investigated photoinduced phenomena in ZnO. However, Mollwo and especially his future student Claus Franz Klingshirn (b. 1944) focused more on the electronics of the material. Terenin on the other hand did a large part of his research on events and phenomena caused mainly by UV irradiation of ZnO, i.e. within its absorption region at 385 nm. In 1946, Terenin retrospectively described his decision for this certain specialization with the following words (English translation and adaptation from the Russian original):

"Due to limitations of existing characterization methods, it felt natural to turn to the field of irradiation phenomena in order to develop and investigate the problems of adsorption and catalysis. This aim was set in the Institute of Physics at the Leningrad University in the early 1930s. It was set to utilize different optical and spectral methods for the investigation of main questions concerning the state of gaseous molecules during adsorption, namely: a) the degree of torsion or structural changes, b) processes of exchange of energy between the molecule and the solids and last and foremost c) chemical reactions taking place on the surface."[96]

Changes of adsorption properties under influence of irradiation were found for a wide range of metals, semiconductors, and dielectrics. The effect is very specific i.e., follows a certain direction (photodesorption or adsorption). The general size of the effect and the according kinetic parameters depend on the nature of the adsorbent material, the adsorbate as well as the preparation

procedure of the surface, spectral range of the active irradiation etc. In earlier works it has been demonstrated that adsorbed molecules are more active from a photochemical point of view, as solid semiconductor adsorbents are capable of dissociation of adsorbed molecules due to the absorbed irradiation energy.

By the year 1935, Terenin established four main processes taking place on the surface of a semiconductor solid being in contact with a gas phase upon irradiation: 1) photodesorption of gas molecules without any reaction and thus structural changes of adsorbate and adsorbent; 2) photo sorption of gas molecules under absorption of light by the solid; 3) photo dissociation of adsorbed gas molecules and adsorbed surface species; 4) photo reaction of adsorbed species on the irradiated surface.[97,98]

The system O_2-ZnO has been investigated and studied in detail over the last decades. It is assumed that high catalytic activity of ZnO, as a typical wide band gap n-type semiconductor, in photocatalytic oxidation reactions is based on the photoactivation of adsorbed O_2.[99] Investigations of photoadsorption and desorption processes have provided valuable information about properties of adsorption centers, bond strengths in the adsorption complex as well as characteristic electronic and molecular processes on the surface. According to Lisachenko and Skornyakov[100] the irradiation can exert its influence very selectively, which allows to alter only specific coexisting forms of adsorption. This gives a fundamental ability of directional formation of surface structures and surface properties.

Electrophysical properties of ZnO and its surfaces highly depend on the amount and strength of the adsorbed O_2, which is assumed to create local acceptor levels inside the band gap of ZnO. The shift of the adsorption equilibrium under influence of light leads necessarily to a redistribution of charges on the surface states likewise of the adsorption and non-adsorption origins. In particular, photodesorption of O_2 induced by irradiation with UV light was utilized to explain the formation of extremely excited layers in the region of surface charges[101,102], photoconduction[103] and increased absorption in the IR region[104,105]. A brief summary of all reported effects as well as the scientists conducting research of these topics, respectively, can be found in

Figure 13.

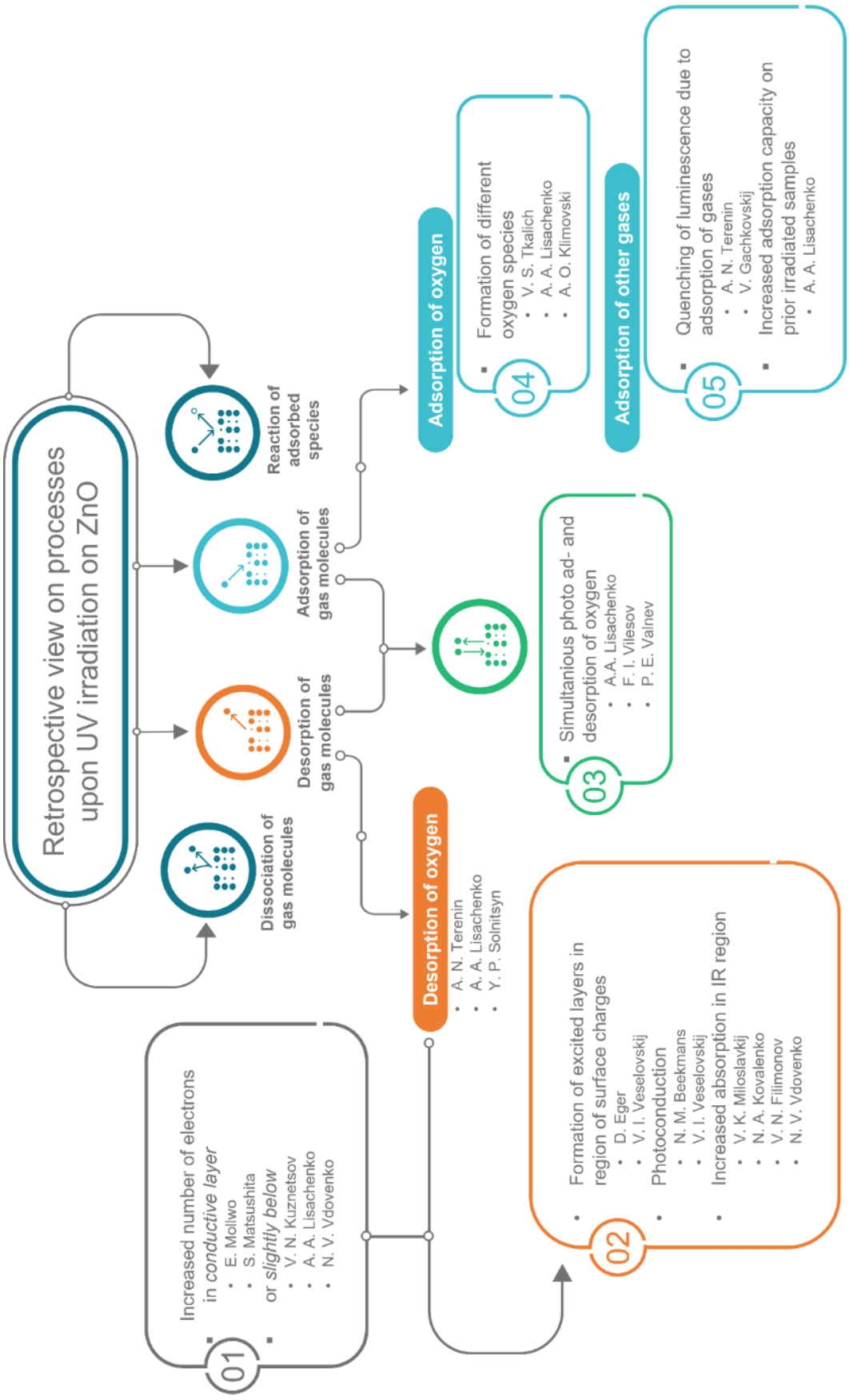

Figure 13: Overview of events occurring during UV irradiation of ZnO, the resulting effects and the respective scientists who observed these effects as discussed in this chapter.

2.5.3 Photogalvanic effects in ZnO

In 1947, Veselovskij provided insights into the photoconductivity of ZnO.[102] Based on its high efficiency he suggested that the absorption of UV irradiation takes place not only on the very surface layers of the material being in contact with adsorbed reactive species, but also in the nearby bulk material. His hypothesis was confirmed by the decrease in measured transmission of the sample. Furthermore, he conducted investigations on the photogalvanic properties of anodic polarized Zn electrodes in an electrochemical circuit. The spectral sensitivity was shown to match quantitatively the absorption spectrum of ZnO, which means ZnO is the light absorbing compound in the observed photoelectrochemical process. Moreover, the measured effective charge in the anodic Zn electrode underlines the reaction taking place in the monolayer, which determines the potential of the electrode in this region. Following these findings, a scheme of the process was derived: A pair of charges created due to absorption of a photon is passed to the ZnO/metal and ZnO/solution interface following the mechanism of the photoconductivity. Here, the electrons are passed to the metal and the holes to the solution, where the electrochemical act of discharging of the adsorbed monolayer of reacting complexes takes place. The degree of the last heterogeneous process is utilized to determine the changes of the potential depending on the amount of photo galvanic current which passes through. The absorbing component is the volume, while the reacting part is the adsorbed monolayer on the surface of the ZnO crystal.

2.5.4 Influence of UV irradiation on the IR spectrum

Separately from each other, Filimonov as well as Miloslavskij and Kovalenko found that ZnO has a specific, broad and non-selective absorption feature in the IR region.[104,105] Irradiation with UV light in vacuum induced enhanced absorption of infrared light in the range starting from 2500 cm^{-1} and reaching a nearly full absorption at 500 cm^{-1}. This absorption disappeared when the sample was brought in contact with O_2 or other reactants like NO or quinone, and this behavior could be reproduced several times in a row. Irradiation with UV light in presence of O_2 or air increased the IR absorption as well, however to a much smaller extent. The increased absorption disappeared when the irradiation was turned off. Thermal treatment of the sample at 575–675 K in reductive atmosphere (CO, Ar or in vacuum) led to the same effects. Since thermal degassing leads to a weaker appearance of the effect, but also starts at temperatures around 575 K, increased absorption has been solely assigned to photodesorption of O_2. It was assumed that desorption of O_2 leads to an increased amount of electron density in the conductive layer or donor level, which priorly were held by adsorbed O_2. A simplified scheme of the observed effect of increased IR absorption is

shown in Figure 14 Similar effects were reported for an increased amount of interstitial Zn in ZnO.[106-108] Further the increased absorption in the IR region was assumed to originate either from an electron transition between a local donor level to a conductive level, or a transition inside the conduction band. Consequently, these absorption phenomena were coupled to the increased number of conduction electrons.

In another study by Miloslavskij and Kovalenko specific absorption of ZnO in the IR region was observed as well.[104] The samples investigated in this study were synthesized by chemical vapor deposition. Depending on the speed and atmosphere of the synthesis, samples with different amounts of excess Zn were prepared. The excess Zn was shown to be directly responsible for lower resistivity and thus higher conductivity. Moreover, it was found that the change of resistivity was directly coupled to the specific absorption of light in the IR range. The authors were able to further alter the conductivity by thermal treatment or irradiation with UV light. By this the absorption of the IR light was altered as well, which again was suggested to be coupled to the number of conduction electrons. Furthermore, the authors suggested the presence of excited states below the conduction band, where not fully excited electrons might be trapped and being further excited by IR light reaching the conduction band and contributing to the increased conductivity.[104]

In a study by Kuznetsov and Lisachenko the creation of so-called "color centers" was assigned to electrons in the conduction band.[109] ZnO samples were thermally treated in H_2 or CO and with increased thermal treatment strong absorption in the IR region was detected, reaching its maximum

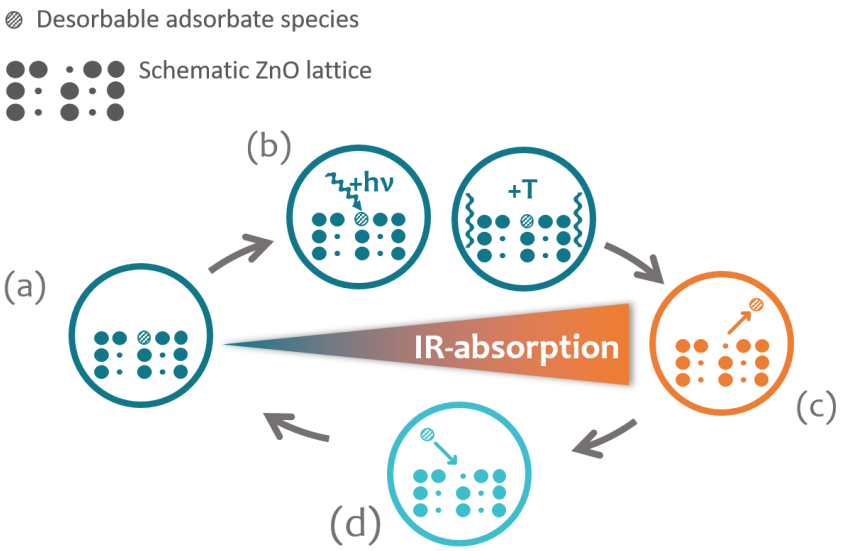

Figure 14: Schematic depiction of reasons for increased IR absorption in ZnO: (a) ground state, (b) UV irradiation or thermal treatment in reductive atmosphere, (c) desorption of adsorbed species (e.g. oxygen), (d) adsorption of electronegative gas phase molecules.

at around 600 K. Thermal treatment in a reductive atmosphere led to the oxidation of H_2 or CO, resulting in the reduction of the ZnO surface and thus an increased number of electrons in the conduction band or slightly below it. Since the effect appeared in either of the two gases, the increase of absorption in the IR region due to the formation of adsorbed surface carbonate species and complexes was excluded. Vdovenko *et al.* confirmed these findings, as they reported an increase of absorption in the IR region (also referred to as increase in reflectivity) upon heating of ZnO samples in vacuum or reductive atmospheres like CO or H_2.[110]

2.5.5 Influence of UV irradiation on the adsorbate bond strength

The possibility of increasing the bond strength of gas phase molecules with semiconductor surfaces due to irradiation with UV light might not only have its origin in the presence of negative (or positive) charge on the surface - which is created as a result of charge separation due to absorption of a photon - but also due to the appearance of free valences or radicals due to bond breaking of previously adsorbed and released species.[98] Lisachenko observed an increase of the adsorption capacity of prior irradiated samples which confirmed the earlier reported "memory" effect of photoadsorption i.e. formation of adsorption centers as a result of the localization of non-equilibrium carriers on the surface states.[111] Desorption from the irradiated sample led to a decrease of the amount of oxygen in the adsorption layer and is not a result of a photochemical reaction with participation of oxygen containing molecules (H_2O, CO, CO_2). Verification experiments conducted in this study showed a quantum, non-thermal nature of this effect.[111] In conclusion, photodesorption of O_2 was identified in the binary system O_2-ZnO. By photodesorption a significant amount of surface oxygen could be removed, also partially strongly adsorbed species. Moreover, this effect was not detected in earlier studies[112-114], which can be explained by the presence of masking, competitive processes. Thus, utilization of the photomanometric method was not very effective, due to the strong contribution of quantum yield of reversed photoabsorption taking place at the same time.[115] Liberation of CO_2 in prior experiments of Shapira[114] evidenced cleaned surfaces and the consumption of photoactivated oxygen for oxidation reactions of carbon containing impurities.

2.5.6 Detecting and distinguishing oxygen surface species

Tkalich, Lisachenko and Klimovski reported in 1982 the presence of different oxygen species after photoadsorption of O_2 on ZnO samples.[116,117] By conducting temperature-programmed desorption (TPD) measurements as well as photoactivated isotopic exchange studies they were able to assign at least three different oxygen species.[116] Low temperature species which featured desorption at

T < 360 K effectively "monitored" the gas phase species but did not interact with the surface oxygen. High temperature species which did not track the isotopic content of the gas phase due to their high binding energy led to a high activation energy for the desorption and thus being desorbed at T > 430 K. Species being desorbed at 410 K were considered for being the main contributor to the photoactivated isotopic exchange of O_2 at T ~300 K (see Figure 15). These species featured the capability of interactions with surface O_2 as well as with the gas phase species.

In a study with isotopic labeled ^{18}O oxygen Lisachenko and Viselov reported simultaneous photoadsorption and photodesorption of O_2 under irradiation with UV light, even though barometric measurements indicated an exclusive photoadsorption process.[115] The sorption behavior was shown to be not two independent processes occurring at the same time, but two directions of the same process featuring desorption of strongly bound lattice oxygen under irradiation. This led to the activation of isotopic exchange of lattice oxygen in ZnO by O_2 present in the gas phase. Stabilization of a certain O_2 pressure during irradiation did not result in the termination of the photoactivated isotopic exchange, but a stabilization of the adsorption-desorption equilibrium. Heating of the sample due to absorption of UV light was ruled out as the origin of the isotopic exchange, since similar results required a temperature of at least 525 K. However, the irradiation used for the experiments was not able to heat up the sample in vacuum by more than 10 K.

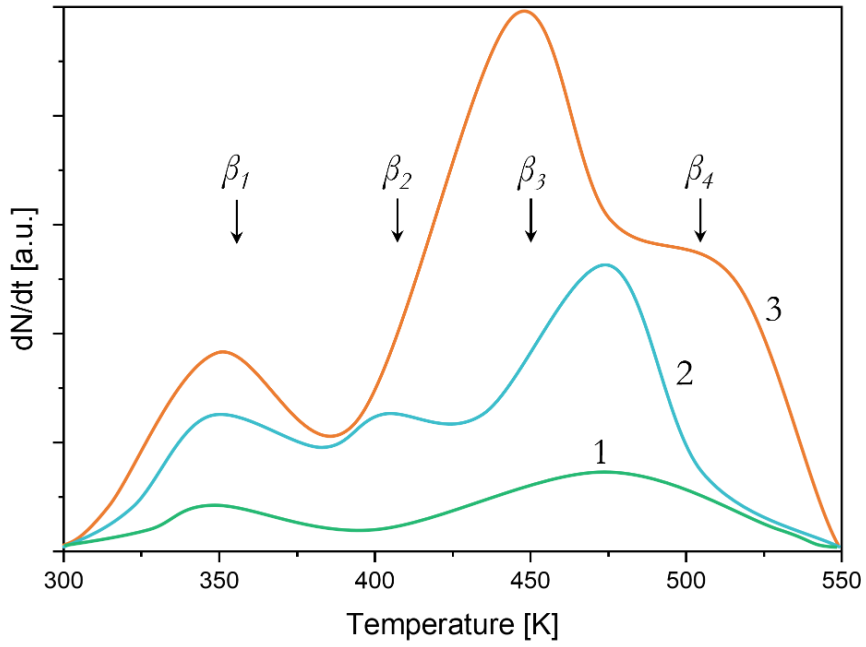

Figure 15: Thermal desorption (TD) spectra of O_2 on non-illuminated (1, green) and illuminated (2, blue; 3, orange) samples. Isotopic content of thermodesorbed O_2 after adsorption in the dark (1), adsorption in the dark with subsequent holding in O_2 (2), adsorption of O_2 in the dark with subsequent holding in ^{18}O-rich O_2 (3) Figure reproduced and modified from literature[116]

In general, great efforts were undertaken to make sure, that the origin of all observed events was of quantum nature rather than temperature driven. In order to distinguish the two possible causes of desorption, it was instructive to consider the wavelength range required to activate the process, which was in the short UV region. This differentiation was investigated by a direct experiment, which successfully showed that thermal desorption due to irradiation is followed by direct re-adsorption of desorbates, while photodesorption exhibits a rather irreversible character due to slow electronic processes at the surface and bulk, but also due to low partial pressures and thus slow re-adsorption processes.

In 1982, Lisachenko conducted further studies on photoadsorption and -desorption of O_2.[100] Samples were treated with O_2 at 775 K for at least 50 h. Afterwards the reaction chamber was evacuated to $p \leq 6\ 10^{-8}$ Pa followed by a TPD experiment in vacuum. The sample was irradiated either prior or after introduction of O_2 as well as during the linear heating. Taking into account his earlier findings[118], the author was able to separate the graph in the range of 300-600 K in at least 7 different peaks. Starting from 620 K the desorption peak was assigned to an increased formation of defects due to the loss of structural lattice oxygen and thus resulting in nonstoichiometric ZnO, which was later confirmed by Kuznetsov *et al.*[110] Irradiation prior to introduction of the O_2 increased the adsorbing capacity of the sample as can be seen in Figure 16, spectrum 2. In comparison to the non-irradiated sample a relative increase in the population of high-temperature ($T > 420$ K) species was noted. Irradiation of the sample after adsorption of O_2 resulted in an increase of molecular O_2 pressure in the gaseous phase meaning a photodesorption of oxygen.

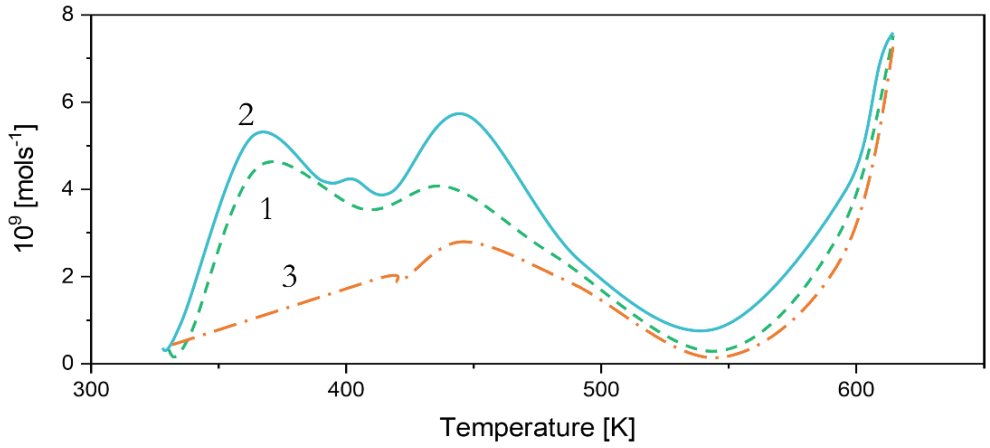

Figure 16: Temperature-programmed desorption (TPD) spectra of molecular O_2, adsorbed at 300 K on non-irradiated sample (1), on irradiated sample (2), and after illumination of the sample with adsorbed oxygen (3). Figure reproduced from literature.[100]

The TPD spectrum 3 in Figure 16 differed from spectrum 1 by much lower overall coverage of the sample with oxygen. While low temperature oxygen species were nearly completely photodesorbed, high temperature species were still present, however, to a diminished degree. A control experiment was conducted, where the sample was heated to 420 K in vacuum prior to irradiation at 300 K in order to ensure the removal of low temperature species. During a subsequent irradiation a pressure increase was detected. From this the authors assumed that high-temperature oxygen species are also being photodesorbed. Additional TPD experiments were performed where the sample was irradiated with light of different spectral ranges. It was shown that irradiation with light in the absorption range of the material was most efficient at temperatures below 520 K. Moreover, the intensity of the short wavelength part of the photodesorption correlated with the amount of O_2 desorbed during the thermal desorption experiment to a temperature up to 520 K. When proceeding to higher temperatures the range of maximum activity shifted into the visible light range. Results of the work were in good correlation to theoretical calculations reported by Tokoro *et al.*[119]

2.5.7 On the mechanism of oxygen photodesorption

In case of a metal it is assumed, that the large energy quantum of UV light needed for the desorption process is characterized by the deactivation event of transformation of the electronic excitation to vibrational degrees of freedom in the solid. This process occurs in parallel to the breaking of the bond between adsorbate and surface. For a semiconductor, the conditions are even more favorable, since the adsorption site is mostly on the surface and thus energetically separated from the bulk. Consequently, on a surface site the absorbed photon may be in the spectral range not covering the required energy of the bulk crystal structures. Thus, the weakening of bonds on the surface and following release of the adsorbate into the gas phase is even more probable in case of non-metallic crystals.[98]

Photodesorption of O_2 on ZnO was found to be favorable on samples with excess metal content.[120] Photodesorption from metallic Zn was reported as well, when the sample featured a thin oxide layer. However, keeping the metallic sample in contact with O_2 for several hours led to a blocking of photodesorption, which could not be restored neither by introducing fresh O_2 nor by heating to reach full oxidation of the sample. Photodesorption can take place also when irradiated with light of the infrared region 1000–2000 nm, however the effect is much less pronounced compared to when irradiated with UV light <400 nm. Up to 1959 it was assumed that adsorbed O_2 was acting as an electron trap leading to an overall electronegative charge of the surface. Thus the negatively

charged O_2^- molecule is strongly bound to the surface unable to dissociate except when it rejects an electron, which is possible in case of migration of an exciton to the surface.[120]

A detailed discussion of the mechanism of photodesorption has been reported by Lisachenko *et al.* in 1982.[117] The process of photodesorption includes steps of absorption of photons, transfer of the energy of the excited state to the adsorbent-adsorbate bond and the breaking of the bond. Since O_2 is not active in the visible or near UV region, the possibility of direct photodesorption originating from direct light absorption of the adsorbate can be excluded. The adsorbing sample has the role of the spectral photosensitizer and photodesorption is being initiated because of the shift of the electron-hole equilibrium due to the irradiation in the near surface region. Discharging of the adsorbate takes place in a much longer time than the bond vibration between adsorbate-adsorbent. Such a model unambiguously explained the main effects in the region up to 520 K i.e. the maximum efficiency in the absorption region of ZnO, linear dependence of the rate of photodesorption to the intensity of the irradiation and the fractional coverage by adsorbed oxygen of the surface. However, the proposed scheme could be transferred to the region over 520 K, since here the dissociated species (O^-, O^{2-}) of adsorbed oxygen are the stable ones. Taking into account the results of Basov *et al.*,[111] which showed that absorption in the visible region leads to a discharge of surface O^- anions, a mechanism for the process in the high temperature region above 520 K was assumed. The mechanism qualitatively explained the superlinear dependence of the rate of photodesorption from the intensity of irradiation, the overestimation of the action spectrum next to the limit of self-absorption in the long wavelength range as well as the connection of the rate of photodesorption with the amount of high temperature adsorbed O_2.[100]

Desorption of hydroxyl radicals was observed by time-of-flight mass spectroscopy on pulsed irradiated ZnO samples.[121] The samples were heat treated for a very long period of time in order to clean the surface completely. Afterwards the surface was saturated with either H_2O or CO. After irradiation hydroxyl radicals were detected which was explained by either bond breaking of surface hydroxyl groups and subsequent desorption of those, or by decomposition of adsorbed water molecules. When CO was pre-adsorbed, CO_2 was mainly detected as desorption product rather than CO. Light driven desorption was verified by heating the sample instead of irradiation. From this observation the authors concluded the interaction of light with adsorbed molecules, which resulted in decomposition or/and desorption of those. Interestingly no photodesorption of O_2 was detected. This was in good agreement with findings reported by Solnitsyn, which showed that oxidized samples featured a characteristic photoadsorption rather than photodesorption while thermal desorption was still "viable".[122]

2.5.8 Fluorescence quenching through adsorption of gas molecules

Studies on fluorescence quenching have been conducted by measuring fluorescence spectra of evacuated ZnO through addition of different gases and influence of temperature.[98] Unlike iodine, oxygen had a moderate effect on the fluorescence spectra. This confirmed early findings, that even though CO is reacting with the ZnO by forming surface carbonates, it has no quenching effect on the fluorescence of the sample. Further it was shown, that quenching of the fluorescence in ZnO can be achieved by simple heating, where the initial fluorescence intensity dropped to zero at 335 K already.[123] By the end of the 1950's a common band diagram was accepted throughout the research field. Here upper local levels $Zn(Zn^{+}\text{-}e)$ are being created by excess atoms of Zn – i.e. interstitial Zn which can release electrons of dark conductivity.[93] Lower levels are denoted as $Zn^{+}(Zn^{2+}\text{-}e)$ and belong to excess Zn ions, which are assumed to be centers of photo conduction and luminescence.[124] In other words, irradiation of the sample leads to the release of electrons, which end up in the conduction band.[93] From the conduction band excited electrons recombine with Zn^{2+} and reach the excited Zn^{+} state, followed by release of luminescence light reaching the ground level back again. When adsorbing electronegative molecules on the surface of ZnO additional electron trap states or levels are being created. These states, owing their electron affinity to the adsorbed electronegative molecules, are being filled by electrons in the dark already, which are being transferred to them from local levels of Zn. Consequently, on the surface of the semiconductor a bilayer is created leading to the bending of the bands. This leads to an electron drought in the boundary layer due to the potential barrier, rejecting those form the surface. Under the influence of an absorbed photon, which is migrating in form of an exciton to the surface on ZnO, a release of electrons from centers of photo effects of Zn^{+} with transfer of the electron to the conduction band is assumed. As a result of the electronic drought of the boundary layer the recombination with ionized centers followed by luminescence radiation becomes more difficult. Ionized luminescence centers Zn^{2+} recombine with electrons from trap states created by adsorbed electronegative molecules without any emitted radiation. While the described process leads to quenching of the luminescence, it also results in an increased duration of the photo effect due to increased lifetime of electrons in the conduction band. With a decreasing number of electrons in the trap states the barrier height is decreasing as well, which leads to a migration of electrons to the surface and thus filling the emptied states created by adsorption. By this the theory of Morrison[125] is being proven wrong in which O^{-} is trapping an electron, since the connection of the electron to O^{-} in the gas phase would require an energy of 9 eV, which excludes the possibility of this process, even when adsorbed.[125] Further it was assumed that absorption of a photon by the crystal creates an exciton which migrates to the surface. Here it induces a discharge of negatively charged

molecular ions on the surface due to transition of electrons into the conduction band. Photodesorption of electronegative surface molecules removes surface trap sites, which are the reason for quenching of the luminescence, followed by an ignition of luminescence. Water can also act as an electronegative adsorbate and thus create additional surface trap sites, since in its free state it has an electron affinity of 1 eV, and in the hydrated state the affinity is even higher. Interestingly, adsorption of dry molecular O_2 did not lead to quenching of the luminescence, however coexistence of molecular water on the surface did. It was assumed that trap states created by dry O_2 only are at much too high energetic states to trap electrons form local interstitial Zn atoms. Additional adsorption of water, especially capillary adsorbed water, results in a hydration of O_2 molecules, which leads to a decrease of the electronegativity, which is equal to an increase in the electronic affinity of the initial O_2 molecule. As a result, the vacant level provided by O_2 is being lowered to a state where it can accept a transition of an electron and thus quenching of the luminescence, as described above[123].

In 1995, Lisachenko and Aprelev finally confirmed the presence of electronic surface states in the forbidden region between valence and conduction band of ZnO utilizing UV photo electron spectroscopy.[126] As their results matched earlier findings from investigation utilizing other spectroscopic methods conducted by them and other groups, they were able to assure the specialties of the photo electron spectra originating from the energetic spectrum of filled surface states (and not from scattering or other mechanisms suggested to date).

3 Results and Discussion

3.1 Design, modification and verification of test stands

3.1.1 Piping for gas supply

In the course of the work at hand different experimental set-ups have been build: (i) *in situ* DRIFTS set-up, (ii) *in situ* photo-TPD set-up, (iii) *in situ* ATR-IR set-up and (iv) a photoreactor. While the set-up (i) and (ii) have been utilized for investigation of powdered samples in gaseous phase, the latter two did not find utilization during this work. In the following chapter the set-ups (i) and (ii) will be discussed in detail. Information about set-ups (iii) and (iv) can be found in the appendix.

The gas supply for all experimental set-ups mentioned here is regulated by three mass flow controllers (MFC, Bronkhorst). Depending on the planned experiment it is possible to switch between two to four different gases or gas mixtures. This results in MFC-1 controlling Ar or He, MFC-2 controlling O_2 or synthetic air and MFC-3 controlling the flow of CO, CO_2 or two more gases which can be potentially attached to the pre-routed gas lines. Figure 17 shows a schematic

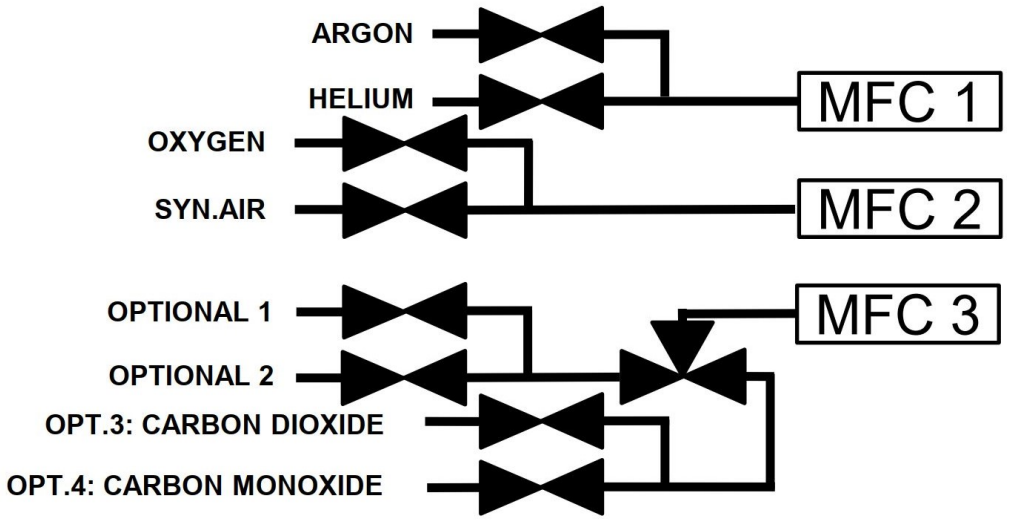

Figure 17: schematic depiction of the installed gas lines leading to the main controlling unit of three MFCs.

depiction of the gas line set-up and gas supply station. While MFC-1 and MFC-2 are Bronkhorst basic *FLOW* edition controllers and calibrated for only one specific gas (or gases with similar properties) at 273 K and a pressure of $1.013 \cdot 10^5$ Pa, MFC-3 is a *Prestige* unit, which allows to adjust the settings like inlet gas, inlet pressure and operating temperature as well as outlet pressure. The pressure was set for all gases to 4 bar inlet and adjusted to 1 bar outlet. The analysis of the effluent gas stream is performed with a quadrupole mass spectrometer (QMS; IP Instruments).

3.1.2 Illumination sorce

Further the utilization of a *LUMATEC Superlite S04* lamp with flexible light conductor allowed measurements under illumination. It features a light source and a set of different light filters allowing illumination with only a certain radiation range. For the experiments in this work two settings were used: UV light ranging 320-400 nm and an intensity of 135 mW/cm^2 as well as a visible light ranging from 400-700 nm and an intensity of 225 mW/cm^2. Figure 18 shows a picture of the lamp as well as the spectral properties of the illumination at utilized lamp settings.

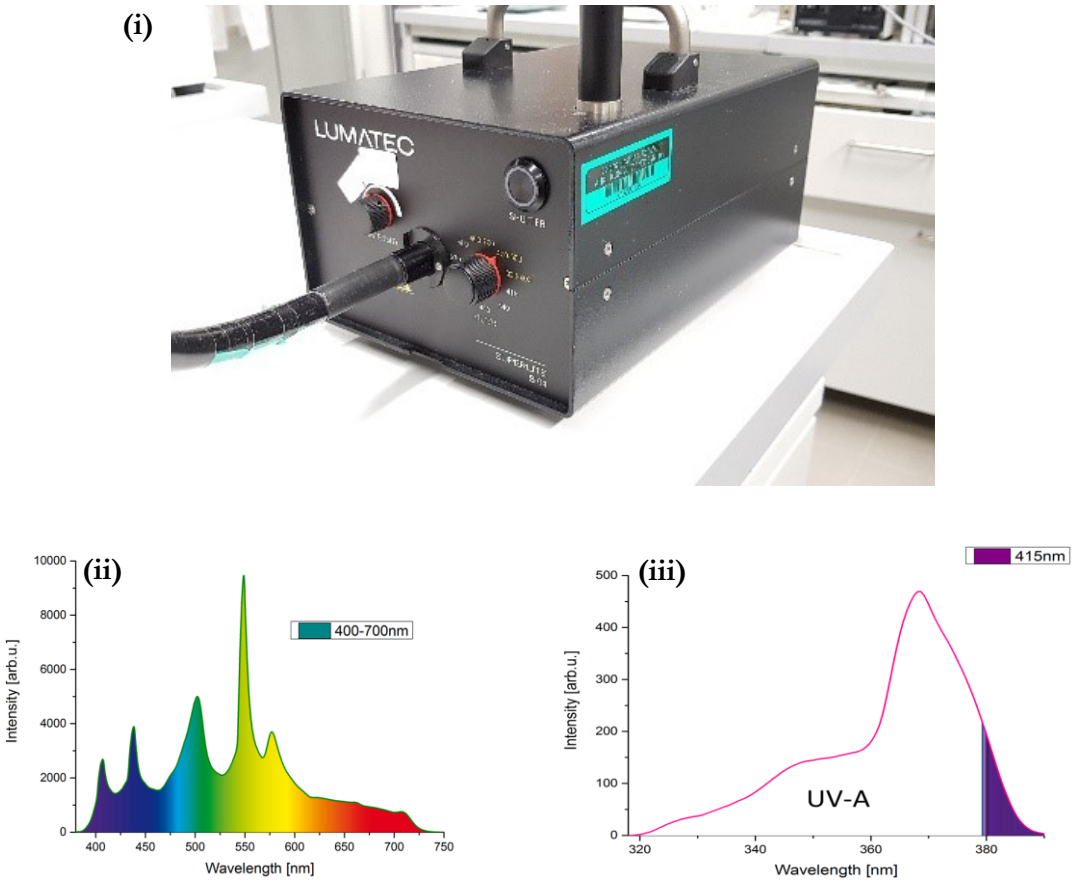

Figure 18: (i) LUMATEC Superlite S04 lamp utilized for the illumination of the sample during CO_2 adsorption and other experiments; (ii), (iii) spectral properties of the light source at the selected device settings.

3.1.3 In-situ DRIFTS set-up

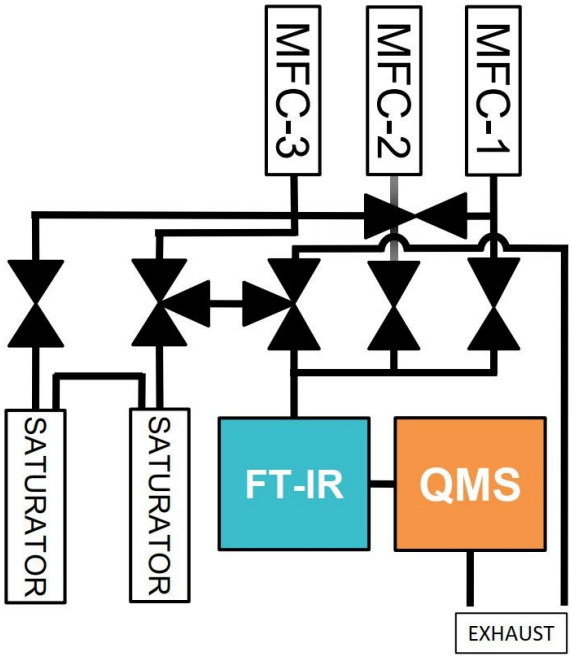

Figure 19: Schematic depiction of the FT-IR set-up including MFC controlling the gas flow, water saturators, FT-IR device and QMS

The main two devices implemented in this set-up were the FT-IR spectrometer and the quadrupole mass spectrometer mentioned in prior chapters. A schematic depiction is shown in Figure 19. DRIFTS measurements were performed by utilization of the *in situ* high temperature reaction chamber supplied by Harrick shown in Figure 20. It features a stainless-steel sample holder and hemispherical stainless-steel dome with metal circular rim and three windows of which two are made of KBr and one of SiO_2. KBr windows allow transmission of the IR beam without significant absorbance in the mid IR region and thus recording of DRIFT spectra in the spectral range 4000-400 cm^{-1}. The SiO_2 window allows illumination of the sample with light of different wavelengths, while being transparent to UV radiation. On the whole perimeter of the bottom side of the rim a notch is engraved, which offers space for a Viton O-ring. The dome is positioned on top of the cell and secured with a metal plate on each side. When screwing down the four screws of the metal plates, the Viton O-ring is squeezed resulting in an airtight sealing of the reaction chamber. Depending on the orientation of the set-up (e.g. pipeline limitations) one of two connectors positioned on each corner of the front side of the cell can be utilized as gas inlet. The gas flow is directed into the chamber entering below the sample holder on its right (or left, depending on which connector is being utilized). The powdered sample is prefilled in the sample holder in the middle of the chamber. The sample holder features a hole at the bottom which is

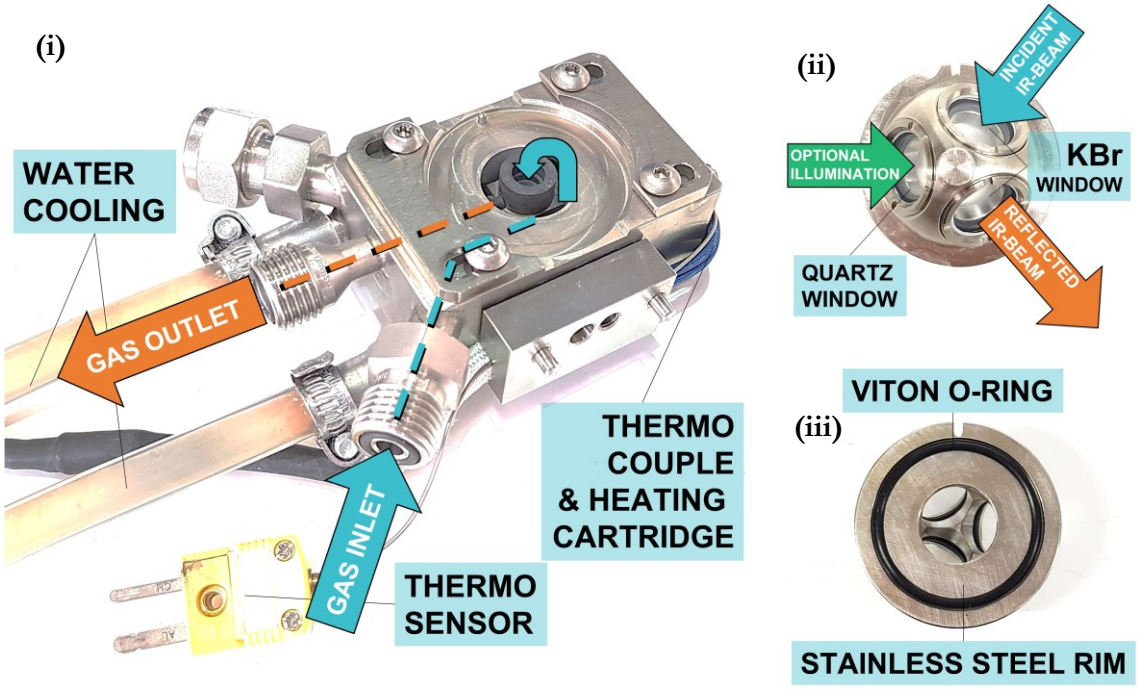

Figure 20: (i) Harrick in-situ high temperature cell, (ii) top view and (iii) bottom view on hemispherical stainless-steel dome with three windows.

covered by a fine mesh (100 µm pore size) and is the only exit in the chosen orientation of the chamber. By this the chamber is filled with gas from the bottom and allows the gas to exit the cell only when passing through the sample. It is possible to utilize the middle connector as gas inlet, however, rapid changes in gas flow and bursts of gas may cause spreading of the powdered sample inside the chamber and thus aborting the measurement. The bottom part of the cell features a separate channel allowing to cool the entire cell with a fluid e.g., water. Moreover, the sample holder can be heated by the built-in cartridges regulated by a Harrick ACT/low voltage heating control element based on the Watlow EZ-ZONE© dual channel controller. It was attached to a PC through an RS-485 to USB 2.0 adapter allowing to control the temperature and implement different temperature programs via the desktop application Watlow EZ-ZONE© Configurator.

The FT-IR spectrometer utilized in this work was expanded with a Praying Mantis™ mirror array which was supplied by Harrick and is required for DRIFT measurements utilizing the Harrick in situ high temperature reaction chamber.

Figure 21 shows a photograph and a schematic depiction of the Paying Mantis™ DRIFTS accessory as well as a schematic of the IR beam path.

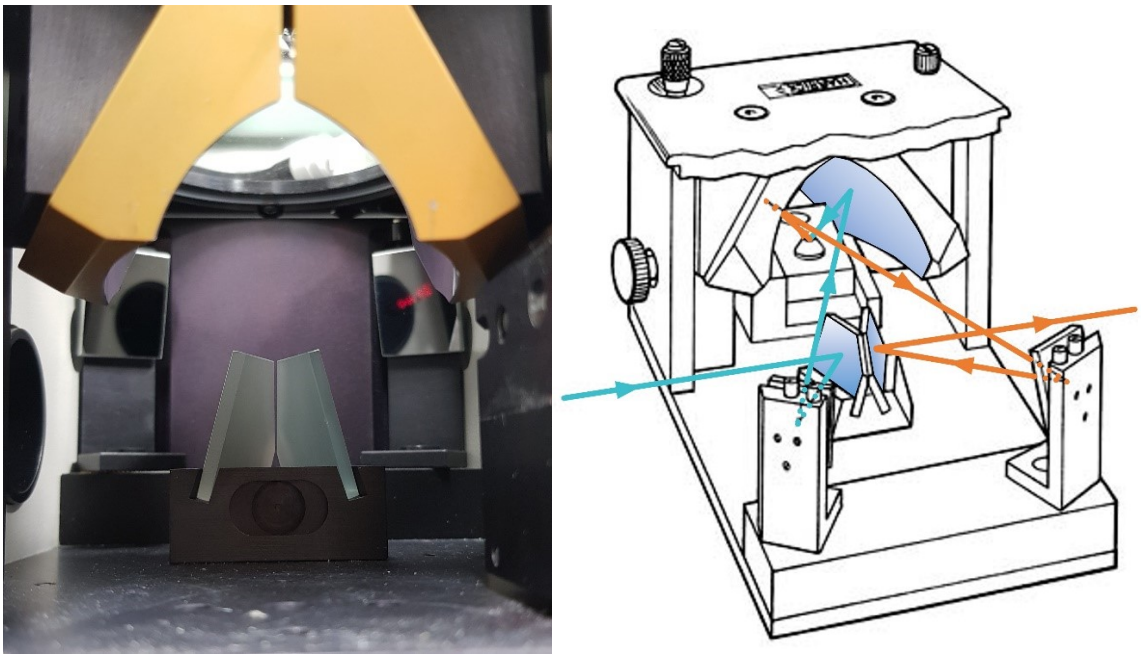

Figure 21: Praying Mantis Mirror geometry utilized for measurements of DRIFT spectra: (left) photograph, front view; (right) schematic depiction, back view (modified from Ref. [127]) Blue: incident IR beam, orange: cumulated diffuse reflected IR beam after having contact with the sample and carrying information to the detector.

3.1.4 Photo TPD set-up

The main part of the set-up was a custom-made heating chamber to perform temperature programmed experiments in flow mode while optional illumination. The chamber consists of a stainless-steel box with circular cutouts on opposite sides. A simple air-cooling device was constructed by channeling an air flow of two 120 mm pc-fans through 50 mm thick, flexible, stainless-steel pipe and through the heating chamber. Inside the chamber a solid copper block is situated, which can be heated by two heating cartridges and is shown in Figure 22 (i). The heating rate and temperature is being controlled by a custom temperature regulator designed by MPI CEC Electronics department around an JUMO© iTRON32 regulation module. A custom-made quartz sample holder can be placed inside of the copper heating block. The sample holder is hand made from quartz tubes of different diameter and is shown in Figure 22 (ii). It features quartz tubes with an inner diameter of 9 mm on both ends as well as a 15 mm tube in the middle, which was squeezed to a height of ~9 mm. By this the middle part features a close-to-flat surface on which solid powdered samples can be spread out evenly offering several advantages for illuminated measurements with solid gas reaction systems. The amount of material below the surface layer is considerably lower compared to non-squeezed tubing, thus maximizing the amount of the sample exposed to the gas flow as well as to illumination. Further, on one side the sample holder has three small flow breakers, which ensure perturbation of an incoming laminar gas flow. This favors

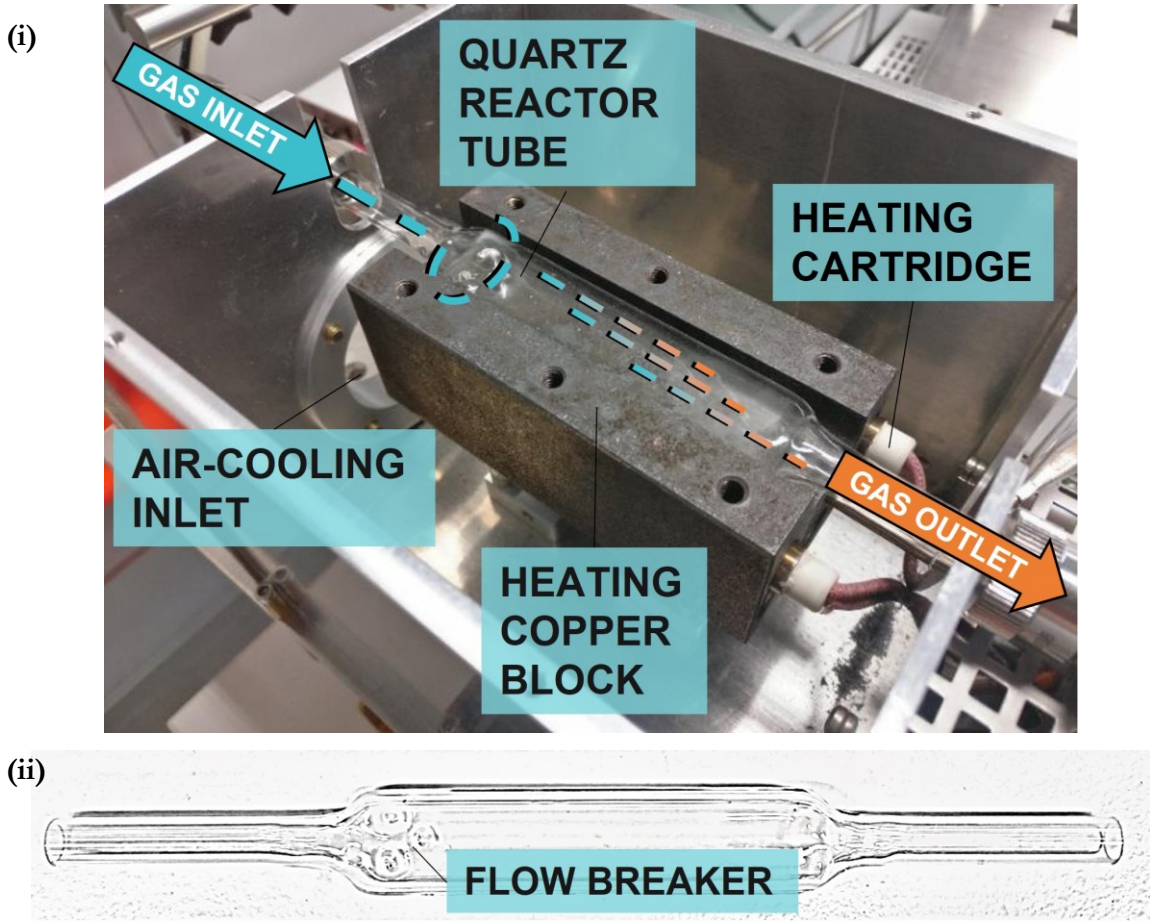

Figure 22: (i) Copper heating block inside the stainless-steel box; (ii) quartz sample holder

interaction of the gas with the sample due to higher residence time of the gas inside the tube, but also reduces the risk of sudden bursts in gas flow perturbating the evenly spread sample. The heating chamber can be closed with a stainless-steel plate, which features a small rectangular cut out positioned directly above the flattened part of the sample holder. Thus, heat of the copper block is isolated from the surrounding environment while also allowing the implementation of different irradiation devices for photo-assisted temperature programmed experiments.

To assure proper cooling of the reaction chamber during the cooling steps a funnel-like part was designed in 3D modelling software and printed by a 3D printer (s. Figure 23). It allows mounting of two standard 120 mm PC fans on one side, as well as a 50 mm pipe on the other side. The channeling effect of the funnel-like structure allows good airflow at low noise levels.

The main purpose of this set-up is to investigate adsorption, desorption events in an flow optimized cell. Additionally, the sample is evenly spread featuring a very thin sample thickness thus maximizing the sample area interacting with gas flow. Further, the illuminated fraction of the sample is maximized as well. Consequently, a sophisticated set-up was adopted in laboratory facilities offering the possibility of temperature programmed, but also illuminated experiments.

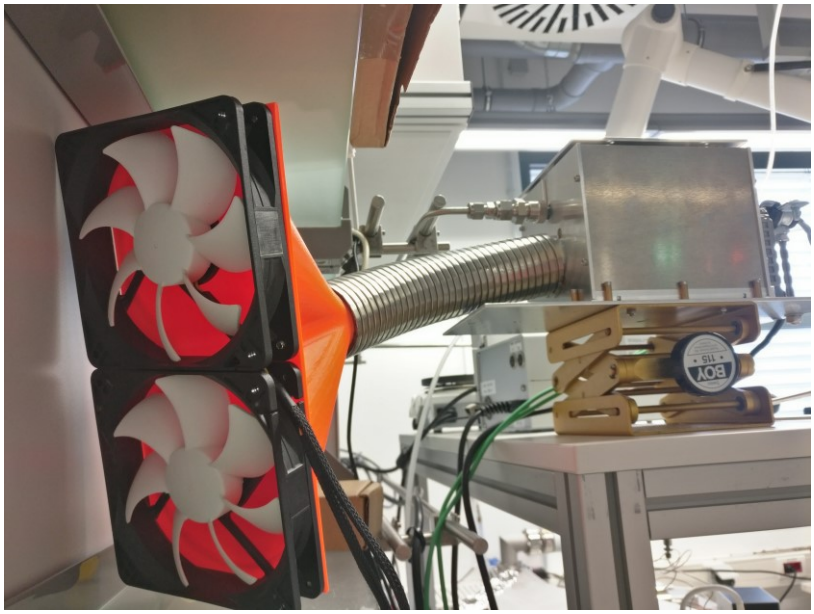

Figure 23: Air cooling of the Photo TPD set-up by two 120 mm PC fans mounted to a 3D-Printed double funnel(orange) channeling air into a flexible 50 mm steel pipe.

3.2 Experimental procedure

The set-ups for Photo TPD and DRIFTS measurements allowed in-situ measurements of powdered samples with flow through mode and different gas streams, as well as elevated temperatures.

The experimental procedure was the same and consisted of three main parts: (i) pre-treatment, (ii) CO_2 adsorption and (iii) post-treatment. A schematic depiction of the experimental procedure can be found in Figure 24. After introduction of the sample, the reaction chamber was purged with Ar for 1-2 h to remove all residual air. According to previous studies[128-130] each sample was heated in a steady Ar flow to 725 K with a heating rate of 10 K/min and held for 1 h. This thermal treatment procedure was found to be the best combination between sample surface cleaning and time efficiency. The sample was allowed to cool down to RT (assisted by water or air cooling depending on the set-up used) prior to conducting the CO_2 adsorption. In the second part 10 % CO_2 was added to the gas stream for 30 min and purged subsequently with Ar for 1-2 h to remove residual atmospheric CO_2. In the third part a thermal treatment similar to the pre-treatment procedure was applied resulting in a temperature programmed desorption experiment of the adsorbed CO_2. A permanent flow of 30 ml/min was set for most measurements while Ar was chosen as carrier gas. The effluent gas stream was analyzed by the QMS which was calibrated for the quantitative detection of CO_2, CO, H_2, N_2, H_2O, CH_3OH and CH_4. A calibration matrix was utilized, which automatically calculated the mole fractions of the effluent gas stream from recorded

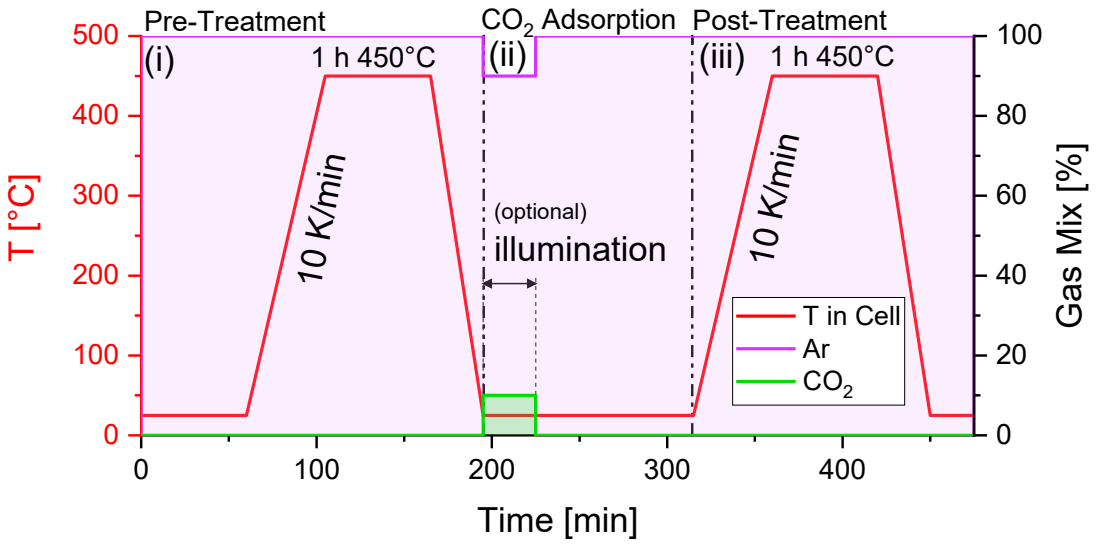

Figure 24: Schematic depiction of the experimental procedure.

values of ion currents of all relevant m/z signals. The time resolution equaled 7 s/cycle. However, due to implementation of mostly ¼" stainless steel pipes, the overall volume of the gas lines connecting the MFCs and the QMS is about 65 ml which resulted in a delay of about 2 min between input of instructions for gas changes in the software and detection at the QMS.

During each measurement part a series of spectra was recorded utilizing the FT-IR spectrometer mentioned earlier. All spectra were recorded in the spectral range from 4000-400 cm^{-1} with a resolution of 4 cm^{-1} and averaging 200 scans resulting in one spectrum every 1.3 min. All changes in the reaction system e.g., changing of temperature or gas composition, addition of light etc. were implemented after recording at least one spectrum. With this a baseline-spectrum was available for post-processing of the recorded series of spectra and creation of subtraction spectra which offer a better visibility of changes in the spectra (especially when the investigated sample shows a versatile IR-spectrum itself).

3.3 Synthesis of ZnO materials

ZnO rods and flowers were prepared following the synthesis procedure described by Cao *et al.*[50] An aqueous NaOH solution was slowly added to an aqueous solution of $Zn(NO_3)_2$ at room temperature while thorough stirring. While the molar ratio of the Zn to hydroxide is set to be 1:10, the overall concentration of both decides on the resulting shape. Mixing a 0.01 M solution of $Zn(NO_3)_2$ with a 0.1 M solution of NaOH leads to a formation of flakes. When the concentrations

are increased by a tenfold, the ZnO particles are expected to feature a nanorod-like shape. The combined solution is stirred for further 30 min at room temperature before being heated to 95 °C while stirred. Afterwards the white solid was filtered and dried at 60 °C overnight.

Further a ZnO sample was synthesized following a simple solid-state procedure. Zinc acetate precursor was heated in a beaker to 1100 °C at atmospheric pressure in air.

3.4 Characterization of ZnO Nanostructures

An in-depth view on the theoretical and practical background of characterization methods utilized in this work is given in chapter 7.1.

For the investigations of nanostructured ZnO commercial ZnO particles with a size of 20 nm were selected as a benchmark material. Four other ZnO samples with unique nanostructures have been synthesized following the synthesis route described in the previous chapter. In total five samples have been investigated which are denoted as "particles" (commercial ZnO particles, mean size 20 nm, iolitec), "flakes" (nano flakes), "flowers" (nanoflowers), "rods" (nanorods), "SSS" (solid-state synthesis).

All samples have been investigated by means of XRD to ensure the presence of crystalline ZnO and SEM to verify a successful synthesis of the desired nanostructures. Figure 25 shows the XRD

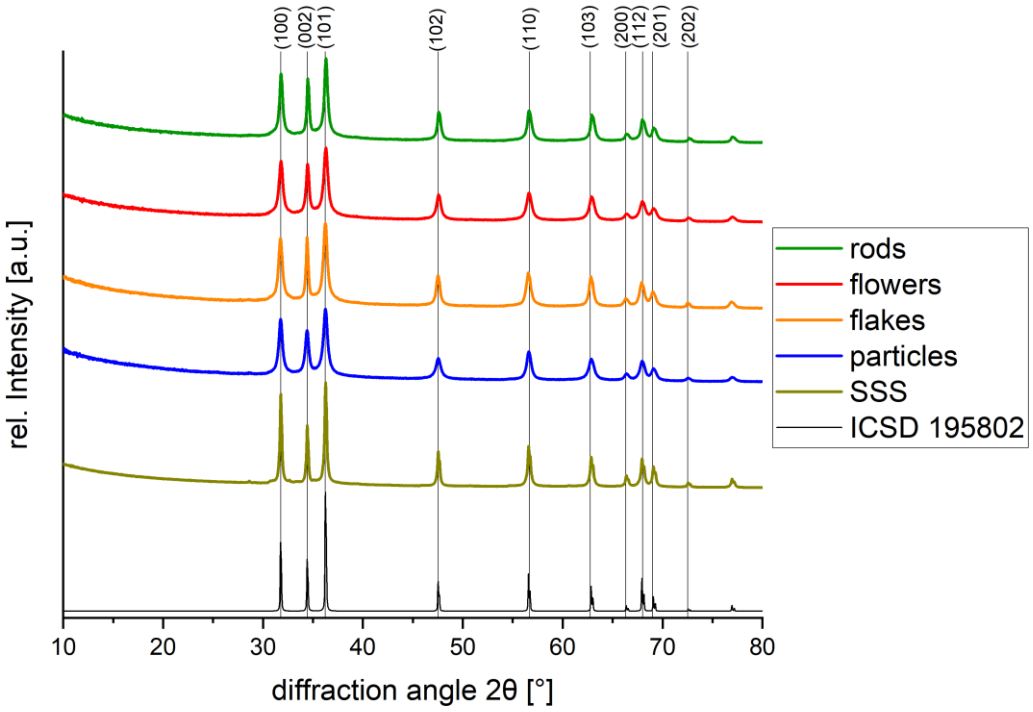

Figure 25: XRD patterns of ZnO samples synthesized during the course of this work as well as reference pattern NIST.

patterns of all samples as well as of the reference ZnO material with wurzite crystalline structure (NIST: ICSD 195802). All samples feature sharp reflexes matching the reference material data confirming the successful synthesis of ZnO materials with highly crystalline wurtzite structure. However, while the reference shows (100) and (002) reflexes being of nearly equal height and much smaller than that of (101) reflex, the difference between the intensity of these three reflexes is smaller in all self-made materials. While the SSS sample shows a less pronounced (002) reflex, all other samples feature an equal intensity of (100) and (002) reflexes as well as a (101) reflex, which is insignificantly higher. In general, the reflexes of the SSS material are sharper than the reflexes of all the other materials. This may be due to the large, well-defined, and prolonged primary crystal structure of the SSS sample, as can be seen in Figure 26 (v). Due to the same reason, the diffractogram of the particles features the broadest reflexes; the primary crystallite structure is constrained to much smaller size of about 20 nm. SEM images of all samples are shown in Figure 26, where images (i) – (iv) are recorded with a magnification of 25 000. As the SSS sample features a much larger particle size a magnification of 1000 was required for a proper image. Rods and Flowers shown in Figure 26 (ii) and (iii) respectively, were synthesized according to synthesis routes described earlier and elsewhere[50]. The synthesis of flowers resulted in ZnO nanosheets with a thickness of about 30 nm and densely stacked to a flowerlike structure, which was also easily reproducible. On the other hand, the synthesis of rods succeeded only once and resulted in rods of about 40 nm thickness and 300 nm length. After numerous attempts by the author as well as colleagues, the synthesis resulted in material denoted as flakes (Figure 26 (iv)). While it is a result of a nanorod synthesis procedure, it has the appearance close to the nanoflower sample, but with a less dense alignment of flakes. Since it featured interesting behavior in FT-IR measurements (different to rods or flowers) and was easily reproducible through the nanorod synthesis route, it was included into the set of investigated samples. Further diffuse reflectance UV/Vis Spectroscopy (DRS) was utilized to measure the reflectance of the samples. According to the method explained in detail Apendix (Chapter 7.1.3.1)., the band gap was determined graphically utilizing the results obtained from DRS measurements. The respective graphs are shown in Figure 27. All samples except SSS ZnO feature band gap values between 3.22 and 3.28 eV, while SSS ZnO has a calculated band gap of 3.16 eV. With that, all ZnO samples feature a band gap well below the value of (3.37+/-0.01) eV reported in literature.[22] Determination of the specific surface area was performed according to Nitrogen physisorption measurements described in detail in Chapter 7.1.2. Table 3 summarizes the results of estimated band gaps and specific surface area values for all samples. Measurements of the specific surface area resulted in values between 5 and 50 m^2g^{-1}. Unfortunately, despite several measurements of the specific surface area of ZnO SSS material no reasonable values

were obtained. This might be due to its large crystals with well-defined, near perfect, mostly defect fee surfaces, which overall feature a surface area well below the detection limit of the measurement device. Nanoparticles have the most versatile distribution of surfaces as well as a theoretically high surface to volume ratio (from the geometrical perspective), which might be the reason for the largest value of specific surface area. While flakes and flowers both originate from sheets of ZnO, flakes have a larger surface area than flowers. Even though in flowers more sheets seem to be stacked in a certain volume the higher stacking density may result in more sterically hindered areas

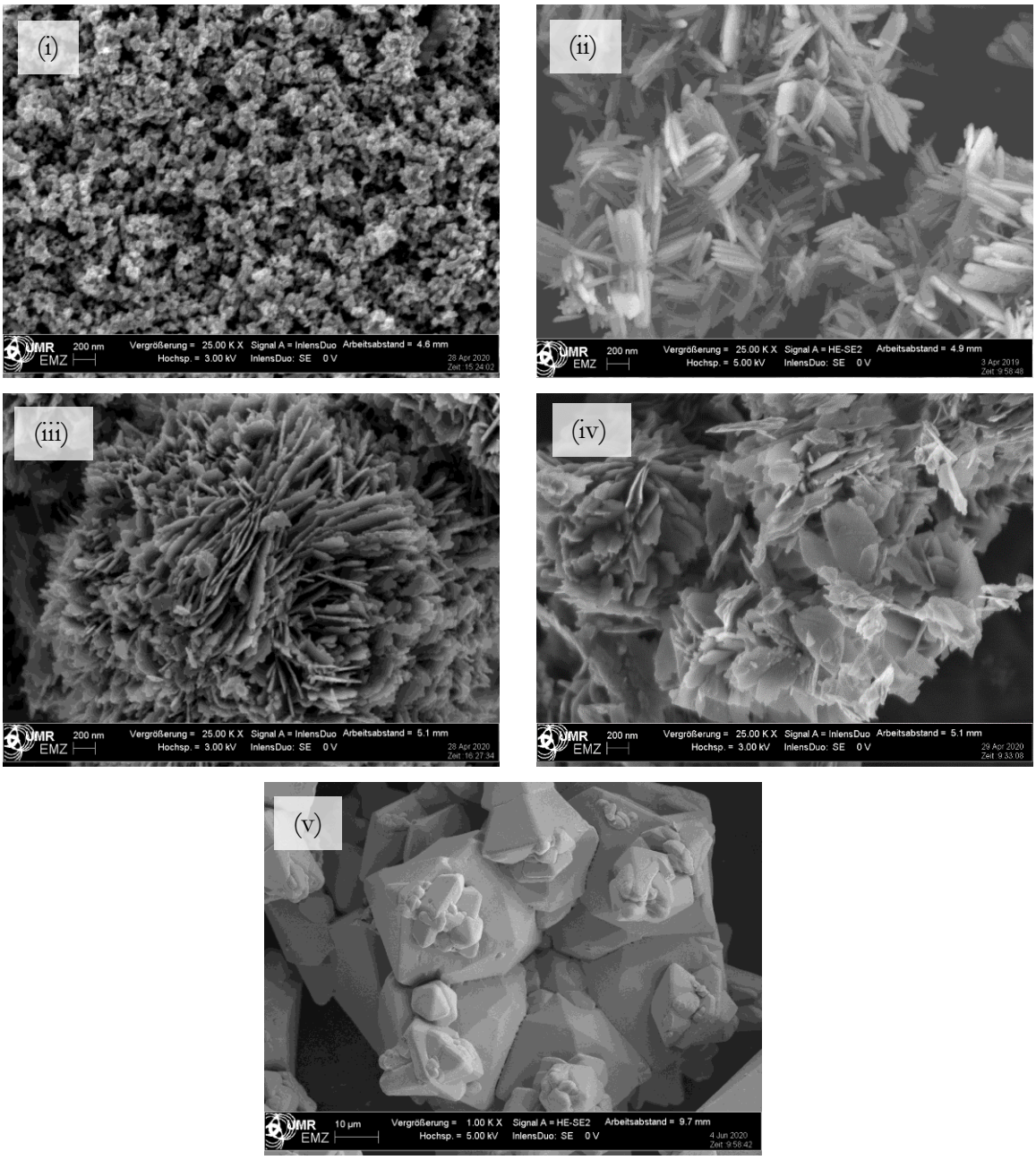

Figure 26: SEM images of all ZnO samples investigated in the work at hand: (i) particles (top left), (ii) rods (top right), (iii) flowers (middle left), (iv) flakes (middle right), (v) SSS (bottom). Images (i) to (iv) were recorded at a magnification of 25 000 and 3 kV; image (v) at a magnification of 1 000 and 5 kV.

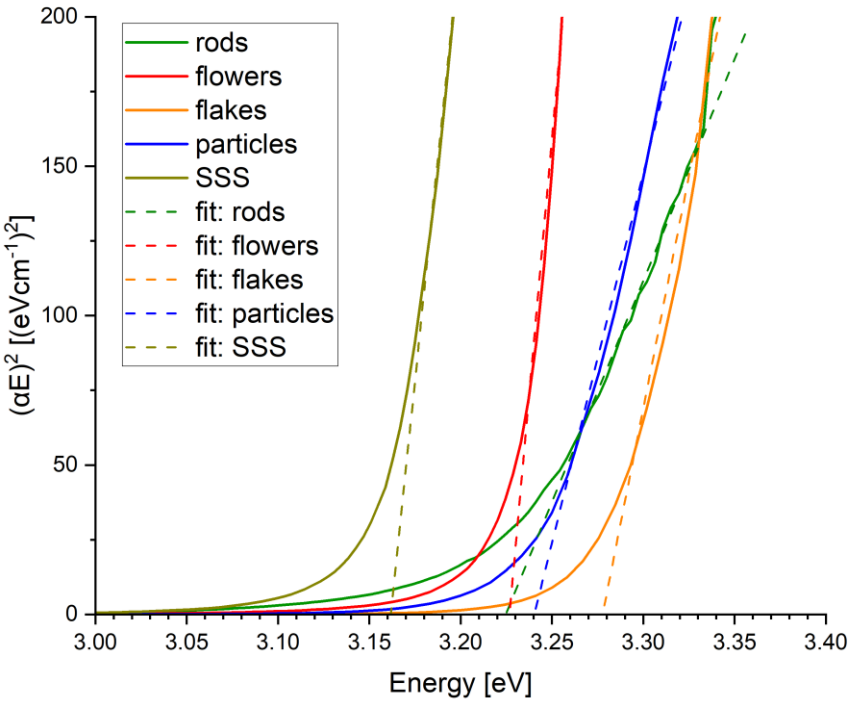

Figure 27: Graphical determination of the band gap values from measured DR-UV/Vis-spectra of all ZnO materials.

for N_2 molecules to reach. When granted more space around each sheet (as in flakes), those hindered spots are possibly more easily accessible and resulting in adsorption of more nitrogen. Rods feature the lowest surface area with only 4.8 m^2g^{-1}. This is possibly due to large surfaces on the long sides of the crystals, which are either connecting the rods between each other or otherwise do not offer proper adsorption area. Therefore, the only adsorption surfaces are the tips of the rods. One can compare the rods to particles, which have been extended in a certain direction and thus featuring a much lower (active) surface to volume ratio. This results in large crystals but low overall nitrogen adsorption per gram of catalyst. Figure 28 shows initial DRIFT spectra for all five materials recorded prior to thermal pretreatment and CO_2 adsorption. All spectra feature an

Table 3: Summary of synthesized nanostructured samples.

sample	band gap [eV]	S_{BET} [m^2g^{-1}]
particles	3.24	48.7
flakes	3.28	28.2
flowers	3.23	19.6
rods	3.22	4.8
SSS	3.16	n.a.

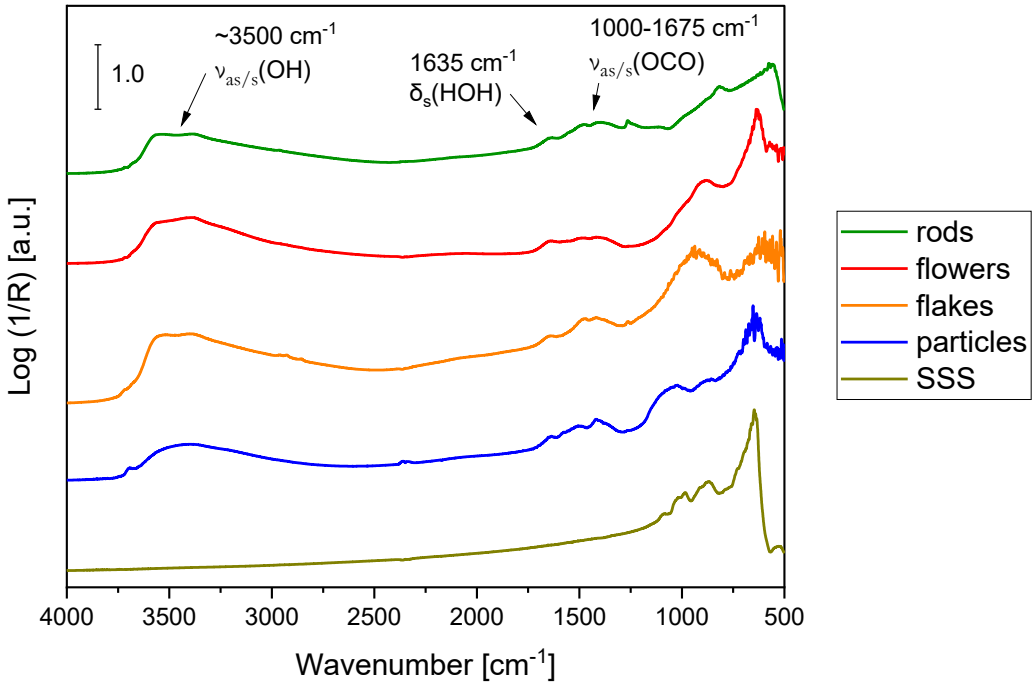

Figure 28: DRIFT Spectra of all as synthesized ZnO nanomaterials as well as commercial ZnO particles.

increase of the intensity towards lower wavenumbers. This is a characteristic behavior for ZnO and metal oxide materials in general, as metal oxygen bond vibrations are observed in this region. Raman Spectroscopy is mostly utilized in order to investigate lattice vibrations of metal oxide semiconductor materials, which is not part of this work. Further, a broad signal arises around 3500 cm^{-1}, which is due to symmetric and antisymmetric vibrational stretching of hydroxyl groups ($\nu_{as/s}$(HOH)) of physisorbed molecular water. Additionally scissoring deformation vibration of adsorbed molecular water molecules (δ_s(HOH)) result in a weak feature at 1635 cm^{-1}. Around 1500 cm^{-1} another broad set of signals is apparent and can be assigned to different vibrational modes originating from carbonate species formed due to adsorption of atmospheric CO_2 and its interaction with surface oxygen as well as surface hydroxyl groups. Due to the broad character of the features in this region an assignment of signals to more specific vibrational modes and thus identification of carbonate and bicarbonate species is not reasonable. Nevertheless, all samples but SSS-ZnO show good adsorption capabilities in respect to water and CO_2. This might be due to the low surface area of the SSS material, but also due to the harsh synthesis temperatures of over 1000 °C which may passivate the sample in regard to adsorption capabilities.

Table 4: Band positions of adsorbed hydroxyl groups on ZnO surface

Surface plane	Band position [cm^{-1}]	description
O-ZnO ($000\bar{1}$) Polar	3620	dissociative adsorption of water on O-vacancies
ZnO ($10\bar{1}0$) Mixed terminated	3687	Chemisorbed water
	3672	Interacting with co-adsorbed water
	3639	Isolated
Not a single crystal surface	3564 3448	Defect-related

3.5 Surface plane determination via Hydroxyl group analysis by means of DRIFTS

Prior to adsorption of CO_2 a thermal pretreatment was included as part of the experiment, in order to clean the surface from pre-adsorbed residual organic molecules such as water and carbonates. DRIFT spectra were recorded throughout the course of the whole experiment, which gave also the possibility to monitor the changes in the features characteristic for hydroxyl groups. With work of Noei *et al.* at hand[131,132] it was attempted to determine exposed surfaces mostly present on different ZnO materials. In Table 4 wavenumbers of features in the IR spectrum characteristic for hydroxyl groups on ZnO surface are summarized.

Figure 29 shows the IR spectra for all samples recorded during the thermal pretreatment in Argon. All material but (v) SSS show a general decrease of the broad band ranging from 3800 to 2600 cm^{-1}, which is characteristic for interaction between molecules of physisorbed water on the surface. Therefore, with increased temperature the amount of adsorbed molecular water decreases. The SSS ZnO sample does not feature any apparent bands except overtones of gas phase water, which can be seen between 3800 and 3550 cm^{-1}. These, however, are a result of high magnification of the spectra, as well as a slightly higher amount of gas phase water in the reaction chamber during recording of background spectra compared to recording of pretreatment procedure of the sample on that certain day. Consequently, stronger bands are being subtracted resulting in negative bands. Moreover, the results of the FTIR-measurement of the SSS sample imply that no adsorption is taking place. This will also be confirmed by CO_2 adsorption experiment later. As was already shown in Figure 26 (v), the SSS sample features large, unified crystal surfaces, which might have little to no defective sites, or any other sites featuring good adsorption properties resulting in overall bad

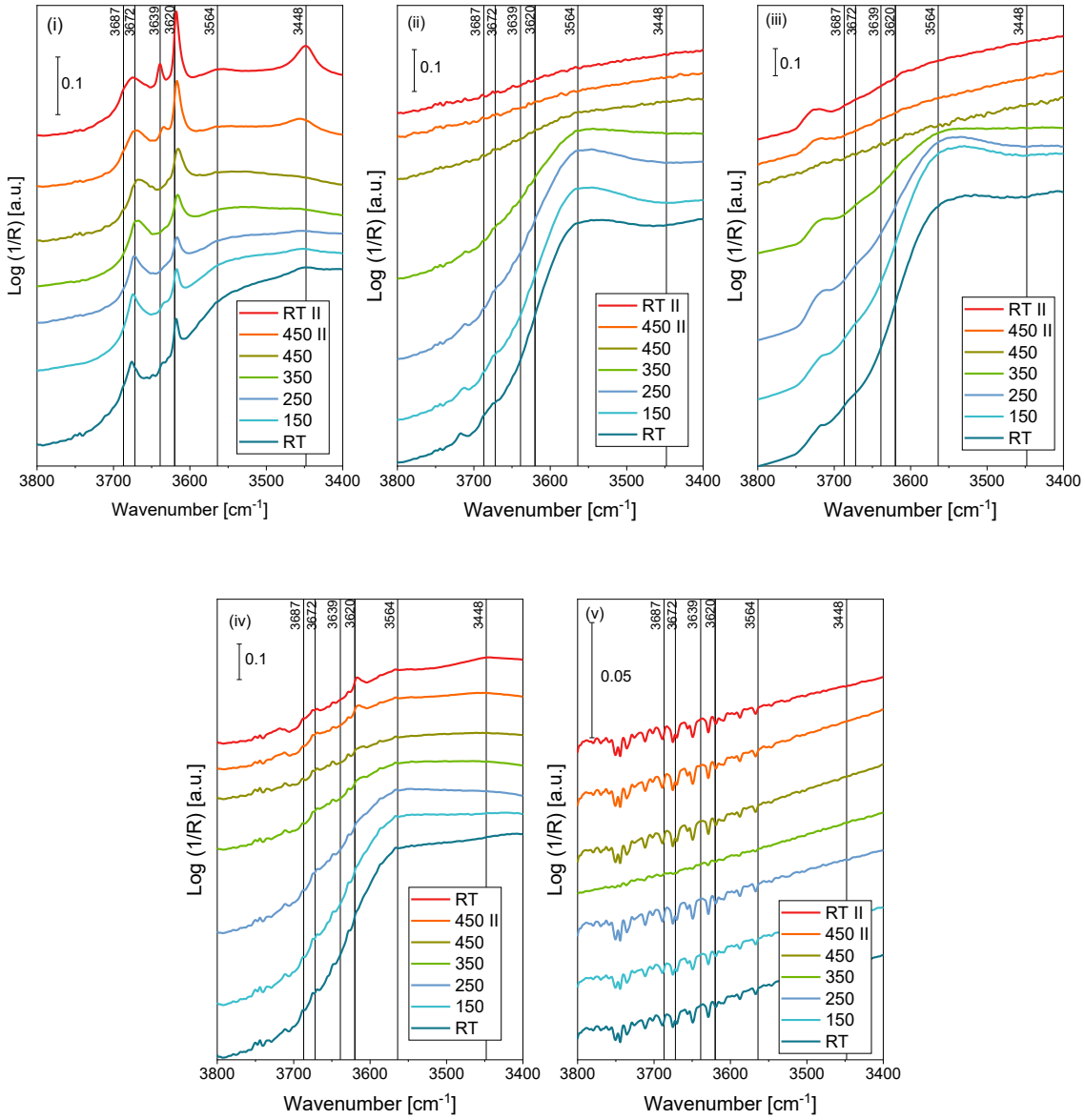

Figure 29: DRIFT spectra of as synthesized samples recorded during thermal treatment in Ar flow: (i) particles (top left), (ii) rods (top middle), (iii) flakes (top right), (iv) flowers (bottom left), (v) SSS (bottom right). The range was cut down for better determination of hydroxide groups for characterization of exposed surfaces present on the material.

adsorption properties of the SSS material. The spectra of rods and flakes sample shown in Figure 29 (ii) and (iii) respective, feature only physisorbed water, with no further bands which can be unambiguously assigned to any hydroxyl surface species. The spectrum of ZnO nanoflower features a weak signal at 3620 cm^{-1} which becomes more apparent, as soon as the sample is heated to 450°C and cooled down to room temperature again. This band is characteristic for dissociative adsorption of water on oxygen vacancies on the polar oxygen terminated $(000\bar{1})$. Masking of the band on the initial sample might result from high coverage of the surface with physisorbed molecular water or dissociation of adsorbed water on oxygen vacancies due to high temperature.

Further weak bands can be found at 3687 and 3672 cm^{-1} indicating the presence of chemisorbed water as well as interaction of hydroxyl groups with co-adsorbed water, respectively, on the $(10\bar{1}0)$ mixed terminated surface. The spectra of ZnO particles sample (Figure 29 (i)) feature several strong bands. In general, the broad band characteristic for physisorbed water is very broad, which might be due to a presence of large amount of different adsorption sites, thus resulting in broad range of interactions of the molecular water with the surface. The main band at 3620, and a combined band of 3672 and 3687 cm^{-1} are apparent also at low temperature prior to thermal treatment indicating the increased presence of $(000\bar{1})$ and $(10\bar{1}0)$ exposed surfaces. By removal of large portion of the physisorbed water two more bands arise at 3639 and 3448 cm^{-1} as well as a weak band at 3564 cm^{-1}. The latter two are characteristic for adsorbed hydroxyl groups on non-perfect crystal planes and thus defect related. The band at 3639 cm^{-1}, however, is characteristic for isolated hydroxyl groups on $(10\bar{1}0)$ mixed terminated surface. Therefore, ZnO particles feature basically all kinds of crystal surfaces as well as a large number of defect sites. As the structure of ball-shaped particles mainly consists of steps and kinks, and less of large unified perfect crystal surfaces these results are in agreement with the theory. The influence of atmosphere for the pretreatment procedure was investigated for two out of five samples – particles and rods. Figure 30 shows the comparison between thermal treatment of particles in Ar only and 15% O_2 in Ar. It can be seen that the pretreatment has a similar effect on the hydroxyl species featuring bands at 3620, 3687 and 3672 cm^{-1}. While in Figure 30 (ii) less hydroxyl species interacting with co-adsorbed water at $(10\bar{1}0)$ crystal planes seem to be present in the beginning of the measurement (indicated by the bands

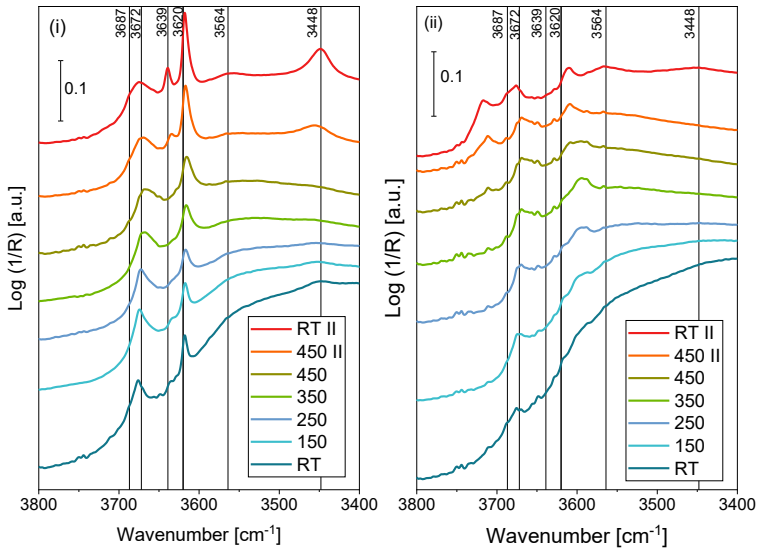

Figure 30: comparison of behavior of hydroxyl groups during thermal pretreatment of commercial particles in (i) Ar or (ii) 15% O_2 atmosphere.

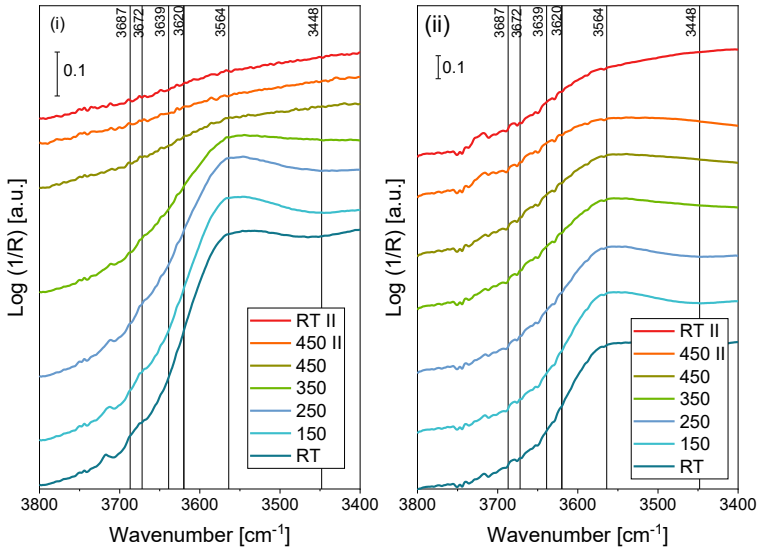

Figure 31: Comparison of behavior of hydroxyl groups during thermal pretreatment of as synthesized rods in (i) Ar or (ii) 15% O_2atmosphere.

3687 at 3620 cm^{-1}), after the treatment the according bands are much more apparent in both cases. Further no feature at 3639 cm^{-1} as well as much weaker bands at 3448 and 3564 cm^{-1} can be seen after the thermal treatment in oxygen rich atmosphere. While latter two result from less defective sites present after the treatment, possibly due to filling of oxygen defect sites with oxygen from the atmosphere, the missing band at 3639 cm^{-1} indicated no isolated hydroxyl groups on the mixed terminated $(10\bar{1}0)$ plane. As these species appear only at the end of the treatment in Ar atmosphere, the corresponding adsorption sites allowing the formation of those, are not being formed during the treatment in oxygen rich atmosphere, possibly due to filling with oxygen instead.

In Figure 31 DRIFT spectra of the thermal pretreatment of rods in pure Argon compared to in 15% O_2 in Argon can be found. Except the decrease of the physisorbed molecular water due to the drying of the sample, no further features can be seen in both spectra. This indicates on one hand water adsorption capability of the sample, on the other hand, however, no active sites for dissociative water adsorption resulting in no apparent features of adsorbed hydroxyl groups in DRIFT spectra.

Unfortunately, hydroxyl group analysis provided in cases of some materials results of limited quality which made it difficult to unambiguously determine certain surface planes every material.

3.6 Influence of light and heat on DRIFT spectra

For the investigation of carbonate species being formed on the surface of ZnO materials due to exposure of CO_2 from air or during the adsorption experiment, observation of changes in the

spectral region from 1800 to 1000 cm^{-1} was attempted. In the IR spectrum most carbonate species adsorbed on semiconductor surfaces feature signals in this region as was shown earlier (Chapter 2.3). Series of spectra were recorded during pretreatment procedure as well as during the CO_2 adsorption experiment for this instance. To obtain a general overview over the experiment results all spectra of a series were plotted along a third time dependent axis creating 3D spectra. OMNIC 7 Software provided by Thermo Scientific was utilized for this purpose. Additionally, a color gradient ranging from deep blue to bright red was added to the spectra for a better visibility of changes in the spectrum. Interestingly, ZnO samples showed baseline shifting and bending in the DRIFT spectra upon heating in inert atmospheres (Ar, He) and reasonable efforts were undertaken to investigate the origin of such phenomena. To exclude temperature gradient interference as the origin of this behavior, experiments with heating rates of 1, 2, 5 and 10 $Kmin^{-1}$ were conducted on commercial ZnO particles ensuring temperature equilibration from the heated sample holder walls into the SSS material, while also determining appropriate heating rate for a time efficient measurement procedure. Figure 32 shows 3D depiction of the series spectra recorded during the pretreatment procedure with different heating rates. Except the heating duration no difference can be found among the four shown spectra. Upon heating the intensity of the baseline increases, until a maximum is reached at a temperature of about 525 K. Afterwards, the baseline drops to a level slightly below the initial level and remains unchanged, when temperature was kept constant at 725 K. As soon as the sample was cooled down to room temperature, the intensity of

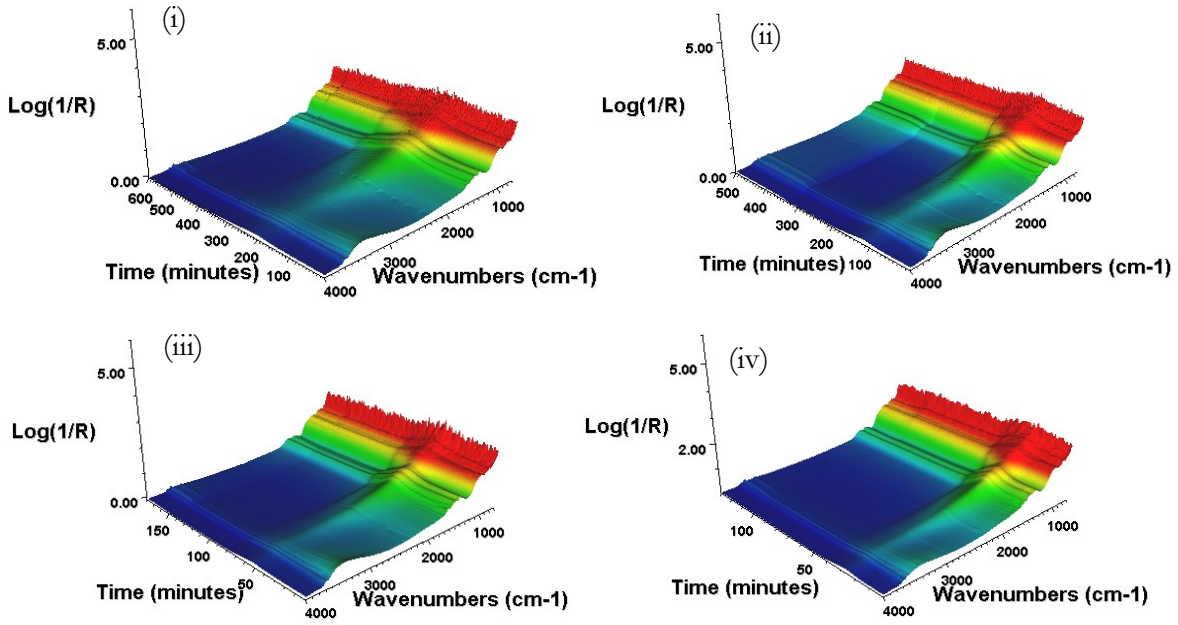

Figure 32: Comparison of 3D spectra of ZnO particles recorded during thermal pretreatment with heating rates of (i) 1 $Kmin^{-1}$, (ii) 2 $Kmin^{-1}$, (iii) 5 $Kmin^{-1}$ and (iv) 10 $Kmin^{-1}$ in 30 ml/min Ar flow. Target temperature of 450 °C was reached at (i) 425 min , (ii) 210 min, (iii) 85 min, (iv) 45 min followed by holding the sample for 1h at 450 °C and cooling down to room temperature.

the baseline reached the initial value. Since the baseline shift appeared regardless of the heating rate, its influence was excluded. A change within the electronic structure of the sample which leads to changes of the optical properties was proposed as the origin of these phenomena. An in-depth literature search in physical and physico-chemical publications from the mid-20th century covered in Chapter 2.5 gave an answer to this question. ZnO is well known to change its optical properties due to heating, which also leads to the observed shifts during DRIFT or FT-IR Spectroscopy in general.[106,107] This is assumed to originate from a thermal excitation of the electrons from trap states below the conduction bands. By that the number of free electrons inside the bulk material increases, which also leads to an increase in conductivity. It is further assumed, that excited electrons might be in a quasi-free state, however trapped in interstitial zinc atoms.[108] Buckeridge *et al* showed that under reducing conditions at elevated temperatures deep states may be the reason for intrinsic n-type conductivity.[133] Furthermore, the conductivity of ZnO in the dark and illuminated has been investigated thoroughly in the past.[93-95] As commonly known, ZnO being a semiconductor material, an excitation of the electrons is also achieved by illumination with light at a wavelength of 385 nm.[102] During DRIFTS an excitation with UV light leads to a similar effect on the optical properties of the samples, as the one observed during thermal treatment. As illumination leads to creation of excitons, one can assume exciton luminescence being partly a reason for the observed phenomena. Exciton luminescence due to UV-irradiation was reported as continuation of earlier works[123,124], however the intensity decreases drastically at temperatures above 5 K up to a nearly total extinction at temperatures above 120 K.[87] Zhao *et al.* showed in a different work that exciton bands are still detectable in photoluminescence spectra of ZnO rods and particles at 300 K after excitation with a 325 nm laser beam.[134] The intensity of the strongest band at 371 nm at 5 K is shown to decrease as well as shift to 381 nm at 300 K. Further an additional broad emission band at 514 nm appears. This signal is attributed to originate from the presence of singly ionized oxygen atoms, zinc interstitials or oxygen vacancies. As the experiments in the work at hand are conducted at temperatures much higher than 300 K, the influence of exciton luminescence on the IR spectrum is uncertain and is brought into discussion with caution. Consequently, as mentioned above, the origin of the increased absorption in the IR was mainly coupled to the increased conductivity, when the sample is illuminated. In **Figure** 33(i) findings of E. Mollwo on the dependence of electrical current passed through a ZnO film are shown.[95] A similar experiment was conducted in the DRIFTS set-up in the current work. Untreated samples of commercial ZnO nanoparticles (Iolitec, in Figure 33 (ii)-(iii) denoted as "np") and self-prepared nanorods (in Figure 33 (ii)-(iii) denoted as "nr") were illuminated with light of 380-520 nm wavelength and the band height at 1800 cm^{-1} has been monitored. This band position was chosen since no species such as carbonates, water or other

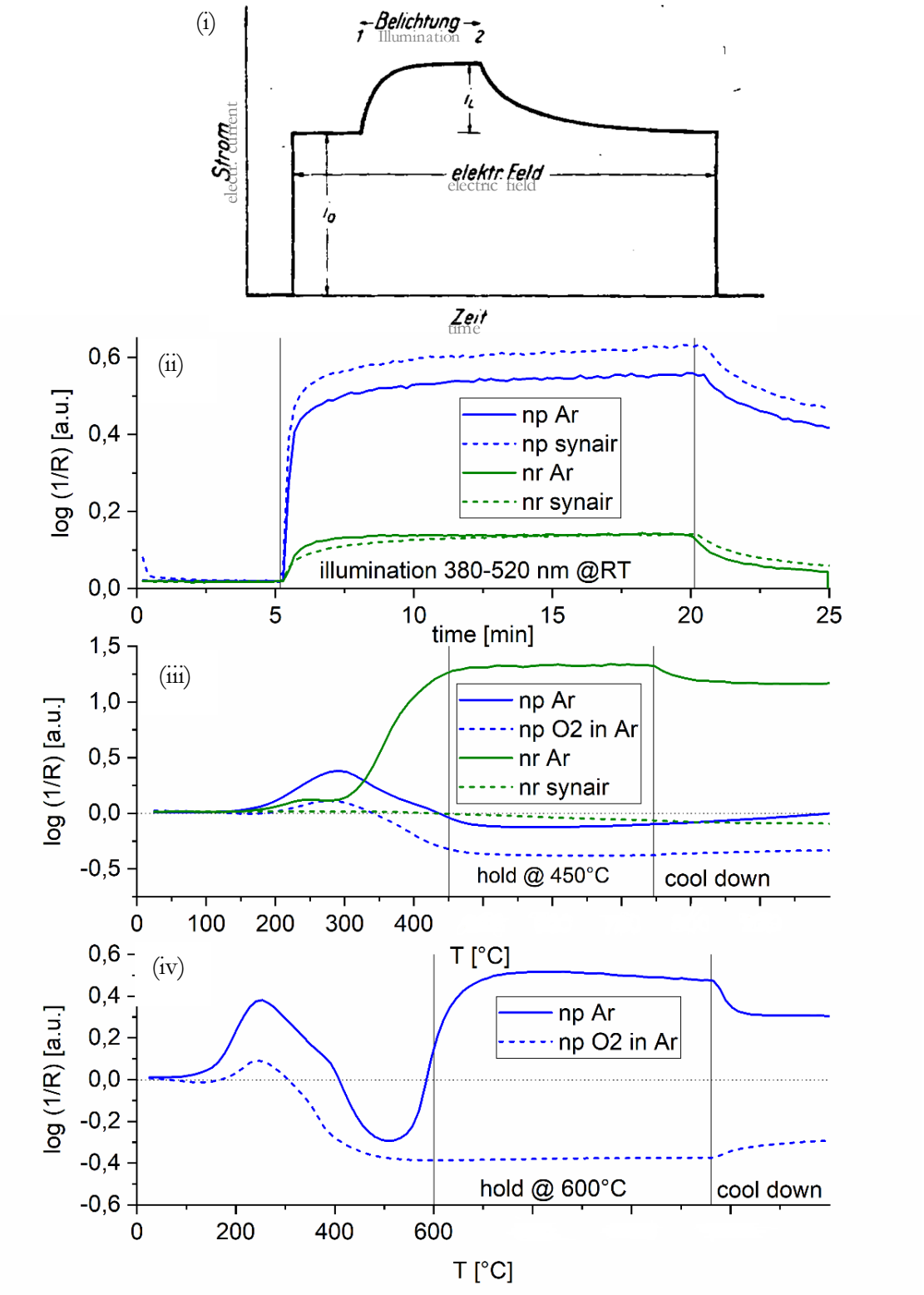

Figure 33: Schematic depiction of electrical current versus time in an ZnO sample in regard to darkness and illumination(i)[95]; Band intensity at 1800 cm-1 in DRIFTS measurements of (ii) unpretreated ZnO particles(np) and rods(nr) in Ar or synthetic air atmosphere in dependence of illumination with light of 380-520 nm wavelength; (iii) thermal treatment of ZnO particles and rods in argon or oxygen containing atmosphere to 450°C; (iv) thermal treatment of ZnO particles in argon or oxygen containing atmosphere to 600°C.

contribute to a rise or decrease of the signal intensity in this region during this simple experiment. By this the changes in the intensity can be assigned to changes of the optical properties due to illumination only. Even though illumination inevitably leads to heating of the sample, temperatures of around 35-40°C were measured. It is to be noted, that the temperature sensor is positioned in the bottom part of the Harrick-cell, while the light source is in close proximity to the surface of the sample which means the temperature at the surface might be even higher than 40°C.
However, fresh gas flow is being directed through the sample possibly leading to a complementary cooling of the sample surface, which was also discussed for reactions in similar reaction set-ups in the past.[135] In any case, it is assumed that during illumination of the sample temperatures below 250°C are reached, which is not enough to initiate optical changes of ZnO samples, as was shown in earlier works.[105,115] When comparing the results to the measurements of conductivity of ZnO in the dark and during illumination, a similar shape can be seen. It is therefore assumed that these events have the same origin and thus the excitation of electrons with light leads not only to an increased conductivity, but also to changes in the optical properties of ZnO. Besides excitation of electrons from trap states (or states inside the band gap) one may also excite from the valence band. Furthermore, a closer look was taken on the band height at 1800 cm^{-1} during the heating procedure of ZnO rods, which has been conducted prior to CO_2 adsorption experiments.[128] As seen in Fig. 1C heating ZnO rods to 450°C in Ar atmosphere leads to a significant increase of the band height, while particles seem to face no such increase, but a slight decrease in the band intensity – in both oxidative and reductive atmospheres. This slight decrease, however, according to the Boltzmann distribution, is mostly due to a higher number of lattice atoms being present in the first excited vibrational state at high temperatures. Therefore, when compared to the distribution at room temperature, less lattice atoms are available for excitation to higher vibrational states due illumination with infrared light. An increase in band intensity is achieved by heating to 600°C in Ar for particles, as shown in Fig. 1D, which can be assigned to the increased number of conduction electrons. Consequently, the structure of the material seems to have an effect on its behavior due to heat, which also might mean different behavior in terms of CO_2 adsorption and the influence of light. As was described earlier (Chapter 2.5), illumination of the sample with UV light leads to different possible events. When observing changes in optical properties desorption of oxygen or other adsorbate surface species is the most important one, as defect states and vacancies are being left empty and thus trapped electrons contribute to an increase in conductivity.[106] Figure 14 (p. 33) shows a simplified summary of the reasons for the changes of optical properties of ZnO regarding FT-IR measurements.

Unfortunately, the increase of the band intensity due to heating as well as illumination, is not only present at 1800 cm^{-1}, but throughout the whole spectral range, increasingly apparent at lower wavenumbers. As a result, the increased baseline completely covers the region of carbonate species (1040-1640 cm^{-1})[17,62] Since the effect is permanent and can be reversed by an oxidative thermal treatment only, it makes the qualitative investigation of CO_2 adsorption after reductive pretreatment or with UV-illumination rather difficult.

As can be seen in Figure 34 ZnO particles is the only sample featuring only a slight increase in band intensity around 250°C falling then back to an intensity close to the base level. Apart from ZnO SSS sample, which does not feature any apparent adsorbates (s. Figure 28), all other samples show a strong baseline bending or the so called "IR-blackening"[136]. Still, certain differences concerning the onset time and intensity of the "IR blackening" effect can be seen between all samples and can be attributed to the different morphologies of the samples. The electric behavior such as conductivity(which is connected to optical properties due to electron-phonon interactions,

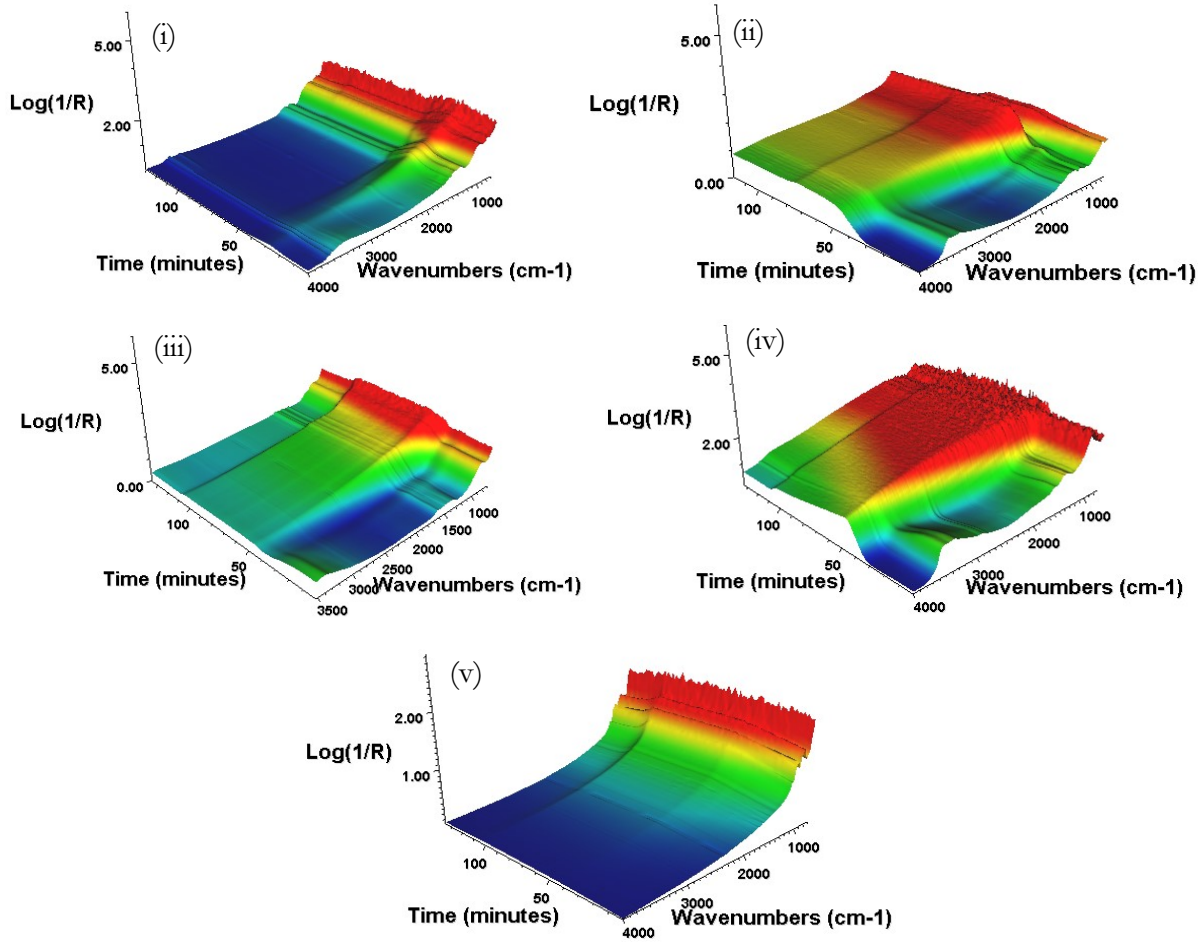

Figure 34: 3D depiction of series spectra recorded during thermal treatment of ZnO samples: (i) particles, (ii) rods, (iii) flowers, (iv) flakes, (v) SSS. A uniform heating procedure in 30 ml/min Ar flow was applied during all measurements: 0-50 min: heating from RT to 450°C with 10K/min; 50-110 min: holding at 450°C for 1 hour; 110 min – end: cooling down to room temperature.

(s. Chapter 2.2.5) of semiconductor materials relies among others on the morphology of the material as well as connection geometries which is known from literature.[137] Assuming ZnO nanoparticles have a small volume with large depletion layer between each other, the initial increase of the baseline is assumed to originate from desorption of some surface absorbate species like water or CO_2 without any permanent effect. ZnO rods, however, feature at least a tenfold length at roughly the same diameter as particles, which means a better charge carrier transfer within a single rod. Consequently, the effect is much more pronounced and permanent, than in particles. The same applies to flakes and flowers, which feature mostly similar initial shape of large ZnO plates, however at different stacking density. As shown in Figure 35, in an abstract 2D consideration all morphologies can be imagined as simple objects, where particles are dots, rods are strings and flakes as well as flowers are planes. According to that charge distribution and mobility is much better in a conjugated 2D plane object and decreases towards strings reaching a minimum in overall conductivity in dots due to existence of a depletion layer between the particle in both directions of the 2D space.

To better understand the origins of the effect a deeper search has been undertaken. As the excitement of electrons should not be directly visible in IR spectroscopy measurements, it felt natural to search for the connection between increased conductivity and changes in vibrational states of the material. Luckily, E. Mollwo and especially one of his students C. Klingshirn conducted most of their work, investigating the events in ZnO materials from the perspective of solid-state physics. Especially the investigations on phonons which are lattice vibrations of solid

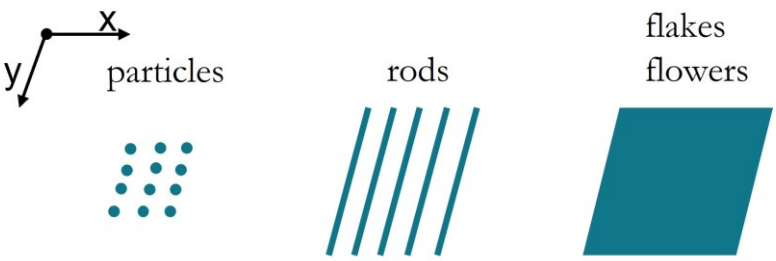

Charge distribution	particles	rods	flakes / flowers
x-direction	BAD	BAD	GOOD
y-direction	BAD	GOOD	GOOD

Figure 35: Schematic depiction of abstract consideration of charge carrier distribution and overall conductivity in ZnO materials with different morphologies.

materials (Chapter 2.2.4) and their possible interactions with electrons or excitons is of great interest in this work. Among numerous different stimulated or spontaneous events reported by Klingshirn[138] and references therein two correlations leading to the phenomena seen in the DRIFTS measurements are supposed to be most relevant. Increase of conductive electrons goes hand in hand with an increased creation of excitons or charge carrier pairs. The excitons, however, are of finite lifetime and a recombination of those may occur resulting in two processes. On one hand a radiative recombination of charge carrier pairs may take place under inelastic scattering of another free charge carrier e.g., an electron – into a higher state. This process occurs under energy and momentum conservation and thus results in indirect increase of lifetime and preservation of the number of excited free charge carriers. On the other hand, the recombination may take place under emission of one or more quanta from a plasmon-phonon mixed state. This is basically a quasiparticle which results from an interaction between plasmons and optical phonons. Further coupling to longitudinal optical phonons only is being assumed, even though the coupling to the phonon-plasmon mixed state is known to be stronger. As described earlier, optical phonons are elementary excitations of optical lattice vibrations (Chapter 2.2.4). The observed phenomena in DRIFT spectra may also be explained by the (phonon) drag-effect.[139-141] This describes the influence of the phonon drag i.e., a thermoelectric phonon transport effect occurring in metals and semiconductors. It is known that an electric current in a solid body is coupled to a shift of the Fermi-surface of the electronic system in the k-space. Due to occurring electron-phonon interactions phonons feature the tendency to shift within their own k-space to remain in an equilibrium with the electronic system. Therefore, a flow of electrons drags a flow of phonons, and vice versa. When irradiated with light in the range of self-absorption of the material, absorption of photons by free charge carriers includes absorption of the momentum of the electromagnetic wave as well as its energy. This may result in the translational motion of the electronic system which manifests in in form of electronic current. Thus, while free electrons or excited charge carriers cannot be detected by IR spectroscopy methods directly, the interaction of excited electrons with phonons leads to change of the optical properties of the material and thus to an indirect detection of free electrons in DRIFT spectra.

To sum up the discussed results and respective effects leading to observed phenomena Figure 36 offers a good overview. Thermal treatment in reductive atmosphere as well as illumination with UV light have a similar effect on the absorption in the infrared spectral range. Both seem to trigger the same chain of events, but at different points. Thermal treatment of ZnO in reductive atmosphere at temperatures over 250°C leads to a desorption of surface species from e.g., defect sites. Further oxygen vacancies, which have been also occupied by adsorbate, are being freed up

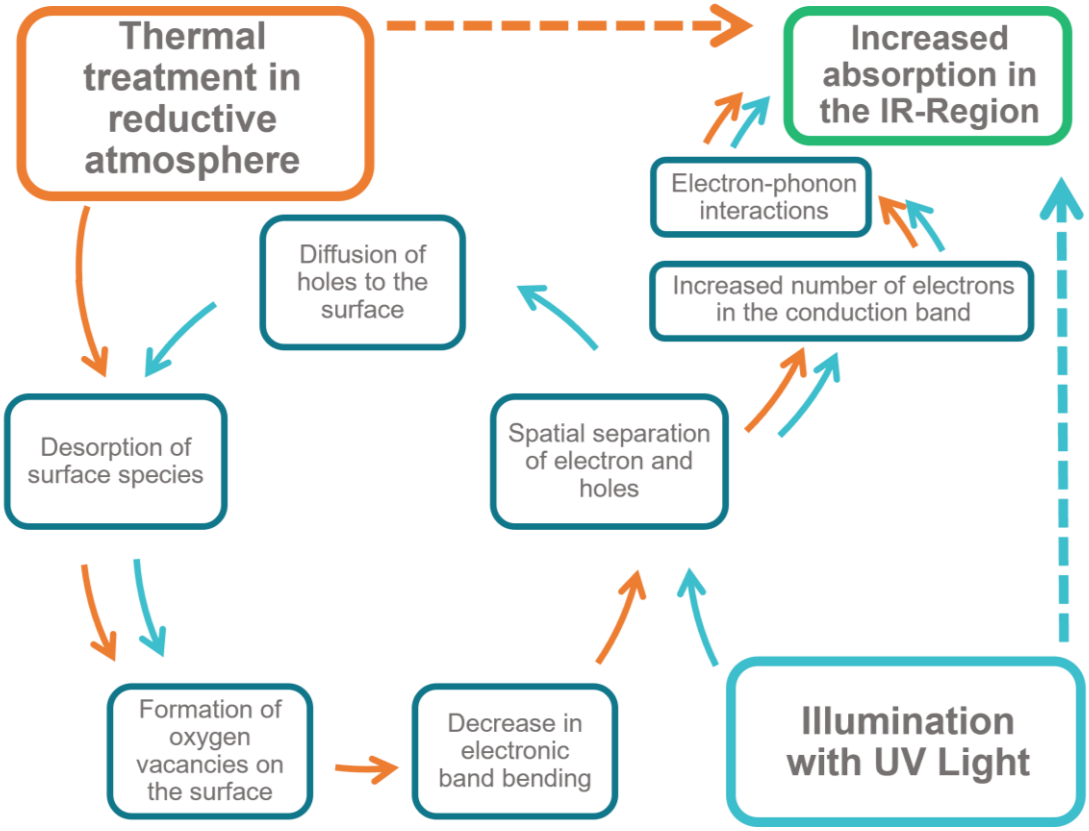

Figure 36: Schematic depiction of events leading to increased IR absorption of ZnO after thermal treatment in reductive atmosphere or illumination with UV light.

which leads to a decrease in electronic band bending of ZnO surface. By this, excited states are more easily available to electrons resulting in a spatial separation of electrons and holes and followingly higher possibility of thermally excited electrons. This means that overall, an increased number of free or conductive electrons are present in the conduction band. Due to interactions between electrons and phonons e.g., inelastic scattering of an electron with a phonon – a quanta of lattice vibrations – energy is being transferred to the vibrational modes of the crystal lattice, which can then more easily interact with IR light utilized in the vibrational spectroscopy. Illumination of ZnO with UV light leads to an excitation of electrons due to the energetic overlap of UV light and the band gap of ZnO. While the holes may diffuse to the surface leading to the desorption of surface species resulting in the creation of oxygen vacancies, the electrons are very likely to stay in the excited state due to the decreased electronic band bending. Finally, the free electrons in the conduction band may interact with the phonons leading again to an increased absorption of IR light.

3.7 CO_2 adsorption on ZnO materials

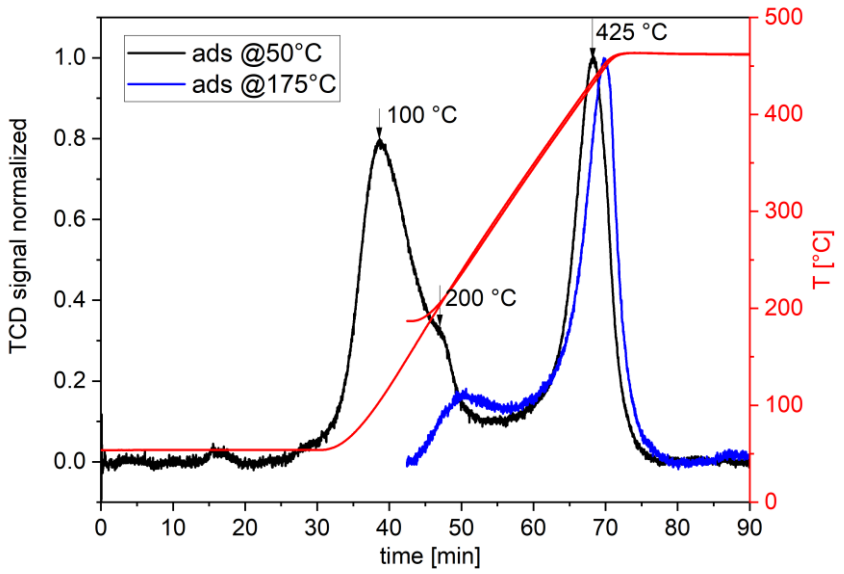

Figure 37: Normalized TCD signal recorded during the temperature programmed CO_2 desorption experiment after adsorbing CO_2 at 50°C(black) and 175°C(blue) on ZnO particles sample. Red curve belongs to the secondary y-axis and gives the temperature detected in the reaction chamber.

Main objective of this study was the investigation of CO_2 adsorption capability of different nanostructured ZnO material. Thus, preliminary adsorption experiments were conducted at different temperatures using Belcat II, while monitoring the outgoing gas stream by the QMS. In Figure 37 the desorbed CO_2 amount, which was calculated from QMS signal, is shown. At 50 °C the amount of detected CO_2 in nearly double of that at 175°C. As can be seen in the TPD measurement in Figure 37 ZnO features at least three different species of adsorbed CO_2, which are desorbed in different temperature ranges, leading to peak maxima at 100, 200 and 425 °C. When CO_2 is introduced at 175°C only the latter two species are being formed, shown by only two desorption peaks. Consequently, the obtained results show that the temperature has a great influence on the amount of adsorbed CO_2, which is in good agreement with the results presented in literature, but also in an earlier work of Lyashenko and Gorokhovatskii[142], shown in Figure 38(left). Here the researchers investigated not only the influence of different temperatures on the adsorption of CO_2 on ZnO, but also the influence of illumination with UV light. As this is also one of the main objectives of this work, the results of this special publication are of great interest. However, as the work by Lyashenko and Gorokhovatskii features simple ZnO material without any significant structure, it serves as a rough guideline, for working with materials of reduced dimensionality or nanomaterials as these are known to show unique behavior. Besides variation of adsorption temperature, the influence of pretreatment atmosphere was investigated.

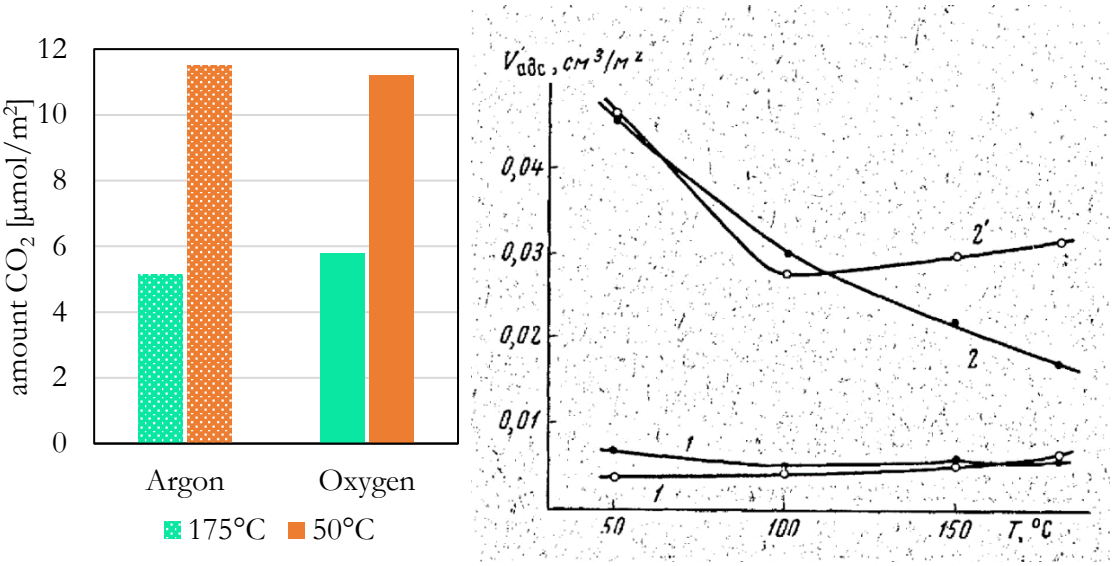

Figure 38: (left)desorbed CO2 amount after adsorption of CO_2 at 20% CO2 in Ar and 175°C or 50°C on ZnO particles sample thermally pretreated in (left) pure Ar or (right) 20% O_2 in Ar; (right) results of CO_2 adsorption presented by Lyashenko and Gorokhovatskii[142]. A comparison between (1) photocatalytic not active sample, due to thermal pretreatment in vacuum at 200 °C for 3h and (2) photocatalytic active sample, pretreated at 520 °C in 88 mm Hg (0.117 bar) for 10 h; additional comparison between adsorption (blank) with additional illumination and (filled,´) without.

Thermal pretreatment in pure Argon and 20% Oxygen in Argon had no influence on the adsorption behavior of ZnO. This, however, is contrary to the results found in literature. This may have several reasons, mainly due to the experimental set-up as well as the leakage in the used device Belcat II. After thermal pre-treatment of the material, when changing to CO_2 some air was detected in the gas flow by the QMS. As the gas flow is being regulated via automatic valves in a closed housing, one cannot exclude leaks inside the device. Even though the amount of detected oxygen is very low, it certainly may be enough to adsorb to the freshly pretreated (possibly) defect and oxygen vacancy rich material, eliminating potential adsorption sites for the CO_2. As in both cases the pretreated sample would have come in contact with oxygen, the variation of pretreatment atmosphere does not have the expected effect.

Further CO_2 adsorption experiments on as-synthesized nanostructured ZnO-based materials have been conducted by means of DRIFTS. FT-IR Spectroscopy allows to observe different molecular species adsorbed on the surface of the analyzed materials and thus gain insight into mechanistic steps taking place. Due to the IR-Blackening effects described earlier, qualitative investigations of CO_2 adsorption were possible only on the not illuminated commercial ZnO particles. Table 5 summarizes vibrational features as well as the assignment to corresponding carbon containing species formed due to adsorption of CO_2. The respective DRIFT spectra as well as reasons for band assignments are discussed in the following.

Table 5: Summary vibrational modes and identified species formed during adsorption of CO_2 on ZnO particles in the dark. Corresponding wavenumbers are given in [cm^{-1}].

Dark			
vibrational mode	carboxylate	bidentate carbonate	bidentate bicarbonate
ν_a(OCO)	1550	1678	1638
	1348	1307	1420
δ(COH)	-	-	1230

In Figure 39 DRIFT spectra recorded during the CO_2 adsorption step on ZnO particles, as well as the subsequent purging with Ar are shown. The very first spectrum denoted as "start" was taken as baseline and subtracted from all following spectra of the series. With this the changes in the spectra could be assigned to introduction of CO_2 only. Numerous bands can be found arising after addition of CO_2 to the gas flow, which indicated the formation of different carbonate species. As most bands are broad one can assume that the formation takes place on a variety of adsorption sites, indicating a highly versatile surface nature. This is in good agreement with the shape of particles featuring numerous kinks and steps in order to maintain a ball-like shape. After 30 min exposure to CO_2 the most prominent features are at 1638 and 1420 cm^{-1}. Due to the LO-TO splitting explained earlier (Chapter 2.3.1) both originate from a single anti-symmetrical vibration of OCO. At 1230 cm^{-1} (shifted from 1219 cm^{-1}) another band arises, which can be assigned to deformation vibration of OH molecular groups.[62] These three signals are characteristic for bidentate bicarbonate species and indicate a preferable formation. Further, the feature at 1638 cm^{-1} has a shoulder-signal indicating another feature at 1675 cm^{-1}. In study by Saussey *et al.* this band

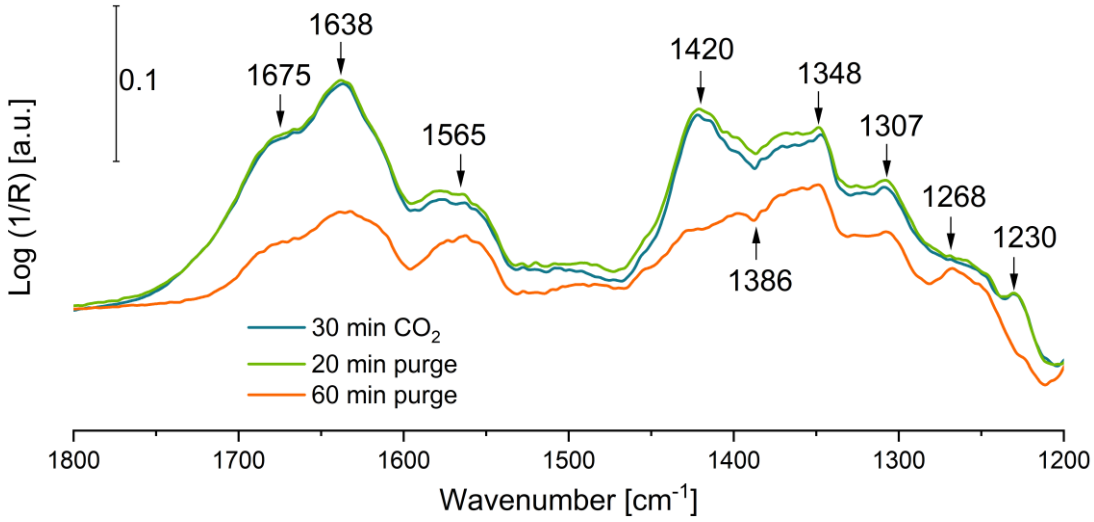

Figure 39: DRIFT difference spectra recorded during CO_2 adsorption and subsequent purging with Ar on ZnO particles sample after thermal pretreatment in Ar.

was shown to arise when more than 18 μmolg^{-1} of CO_2 are being adsorbed while forming bidentate carbonates.[143] As in the same study a second band is being reported at around 1307 cm^{-1}, and is also found in the given spectra, the formation of bidentate carbonates is confirmed further. According to literature source mentioned above[62], signals characteristic for carboxylate species are positioned at 1523 and 1336 cm^{-1}. While in the given spectrum a slightly shifted band can be found around 1348 cm^{-1}, the complementary feature around 1523 cm^{-1} is not clearly visible. According to literature[17] the band at lower wavenumbers is more intense, than the one at higher wavenumbers. It is therefore assumed that both features are shifted likewise by about 15 cm^{-1} and thus the band around 1523 cm^{-1} contributes as a shoulder to the broad band around 1565 cm^{-1}. Bands characteristic for the monodentate carbonates, which are being reported at 1474 and 1386 cm^{-1} cannot be found in the spectrum. Moreover, at 1386 cm^{-1} the spectrum features a clear drop. As the given spectra are difference spectra, a negative band is caused by a disappearing of species. Consequently, one can assume that monodentate carbonates are present before introduction of CO_2 but are removed or transformed to other species as soon as CO_2 is added to the atmosphere. In general, it can be said, that the literature offers a variety of suggestions concerning band assignment. Contrary to numerous references for adsorbed CO_2 and carbonates on ZnO single crystal surfaces, for ZnO particles a perfect assignment of bands and thus an unambiguous identification of surface species is unfortunately not possible. During the first 20 min of purging with Ar only no significant changes are observed, mainly due to the presence of residual CO_2 in the gas stream or the atmosphere inside the measurement chamber. After one hour of purging with Ar the intensity of bands characteristic for adsorbed bicarbonates decreases noticeably. Apart from a further decrease in intensity of the band at 1350 cm^{-1}, indicating a decrease in adsorbed monodentate carbonates, the intensity of all other bands remains unchanged. It is therefore likely that bicarbonates and some monodentate carbonates are desorbed, rather than transformed to other carbonate species.

A qualitative evaluation of the adsorbed CO_2 species was performed through analysis of peak positions of the calibrated CO_2 signal recorded during the TPD experiment i.e., the QMS measurement in the course of the whole thermal post treatment procedure. Further, the results of the same measurement were utilized for a quantitative evaluation of the adsorbed CO_2 species through integration of the calibrated CO_2 signal.

As can be seen in Figure 40, and already discussed earlier (Figure 37) two main peaks are apparent in QMS spectra of experiments with ZnO particles. A slight shoulder in the recorded mass traces is found at around 200 °C, when CO_2 was adsorbed under illumination. However, this peak was also detected in previous TPD measurements in the BelcatII (s. Figure 37), where CO_2 was

adsorbed in the dark. Comparing measurements of the other materials, desorption traces recorded after CO_2 adsorption with illumination do not differ from the one where adsorption was performed in the dark. This is the case for most ZnO nanomaterials, which were investigated in this work. Thus, illumination with UV-light apparently does not lead to significant formation of new carbonate species, which might result in new desorption peaks during the subsequent TPD measurements. Since the shape of the TPD (QMS) signal does not change, neither new carbon containing species are being promoted, nor is the preference of the material for a certain adsorption species changed through the illumination with UV-light during CO_2 adsorption.

However, as summarized in Figure 41 quantitative determination of the amount of adsorbed CO_2 shows not only a difference between different morphologies, but also whether the respective sample was illuminated during the adsorption step or not. SSS ZnO hardly adsorbs CO_2, (but also

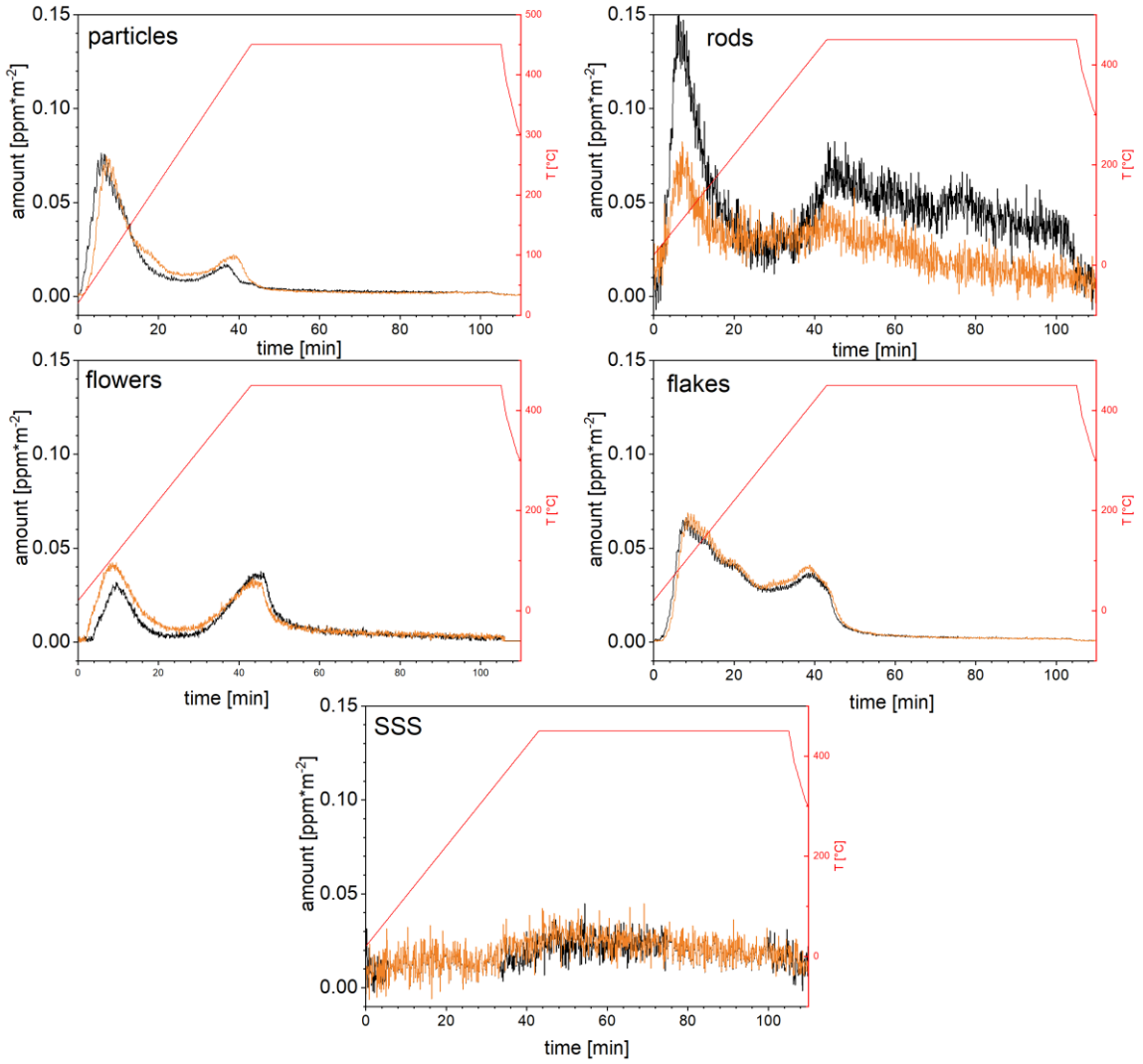

Figure 40: Mass traces for effluent CO_2 recorded during the thermal treatment after adsorption of CO_2 under illumination(yellow) and in the dark (black). All concentrations were normalized by the surface area of the respective material.

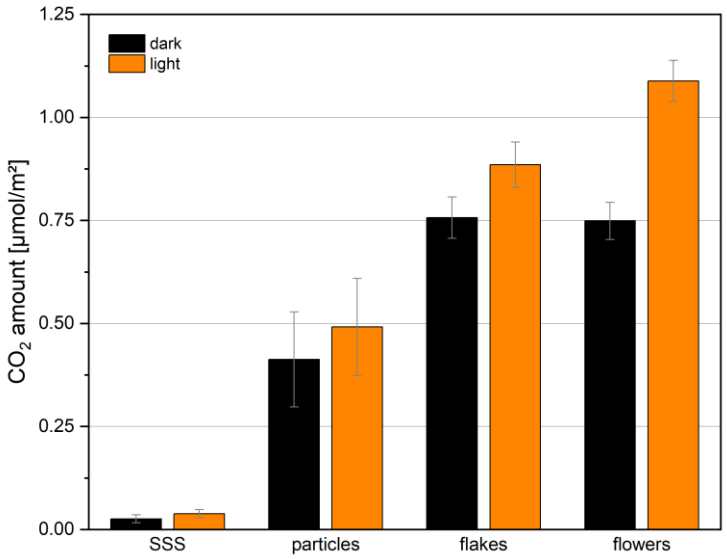

Figure 41: Summarized results of CO_2 desorption experiments after thermal treatment at 450 °C in Argon and CO_2 adsorption at room temperature. The DRIFTS set-up was unitized for all measurements.

other gas phase molecules) which was already indicated by the DRIFTS as well as BET measurements. This is probably due to the large perfect crystalline surface planes present in the material with only some defect sites, and thus a low number of available adsorption sites. Furthermore, this material has by far the smallest surface to bulk ratio of all investigated samples. For the SSS sample, illumination with UV-light increases the amount of adsorbed CO_2 ever slightly, which is however in the margin of error. It showed an average desorption amount of 0.03±0.01 µmolm^{-2}, while when illuminated this value was increased to 0.04±0.01 µmolm^{-2}. ZnO particles featured much more adsorbed CO_2 detected during the subsequent TPD measurement resulting in calculated values of 0.41±0.11 for adsorption in the dark and 0.49±0.12 for adsorption under illumination. Due to large deviations between the measurements under same conditions, this difference is to be taken into account with caution. ZnO flakes show similar desorption profiles for dark and illuminated CO_2 adsorption with calculated values of 0.76±0.05 µmolm^{-2} and 0.89±0.06 µmolm^{-2}, respective. ZnO flowers sample shows two peaks indicating at least two different desorption species. After the illuminated CO_2 adsorption, however, the first peaks at about 100 °C is more intense. This leads to an overall higher desorption value of 0.09±0.05 µmolm^{-2} compared to 0.75±0.04 µmolm^{-2} after adsorption in the dark. As was shown in earlier studies some, surface oxygen species are being desorbed by UV-illumination only. While thermal treatment in reductive atmosphere also leads to desorption of oxygen and formation of active adsorption sites on the surface of the material, some oxygen species might be desorbed only during UV illumination. Followingly, when the sample is illuminated with UV light during the CO_2 adsorption experiment, more adsorption sites may be created due to desorption of oxygen. Since

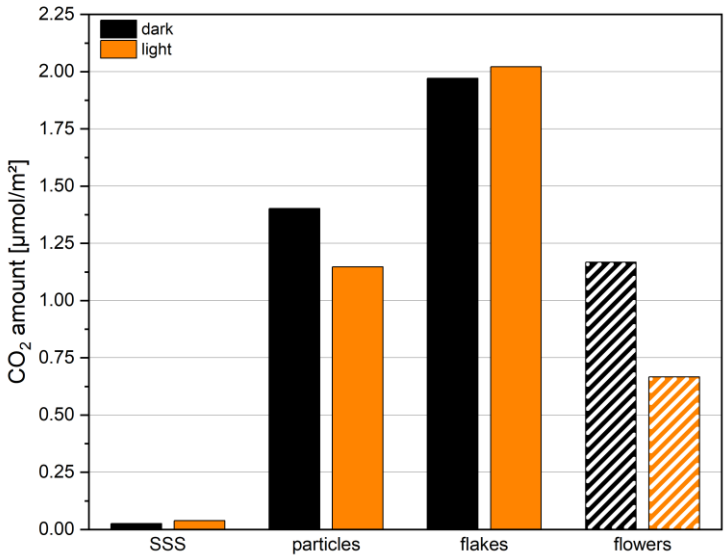

Figure 42: Summarized results of CO_2 desorption experiments after thermal treatment at 450 °C in Argon and CO_2 adsorption at room temperature in the dark or under illumination. The photo-TPD set-up was unitized for all measurements.

the observation of formation of surface species during the adsorption experiment was not possible by means of DRIFTS, one cannot exclude the desorption of already existing carbonate species. Further, as the CO_2 which is introduced during the adsorption step is not instantly being removed from the measurement chamber, but follows a rather long-lasting purging process, a subsequent adsorption of CO_2 after the illumination cannot be excluded. This assumption also explains why the illumination does not influence the strength of adsorption but only the amount of adsorbed CO_2.

Further desorption measurements were performed utilizing the photo-TPD set-up presented in Chapter 3.1.4. As can be seen in Figure 42, the overall trend of CO_2 adsorption capabilities SSS<particle<flakes was confirmed, while the values for desorbed CO_2 are nearly 3-fold of the results summarized in Figure 41. However, unlike previously discussed TPD measurements in the DRIFTS cell, the flowers sample showed much less desorbed CO_2, than flakes and particles material. As this trend was similar for both desorption experiments after illuminated as well as dark adsorption of CO_2, some sort of decay of the sample itself is suggested to be the problem for decreased CO_2 adsorption capability of the material. Consequently, ZnO flakes showed the highest amount of desorbed CO_2. The overall higher amount of desorbed CO_2 is attributed to the quartz cell utilized for the photo TPD measurement. It features lower sample bed height due to better sample distribution inside the cell. This ensures superior accessibility of the turbulent gas flow present in cell to the whole sample mass. Compared to this, the packed bed filling of the sample

inside the Harrick cell features only a small exit on the bottom, which may lead to decreased accessibility of the gas flow to the sample.

Once again, SSS material showed poor CO_2 adsorption and while there is a difference between illuminated and dark adsorption, it is being pointed out with caution. For particles, desorption traces of CO_2 on previously illuminated sample were lower than for the one in the dark. This is contrary to the previously shown trend, however, within the margin of error. ZnO flakes show slightly more desorbed CO_2 after illuminated CO_2 adsorption than after adsorption in the dark. All in all, the previously suggested influence of light on the adsorption capabilities of each material was not confirmed for the whole range of materials. This contradicts the assumption that an evenly spread-out sample provides increased accessibility of the illumination to the sample, and not only to the upper surface layer (which is the case in the Harrick cell), which would increase the assumed positive effect of illumination on adsorption of CO_2.

3.8 Influence of UV-illumination on CO_2 adsorption on TiO_2-based materials

CO_2 adsorption experiments have been conducted on TiO_2 based materials. In the following CO_2 adsorption on P25, Anatase and modified P25 material[144] (denoted as m-TiO_2) are compared. The influence of the organic shell present in the modified material as well as implementation of light during the CO_2 adsorption is to be outlined. The m-TiO_2 sample was provided by Dr. Nikolaos Moustakas, and the results presented herein will contribute to a joint publication.

To show the difficulty of spectra analysis, a single difference spectrum of TiO_2 after CO_2 adsorption is presented in the range from 1800 to 1200 cm^{-1} in Figure 43 including graphical summary of literature references from Table 1. It felt therefore more reasonable to first identify groups of bands behaving similarly throughout the experiment and try to assign those to vibrational modes of corresponding adsorbed species in the next step. In case of OH containing species, deformation bands found around 1225 cm^{-1} were also taken into consideration. When a formate species was assumed to be present, the spectral range from 2800-3000 cm^{-1} was investigated more closely in order to identify characteristic signals for stretching vibrations of CH groups. The study by Mino, Spoto and Ferrari from 2014 was mainly utilized for the identification and assignment of features as well as determination of corresponding adsorbed carbonate species. Due to high quality of theoretical calculations and good agreement with experimentally measured values measured

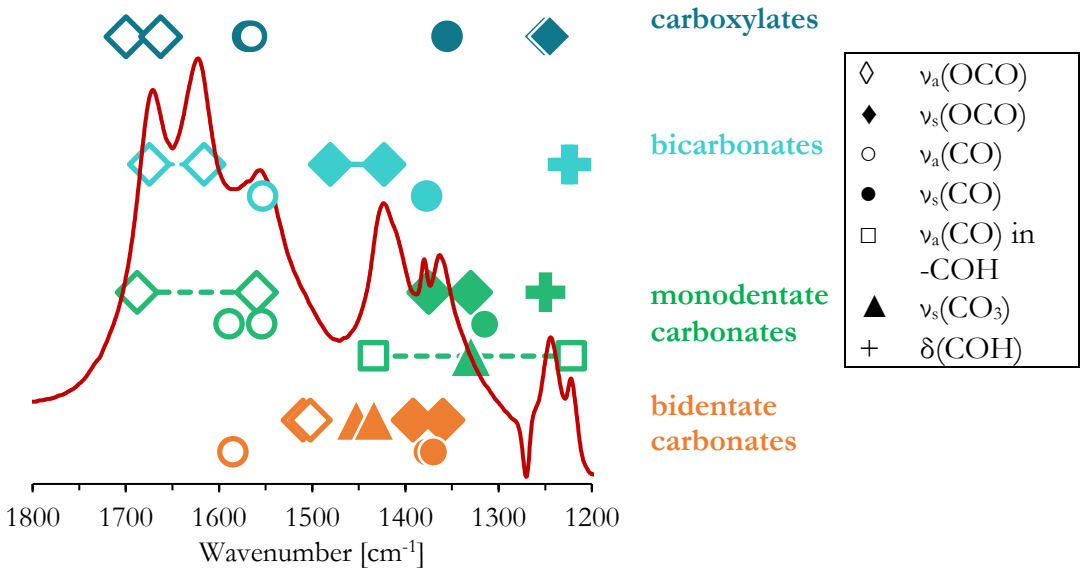

Figure 43: Schematic visualization of feature assignment to vibrational modes in different carbonate species formed on TiO_2 samples due to adsorption of CO_2 according to literature sources of last 30 years summarized in Table 1. An exemplary DRIFT spectrum of adsorbed CO_2 on TiO_2 was added additionally.

values it offered the best and most reliable basis. For each material all identified species including assigned features are summarized in a corresponding table.

Unlike ZnO samples investigated earlier, m-TiO_2 sample featured low stability at temperatures higher than 675 K. Thus, all TiO_2 based samples were heated only to 675 K during the thermal pretreatment steps (step (I) and step (III)). Moreover, none of the investigated samples experienced baseline bending or the "IR-blackening" during either the thermal pre-treatment or illumination with UV light to the same extent as the ZnO samples shown earlier. However, baseline bending has been reported by earlier research for TiO_2 based materials. Lüken *et al.* utilized this phenomenon during ATR-IR measurements of 2-propanol adsorption on gold modified TiO_2 oxidation catalyst to monitor the accumulation of excess electrons[15]. This confirms the assumptions and early findings[93-95,106] that the baseline bending in the ZnO (and TiO_2) is due to increased amount of conduction electrons. However, in the following experiments no severe baseline bending was detected, as unlike in ATR-IR measurements conducted by Lüken *et al.* no hole-scavenger (being potential adsorbates) were present in the atmosphere during the measurements. While some samples featured a slight increase in the baseline intensity, the relevant range of the spectrum (1200-1800 cm^{-1}) remained mostly unchanged. This resulted in successful recording of DRIFT spectra for CO_2 adsorption experiments after the thermal treatment and even under illumination.

Table 6 summarizes assignment of vibrational features to carbon containing species formed due to adsorption of CO_2 on anatase sample and recorded by means of DRIFTS. The reasons for particular band assignment are discussed in the following.

Table 6: Summary vibrational modes and identified species formed during adsorption of CO_2 on anatase. Corresponding wavenumbers are given in [cm^{-1}].

vibrational mode	lin. CO_2	carboxylate	monodentate carbonate	monodentate bicarbonate	bidentate bicarbonate
Dark					
2δ(OCO)	1264	-	-	-	-
ν_a(CO)	1346	1346	1586 1378	1670 1424	1631 1448
δ(COH)	-	-	-	1221	1218
Light					
2δ(OCO)	1264	-	-	-	-
ν_a(CO)	-	-	1590 1378	1675 1430	1625 | 1613 1444 | 1501
δ(COH)	-	-	-	1230	1218

Following figures show the difference spectra recorded for all three TiO_2-based materials mentioned above during different steps of the CO_2 adsorption experiment. Top section of each figure features a comparison between CO_2 adsorption conducted in the dark and under illumination as well as two spectra recorded during subsequent purging with Ar. Bottom section shows difference spectra at selected temperatures recorded during thermal post treatment in Ar. Corresponding (non-difference) spectra can be found in appendix (Figure A. 1 – Figure A. 3)

Figure 44(i) shows spectra recorded during the CO_2 adsorption experiment on anatase in the dark. When CO_2 is introduced into the reaction cell, a positive band appears at 1264 cm^{-1} and a strong negative band is formed at 1346 cm^{-1}. While the origin of the feature at 1264 cm^{-1} can be assigned to the first overtone of the deformation mode of an OCO group (2δ(OCO)) in linearly adsorbed CO_2[58], the signal at 1346 cm^{-1} may originate from symmetrical CO stretching ν_s(CO) being assigned to adsorbed carboxylate species by Bando *et al.*[76]. Based on a study by Ramis, Busca and Lorenzelli[145] this feature might also be part of the doublet originating from the Fermi resonance between the ν_s(CO) positioned around 1376 cm^{-1} and the 2δ(OCO) at 1264 cm^{-1} both originating from linearly adsorbed CO_2 on the (101) surface. This assignment, however, requires a strong blue shift of ν_s(CO) feature by about 30 cm^{-1} due to some sort of surface contribution or coverage dependent effect. According to the raw spectra of this measurement (Figure A. 1(i)), these features are present in the beginning of the adsorption step. This indicates the presence of temperature-stable surface species, as they seem not to be affected by preliminary thermal treatment at 675 K in Ar. Throughout the measurement not only the intensity of the feature at 1346 cm^{-1} decreases, but its peak position

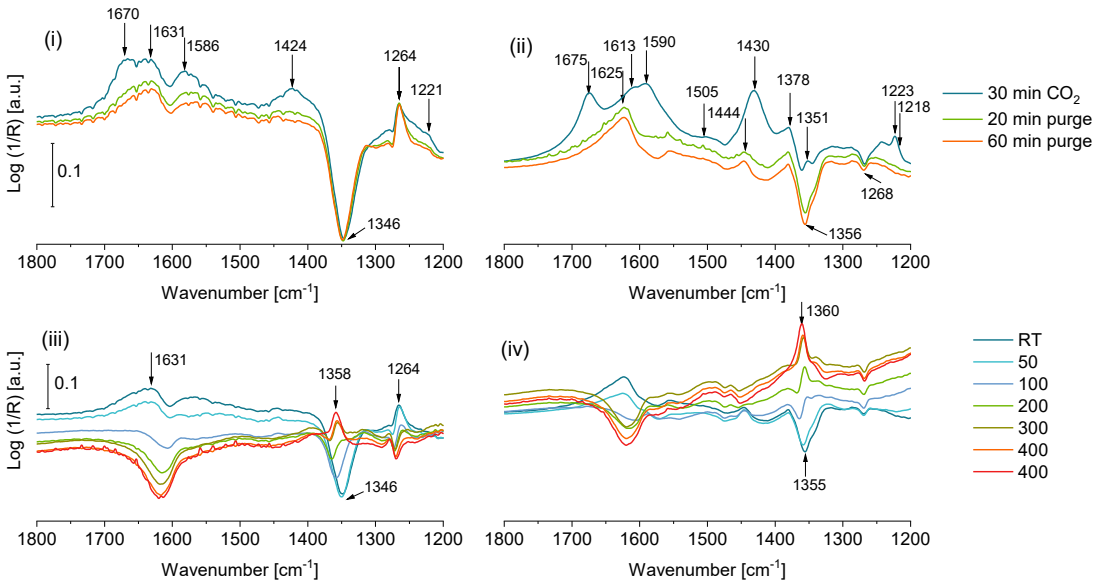

Figure 44: Difference DRIFT spectra recorded during the CO_2 adsorption experiment in dark(i) and under illumination(ii) as well as the subsequent thermal treatment((iii), (iv)) of the anatase sample. The last spectra of the top depictions (red) are the first spectra of the bottom depictions (dark teal).

shifts to 1324 cm^{-1} as well. It is well known, that increased coverage of the surface may lead to interactions between the adsorbates leading to red shifts of the corresponding feature in the IR-spectrum. The decrease in intensity indicates a decrease in the amount of this species, which results in weakening of the coverage-dependent effect leading to a red shift of the feature to lower wavenumbers. Further, weak features are formed at 1670 and 1424 cm^{-1} as well as 1221 cm^{-1}(the latter feature is better visible in raw spectra Figure A. 1(i)), which can be assigned to the doublet of the anti-symmetric stretching ν_a(CO) and deformation mode δ(COH) in monodentate bicarbonates, respectively.[58] In the last decades features simultaneously appearing around 1670 and 1221 cm^{-1} were very often assigned to ν_a(OCO) and ν_s(OCO) modes in adsorbed carboxylate species.[59,62,75,146] This, however, is a wrong assignment postulated by Rasko and Solymosi in 1994[63], which was cited numerous times throughout the years leading unfortunately to an accumulation of wrong assumptions. On one hand, the vibrational frequencies of ν_s(OCO) modes are expected at much higher wavenumbers (around 1350-1500 cm^{-1}), while assignment of the signal at 1221 cm^{-1} to δ(COH) is more reasonable as this feature is mostly found between 1200-1250 cm^{-1}. On the other hand, both features (1670 and 1221 cm^{-1}) disappear as soon as CO_2 is being removed from the atmosphere, indicating the according surface species to be labile. Assignment of these signals to monodentate bicarbonates, which not only feature an OH group, but also low formation energies (and thus easy desorption) is therefore a much more reasonable choice. Another weak band arises at 1586 cm^{-1}. In the work of Mino, Spoto and Ferrari[58] it was shown that the corresponding second feature which is created by the double degenerate splitting of the

antisymmetric stretching due to adsorption and thus required for the unambiguous assignment to ν_a(CO) in monodentate carbonates, is positioned around 1378 cm^{-1}. However, the intensity of the latter is expected to be more than 10 times lower. Combined with the overall low intensity of the difference spectra at hand this could mean that here the feature is not visible at all. One last broad band at 1631 cm^{-1}, which is already present in the beginning of the measurement, is assigned to the additional formation of bidentate bicarbonate species throughout the experiment. Again, a reliable assignment to the ν_a(CO) vibration requires a second feature of the doublet at 1448 cm^{-1} as well as the feature for δ(COH) vibrational mode at around 1218 cm^{-1}. Both can be better seen in the corresponding raw spectra of the measurement (Figure A. 1(i)), while still being very weak. In the difference spectra in Figure 44(i) these features are contributing to the tailing and shoulders of the broad signals around 1580 and 1240 cm^{-1} and are therefore not clearly visible.

As soon as CO_2 is removed from the gas feed and slowly purged out of the reaction chamber, monodentate bicarbonates are being desorbed as the corresponding features decrease and disappear. Meanwhile, characteristic features of monodentate carbonates and bidentate bicarbonates decrease in intensity only during the subsequent thermal treatment of the sample which is seen in the DRIFT spectra in Figure 44(iii). This indicates a desorption or decomposition of the strongly adsorbed species requiring higher temperatures due to higher adsorption energies. Moreover, during the thermal treatment features at 1348 and 1264 cm^{-1} show a reverse behavior compared to the CO_2 adsorption and desorption step. As mentioned earlier, this might be due to the presence of a certain surface species even after the thermal pretreatment. With additional CO_2 available throughout the adsorption experiment the latter may participate in the formation of other carbonate species leading to decrease in the intensity of their initial features. When the less strongly bound species are desorbed, the initial high temperature species are uncovered again which is signalized by reappearing of the corresponding vibrational features as can be seen in Figure 44(iii). Figure 44(ii) shows the DRIFT spectra of the CO_2 desorption, after light-assisted CO_2 adsorption. Similar to results shown in Figure 44(i), strong features at 1675, 1430 and 1223 cm^{-1} indicate the formation of monodentate bicarbonates. Further, monodentate carbonates are being formed as positive features representing the corresponding ν_a(CO) appear at 1590 and 1378 cm^{-1}.[58] As the intensity of the 2δ(OCO) feature at 1268 cm^{-1} is decreasing throughout the measurement, desorption or transformation of initially linearly adsorbed CO_2 is also possible. Further, a strong negative feature appears around 1355 cm^{-1}. However, unlike the measurement of CO_2 adsorption in the dark (Figure 44(i)), this signal features two bands: one increasingly negative feature at 1356 and a weaker positive one at 1351 cm^{-1}. Different literature sources assign different vibrational modes to signals in this region. In general, a feature at around 1355 cm^{-1} has been previously

assigned to ν_s(OCO) in bidentate carbonates[62,81], ν_s(OCO) in monodentate carbonates[59,79] or ν_s(CO) in carboxylates[76]. Here, however, an unambiguous and well-founded assignment is not possible. Nevertheless, it is suggested, that the negative signal originates from a spectator species which is covered during the adsorption experiment, while the positive signal is due to some newly formed species. When CO_2 is removed from the atmosphere monodentate carbonates and bicarbonates seem to be desorbed, as the corresponding features disappear in the spectrum. However, several bands remain visible, such as signals at 1625, 1444 and 1218 cm^{-1} which indicate the presence of stable bridging bidentate bicarbonate species.[58] This species might have been formed in presence of CO_2 already, however the characteristic features contributed to the strong signals dominated by monodentate species and were thus not clearly visible. A chelating bidentate bicarbonate species can be assumed, as weak shoulders at 1613 and 1505 cm^{-1} can be seen in the spectrum.[58] Spectra recorded during the thermal post-treatment(Figure 44(iv)) show mostly negative features indicating desorption of adsorbed carbonate species. Similar to the thermal post treatment after the adsorption experiment in the dark, positive bands in the region of 1350 cm^{-1} arise, indicating formation or rather uncovering of high temperature spectator species.

Table 7 gives a summary of vibrational features as well as the assignment to corresponding carbon containing species formed due to adsorption of CO_2 on P25 sample and recorded by means of DRIFTS. The respective DRIFT spectra as well as reasons for particular band assignments are discussed in the following.

Table 7: Summary vibrational modes and identified species formed during adsorption of CO_2 on P25. Corresponding wavenumbers are given in [cm^{-1}].

Dark						
vibrational mode	free carbonate	formate	monodent. carbonate	bident. carbonate	monodent. bicarbonate	bident. bicarbonate
ν_a(CO)	1407	-	1568 1378	-	1670 1424	1625 1444
δ(COH)	-	-	-	-	1252	1230
Light						
ν(CH)	-	2960 2872	-	-	-	-
ν_a(CO)	-	1550 1370	1584 1378	1575 1360	1670 1432	1625 1505
δ(COH)	-	-	-	-	1219	1218

Figure 45(i) shows DRIFT spectra recorded during the CO_2 adsorption and desorption steps on thermally pretreated P25 material. Moreover, raw spectra of the measurement (Figure A. 2(i)) show existing broad features in this spectral region indicating the presence of numerous carbonate species prior to CO_2 adsorption step. Due to bands at 1625 and 1444 cm^{-1} bridging bidentate

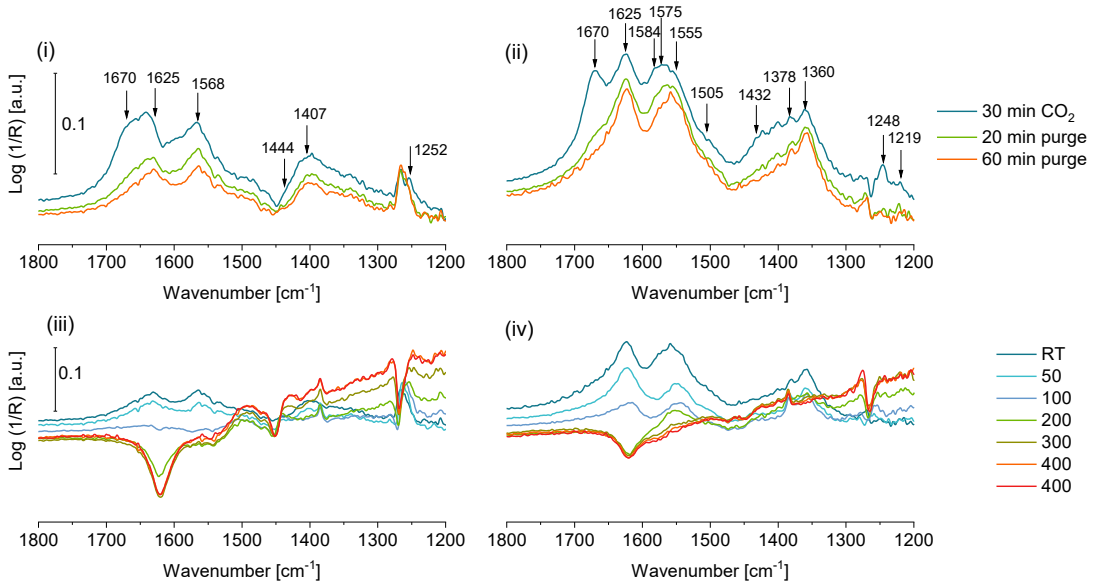

Figure 45: Difference DRIFT spectra recorded during the CO_2 adsorption experiment in dark(i) and under illumination(ii) as well as the subsequent thermal treatment((iii), (iv)) of the P25 sample. The last spectra of the top depictions (red) are the first spectra of the bottom depictions (dark teal).

bicarbonates are assumed to exist. When CO_2 was introduced into the reaction cell a broad feature at 1407 cm^{-1} appears and is assigned to ν_a(CO) in free carbonate. Due to its three-fold symmetry the ν_s(CO) vibrational mode does not lead to a change in the dipole moment of the molecule and is therefore IR inactive. Further, a strong feature arises at 1670 cm^{-1}, while additionally increasing the intensity of the previously existing band at 1626 cm^{-1}. Assignment of the signal at 1670 cm^{-1} to ν_a(CO) in additional bidentate bicarbonates species requires complementary signals at 1497 cm^{-1} as well as at 1230 cm^{-1} for the corresponding δ(COH) vibrational mode. While the feature at 1497 cm^{-1} is presumably part of the broad shoulder around 1500 cm^{-1}, the signal for δ(COH) is not apparent. According to theoretical calculations this signal, however, features a much lower intensity and may therefore be not visible in this spectra.[58] The band at 1670 cm^{-1} is assumed to originate from ν_a(CO) but cannot be assigned to any adsorbed species unambiguously. As its intensity decreases, when CO_2 is purged out of the reaction cell, it is assumed to indicate formation of a weakly bound carbonate species during CO_2 adsorption step. Simultaneously the signal at 1252 cm^{-1} which is assigned to δ(COH) features a decrease in intensity. Therefore, both signals are assigned to formation of weakly bound monodentate bicarbonate. Further, a strong band appears around 1568 cm^{-1} and is attributed to ν_a(CO) in monodentate carbonate.[58] The corresponding second feature of the doublet at 1378 cm^{-1} is assumed to be part of the broad band around 1400 cm^{-1}. DRIFT spectra of the subsequent thermal treatment (s. Figure 45(iii)) indicate the desorption or decomposition of bidentate carbonates, as the corresponding features decrease in intensity. Moreover, negative signals appear at 1444, 1404 and 1269 cm^{-1} which might lead to the assumption

that the corresponding carbonate species are desorbed. However, as can be seen in the raw spectra of the thermal post-treatment, with increasing temperature the baseline of the spectra experiences a general increase in intensity, which becomes more apparent at lower wavenumbers. Even though the intensity of the bands remains unchanged, the rising baseline leads to the creation of false negative bands in the difference spectra. The origin of the baseline bending is being assigned to the accumulation of conduction electrons at higher temperatures in some TiO_2 samples.[15]

The results of the CO_2 adsorption experiment conducted under illumination are shown in Figure 45(ii). The surface of the sample was much cleaner after the thermal pretreatment, as much less signals are apparent in the initial spectra (Figure A. 2(ii)). This might be the reason for the overall higher intensity of the bands of the difference spectra, when compared to the spectra in Figure 45(i). Features at 1670 and 1432 are assigned to ν_a(CO). Together with the corresponding weak feature of δ(COH) at 1219 cm^{-1}, these three signals indicate the formation of monodentate bicarbonates. As these bands disappear during purging of the reaction cell with Ar, this undermines the assumption of the weakly bound species. Features at 1625, 1505 and 1248 cm^{-1} can be assigned to the formation of bidentate bicarbonates. A feature at 1584 cm^{-1} (being part of a broad band around 1575 cm^{-1}) as well as the corresponding feature at 1378 cm^{-1} are characteristic for ν_a(CO) in monodentate carbonates. Features in the same region positioned at 1575 cm^{-1} and 1360 cm^{-1} can be assigned to ν_a(CO) in adsorbed carboxylates[56] or bidentate carbonates[62]. Due to the broad range covered in the spectrum by latter feature it can be further assumed to mask features around 1550 and 1370 cm^{-1} indicating ν_a(CO) in adsorbed formate species. Further, when investigating the spectrum between 2800 and 3000 cm^{-1} two weak features are apparent at around 2960 and 2872 cm^{-1} which are characteristic for stretching of CH-groups in adsorbed formates.[76,78] Therefore, formation of adsorbed formate species is suggested. Due to the mostly negative bands in the spectra of thermal post-treatment shown in Figure 45(iv) it is assumed that all adsorbed carbonates and formate species are being desorbed or decomposed. The negative band at 1269 cm^{-1} is created due to the baseline bending of the spectra at higher temperatures rather than due to a disappearing species, as was described earlier.

CO_2 adsorption experiments have been conducted on a core shell catalyst containing a TiO_2 core and an organic shell. Detailed information on the material can be found elsewhere[144]. Table 8 sums up vibrational features, the respective positions in the DRIFT spectrum as well as the assignment to corresponding carbon containing species formed due to adsorption of CO_2 on m-TiO_2 sample. Reasons for particular assignments are based on the discussion of previous measurement on anatase and P25 and are thus briefly outlined in the following.

Table 8: Summary vibrational modes and identified species formed during adsorption of CO_2 on m-TiO_2 material. Corresponding wavenumbers are given in [cm^{-1}].

vibrational mode	formate	monodentate carbonate	bidentate carbonate	monodentate bicarbonate	bidentate bicarbonate
Dark					
ν_a(CO)	-	1592 1378	1575 1360	1671 1421	1624 1497
δ(COH)	-	-	-	1248	1218
Light					
ν_s(CH)	2960 2872	-	-	-	-
ν_a(CO)	-	-	1550 1360	1671 1421	1624 1497
δ(COH)	-	-	-	1248	1218

Figure 46(i) shows the results of DRIFTS measurement of the CO_2 adsorption and desorption in the dark on thermally pretreated m-TiO_2 sample. Three main features behaving similarly throughout the experiment can be identified at 1671, 1421 and 1248 cm^{-1}. They are assigned to ν_a(CO) and δ(COH) in weakly bound monodentate bicarbonates[62,76,77], which are formed when CO_2 is present in the atmosphere, however, quickly desorbed during the purging step already. As the features at 1624 and 1218 cm^{-1} are present during the whole experiment, these are assigned to ν_a(CO) and δ(COH) of strongly bound bidentate bicarbonates. The less intense signal at 1497 cm^{-1} required to solidify this assumption is presumably part of the broad band appearing as a shoulder

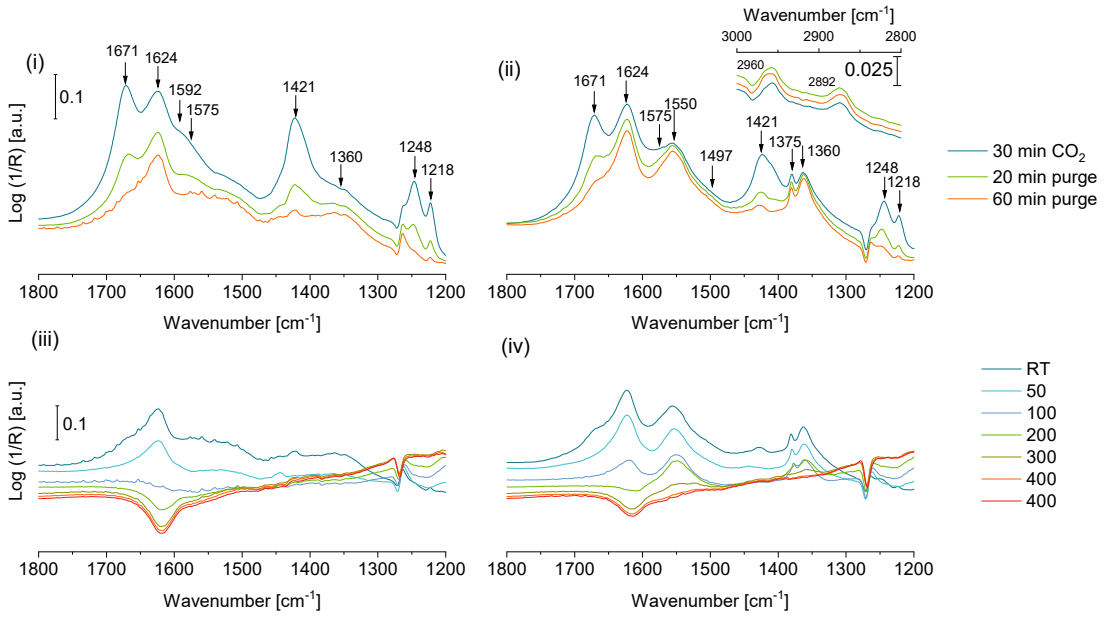

Figure 46: Difference DRIFT spectra recorded during the CO_2 adsorption experiment in dark(i) and under illumination(ii) as well as the subsequent thermal treatment((iii), (iv)) of the m-TiO_2 sample. The last spectra of the top depictions (red) are the first spectra of the bottom depictions (dark teal).

at 1530 cm^{-1} and becoming more apparent in the end of the purging step. The broad shoulder at 1592 cm^{-1}, which disappears when CO_2 is removed from the atmosphere is assigned ν_a(CO) in weakly bound monodentate carbonate species.[58] The intensity of corresponding signal at around 1378 cm^{-1} was calculated to be about 15 times weaker and is therefore presumably not clearly visible, but is probably contributing to the broad band between 1300 and 1450 cm^{-1}. Another feature which might be part of this broad band is a signal at 1360 cm^{-1}. Together with a corresponding feature at 1575 cm^{-1} it can be assigned to carboxylates[56] or bidentate carbonates.[62] As both signals are not clearly visible, the presence of this species is only a suggestion. During the thermal post-treatment most on the formed carbonate species are desorbed or decomposed, as the corresponding spectra shown in Figure 46(iii) feature only negative bands. Furthermore, band bending towards lower wavenumbers is observed, which again is attributed to the accumulation of conductive electrons at higher temperatures.

The results of the DRIFTS measurement during the light assisted CO_2 adsorption experiment are shown in Figure 46(ii). Similar to the dark experiment characteristic features for the formation of weakly adsorbed monodentate bicarbonates (1671, 1421 cm^{-1} for ν_a(CO) and 1248 cm^{-1} for δ(COH)) as well as strongly bound bidentate bicarbonates (1624, 1497 cm^{-1} for ν_a(CO) and 1218 cm^{-1} for δ(COH)) are clearly visible. Additionally, features at 1550 and 1360 cm^{-1} are much more apparent compared to the experiment in the dark and are assigned to an increased formation of strongly bound bidentate carbonates. Furthermore, a rather sharp band appears at 1375 cm^{-1}, while a corresponding feature for an assignment to ν_a(CO) in formate species at 1550 cm^{-1} is presumably part of the broad band in this region. As weak bands at 2872 and 2960 cm^{-1} which are characteristic for ν_a(CH) are apparent as well, formation of adsorbed formate species is suggested.[76,78] During the subsequent thermal treatment negative features appear at the position mentioned above, indicating the desorption and decomposition of all surface species.

In Table 9 a summary of identified surface species formed during CO_2 adsorption experiment is shown. Thermal pretreatment at 675 K is found to be not sufficient for cleaning the surface of anatase samples, as temperature-stable surface species were still present during the adsorption experiment. These are suggested to participate in formation of other adsorbed species as the respective characteristic signals disappear when additional CO_2 is introduced into the reaction chamber, and reappear as soon as CO_2 is purged out or the sample is thermally treated at 675 K. Nevertheless, on anatase CO_2 was found to form different adsorbed carbonate species such as carboxylates, monodentate carbonates and bicarbonates. When the same experiment is conducted under illumination with UV-light no carboxylates are formed, while monodentate carbonates and less stable monodentate bicarbonates can be identified similarly to the dark experiment. Bidentate

bicarbonates are formed as well, however, feature stronger binding energy, as they are being desorbed only during thermal post-treatment of the sample. On P25 CO_2 predominantly forms different kinds of carbonates such as monodentate, bidentate and free carbonates. Further weakly bound monodentate bicarbonates can be identified. When during UV-illumination CO_2 is introduced to the reaction chamber, monodentate and bidentate carbonates are being formed as well. Further, not only monodentate bicarbonates, but also bidentate bicarbonates as well as formate species are formed. On m-TiO_2 material CO_2 was found to form monodentate and bidentate carbonates, as well as weakly bound monodentate bicarbonates and strongly bound bidentate bicarbonates. When UV-illumination was implemented during the CO_2 adsorption, monodentate and strongly bound bicarbonate were formed. While no monodentate carbonates were identified, a higher degree of bidentate carbonate formation was detected. Additionally, formate species were identified.

It is known that especially bicarbonates are formed due adsorption of CO_2 molecules through one of the oxygen atoms on sites such as interstitial Ti atoms or oxygen vacancies leading to an activation of CO_2 and followed by a subsequent interaction with pre-adsorbed surface hydroxyl groups.[147,148] Assuming UV-Illumination affects TiO_2 samples in a similar manner as ZnO, it is suggested that oxygen desorption is favored due to the chain of events postulated earlier: exciton formation due to illumination with light in the self-absorbing range of the material leads to charge carrier separation and further migration of excited electrons to the surface region, where these contribute to desorption of oxygen and therefore are trapped in oxygen deficient sites.

Moreover, desorption of oxygen results in an increased number of poorly coordinated Ti atoms which are Lewis acidic sites. This would explain the increased formation probability and stability of bidentate bicarbonates on anatase as well as anatase-based m-TiO_2 sample. From light driven CO_2 conversion experiments m-TiO_2 as well as P25 are known to be good methane production catalysts. Identification of formate species during illuminated CO_2 adsorption experiments might give a hint on the reaction mechanism of the CO_2 conversion. Since formation of different bicarbonate species is assumed to take place due to adsorption of CO_2 in proximity to hydroxyl groups, the interaction between both is assumed to be activated through light thus being the previous step to formate formation. However, one must be cautious as the carbon source utilized for the formation of formates is not clearly identified. It is possible that previously existing residual carbonate species are transformed, while gas phase CO_2 is being adsorbed but not converted. As was shown by Mul *et al.*[81] during $^{13}CO_2$ conversion experiments, carbon containing residues are predominantly involved in photocatalytic reactions, rather than $^{13}CO_2$ provided in the gas phase. The results obtained here highlight the necessity to verify the observations shown in the work at

Table 9: summary of identification of formed adsorption species on different TiO_2 materials upon exposure of CO_2 in dark and under illumination

	Dark	Light
anatase	- monodentate carbonates - monodentate bicarbonates - bidentate bicarbonate - carboxylate	- monodentate carbonates - monodentate bicarbonates - stable (bridging/chelating) bidentate bicarbonate
p25	- monodentate carbonate - monodentate bicarbonate - (bridging) bidentate carbonates - free carbonates	- monodentate carbonates - monodentate bicarbonates - bidentate carbonates (or carboxylates) - bidentate bicarbonates - formate
m-TiO_2	- monodentate carbonates - monodentate bicarbonates - bidentate carbonates (or carboxylate) - strongly bound bidentate bicarbonates	- monodentate bicarbonates - bidentate carbonates - strongly bound bidentate bicarbonates - formate

hand by similar $^{13}CO_2$ based experiments but may also have a strong impact on the viability of production rates reported for photoreduction catalysts throughout the last decades. Especially catalytic performance of catalysts prepared with carbon containing precursors must be questioned critically.

On the other hand, interaction of CO_2 through the C-atom with Lewis basic centers results in formation of surface carbonates.[58] As on m-TiO_2 the relative amount of carbonate formation during illumination is noticeably higher than in the dark, an overall higher basicity of the surface oxygen centers is assumed. This, however, contradicts the suggestion of light-assisted oxygen desorption. Tkalich *et al.* reported at least three different oxygen surface species being desorbed on ZnO during illumination with UV-light[116,117], which to some extent may also be true for TiO_2. Assuming light-assisted desorption of some surface oxygen species or increasing the Lewis basic character of others may be a possible explanation for the observed events.

3.9 Influence of Illumination on desorption of adsorbates on $Ce_xZr_{1-x}O_2$

The viability of light assisted desorption was investigated on a $Ce_xZr_{1-x}O_2$ sample.[149] When stored in air the material needs to undergo a 20 h regeneration procedure at 300 °C due to strong CO_2 adsorption capabilities of about 90 $\mu molg^{-1}$ and thus slow desorption of surface adsorbates. This

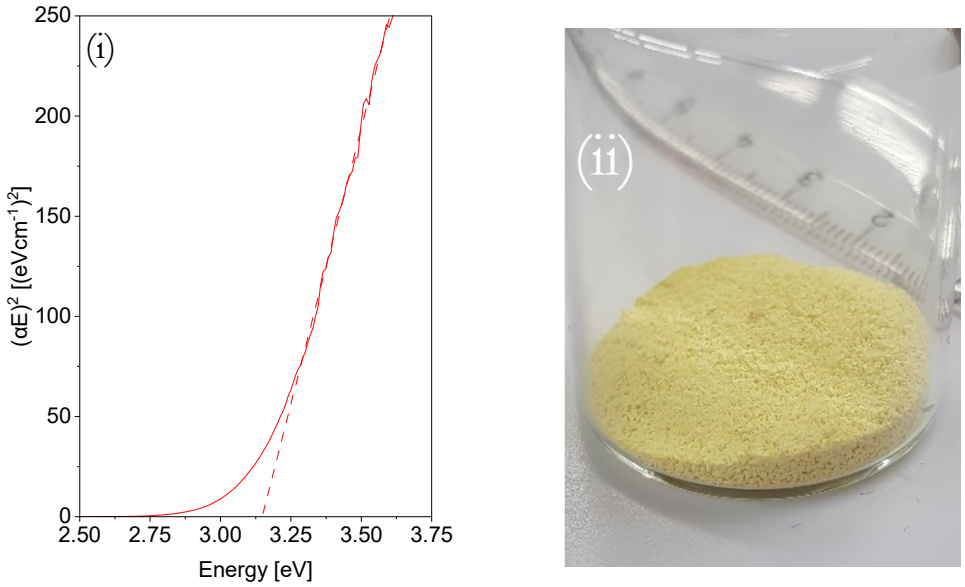

Figure 47: (i) Graphical determination of the band gap value from measured DR-UV/Vis-spectra and (ii) a photograph of the $Ce_xZr_{1-x}O_2$ sample.

property is of high interest for CO_2 capture from air, however, the regeneration procedure needs to be improved. It was therefore of interest to investigate, whether illumination of the sample with UV or Visible light would result in desorption of adsorbed species and therefore reducing the need of high pretreatment temperatures as well as shorten the pretreatment duration.

Several initial tests have been conducted using the DRIFTS set-up equipped with the Harrick cell to get a first impression on the properties of the materials with respect to illumination and thermal treatment in inert atmosphere (Ar).

In the first test the sample was treated thermally according to the first step of the standard procedure explained in chapter 7.1.3.1, while additional illumination with light in the visible or UV range was applied. According to previous DRS measurements, the bandgap of the material was estimated at 3.14 eV (s. Figure 47(i)). However, as the sample shows an apparent yellow color(s. Figure 47(ii)), the spectral range of illumination utilized for light assisted experiments was set at 400-700 nm.

Figure 48 shows the calibrated mass traces of CO_2 in effluent gas stream recorded during the thermal treatment in the dark in comparison to illuminated thermal treatment. In both cases two peaks can be seen, indicating desorption of weakly bound carbonate species or CO_2 up to a temperature of 150 °C, followed by possibly decomposition of more strongly bound carbonates at around 300 °C. However, the second desorption step features a much lower height due to lower amount of strongly bound carbon containing species. The onset slope of the first desorption peak is in case of illuminated heating much steaper, which might be due to additional heating through

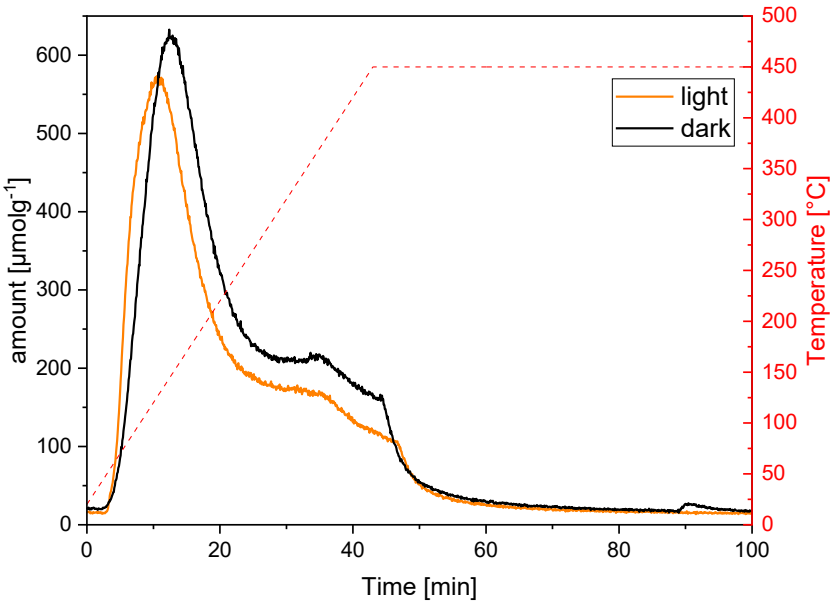

Figure 48: Weight normalized mass traces for CO_2 in the effluent stream recorded with the QMS during thermal treatment tests of $Ce_xZr_{1-x}O_2$ sample in the Harrick cell in Ar. (black) Thermal treatment in dark; (orange) illuminated thermal treatment with additional illumination (400-700 nm, 225 mWcm^{-2}).

the thermal radiation of the lamp. Apart from the overall lower amount desorbing from the illuminated sample during thermal treatment, there are no further differences in the shape of the mass traces apparent. Illumination seems not to influence the thermal desorption.

In the second test the sample was investigated as received without any thermal pretreatment, but initial purging of the reaction chamber with Ar while the Harrick cell was cooled by flowing tap water with a temperature of 15 °C. Subsequently, the sample was kept alternating under illumination and darkness for about 15 min, while first UV light in the range of 320-400 nm was applied and afterwards visible light in the range of 400-700 nm. The results of the effluent gas stream recorded by the QMS for the calibrated fractions of CO_2 and H_2O is shown in Figure 49 (i). Illumination with UV light leads to desorption of CO_2 as well as H_2O, while illumination with visible light has a similar but weaker effect. The lower desorption of adsorbates can be attributed to a limited amount of initially adsorbed species, of which some fraction is already desorbed during the first illumination step. As the temperature reading of the Watlow^{tm} heating control unit showed an increase in temperature up to 45 °C when the sample was illuminated, thermal radiation of the lamp needed to be excluded as the reason for the desorption processes. A second experiment with similar alternating condition was conducted, where in the first step visible light was applied, while in the second step (after 15 min of subsequent darkness) the sample holder was heated to about 45 °C and held to 15 min utilizing the Watlow^{tm} temperature control unit. With this it was attempted to replicate the increase of the temperature inside the cell, but without an illumination. As Figure 49 (ii) shows, significant amount of desorbed H_2O and CO_2 was recorded during the

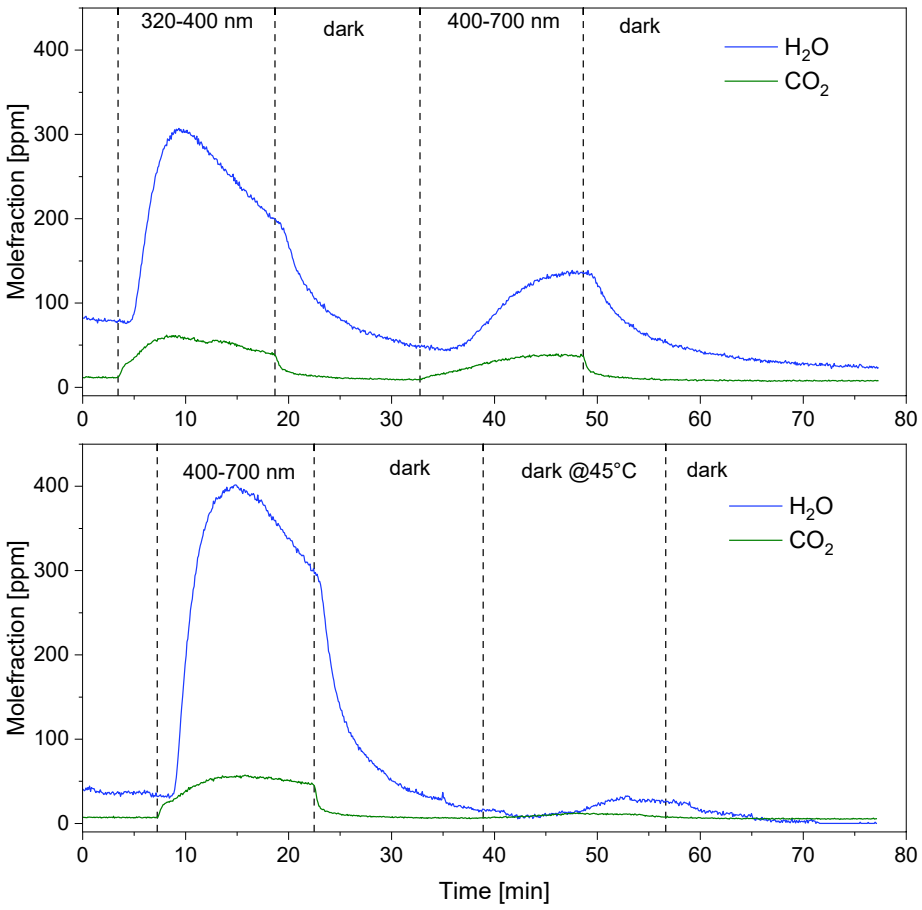

Figure 49: Mass traces for CO_2 and H_2O in the effluent stream recorded with the QMS during initial irradiation tests of untreated $Ce_xZr_{1-x}O_2$ sample in the Harrick cell.

illumination, while pure heating to 45 °C without light resulted in much weaker desorption. As discussed earlier, the temperature rise due to thermal radiation of the lamp is possibly much higher than indicated by the Watlow^{tm} control unit. Since the temperature sensor is positioned at the bottom of the Harrick cell, and the lamp points directly at the surface of the material, there is a certain distance covered by bulk metal of the sample cell between these two points. Due to strong thermal radiation of the lamp, slow increase of the temperature of the whole cell might result in a large difference of the temperature leading to a lower value provided by the thermal sensor, when compared to the temperature at the surface of the packed bed of the sample. Thus, in these experiments both thermal and irradiation assisted desorption is possible. However, an unambiguous assignment to what degree thermal radiation of the lamp contributes to the desorption process during the illumination experiment is not possible here.

In the interest of a direct comparison between illumination and thermally induced desorption a four-step experiment was designed, which is schematically depicted in Figure 50 and was performed on two samples of the same catalyst. In the first step the material was pretreated

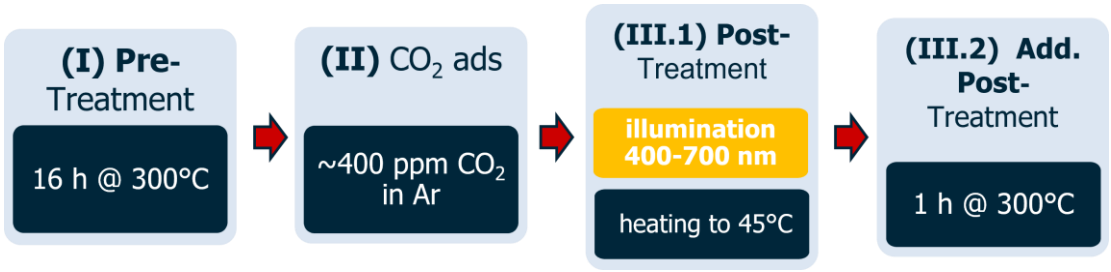

Figure 50: Schematic depiction of the four-step experiment for a direct comparison between illumination and thermally assisted desorption.

thermally at 300 °C in Ar for 16 h according to the standard regeneration procedure of the material.[149] After cooling down the sample to room temperature 400 ppm of CO_2 were added to the Ar flow for a duration of 30 min, followed by a subsequent purging of the reaction chamber with pure Ar for 2 h. The post-treatment of the material included two steps, where in the first step the sample was either heated to 45 °C for two hours or illuminated with light in the range of 400-700 nm (225 $mWcm^{-2}$). In the second step the sample was heated to 300 °C at a heating rate of 10 $Kmin^{-1}$ in Ar and kept at this temperature for 1 h.

Figure 51 shows the mass traces of CO_2, H_2O and O_2 recorded by the QMS during the thermal pretreatment in Ar. Similar to the results shown in Figure 48, the sample features a strong desorption maximum at around 150 °C, where large amounts of CO_2 and H_2O were detected. After about 2 h no CO_2 and H_2O were detected in the effluent gas stream for the rest of the experiment. After cooling down the sample to room temperature and providing CO_2 for a subsequent adsorption on the catalyst surface, both samples featured theoretically the same state. Results of the direct comparison between illumination and pure thermal treatment at 45 °C are shown in Figure 52(i). Both treatment methods result in an initial increase of desorbed CO_2. The amount of desorbed CO_2 during pure thermal treatment is significantly higher, than during irradiation, which

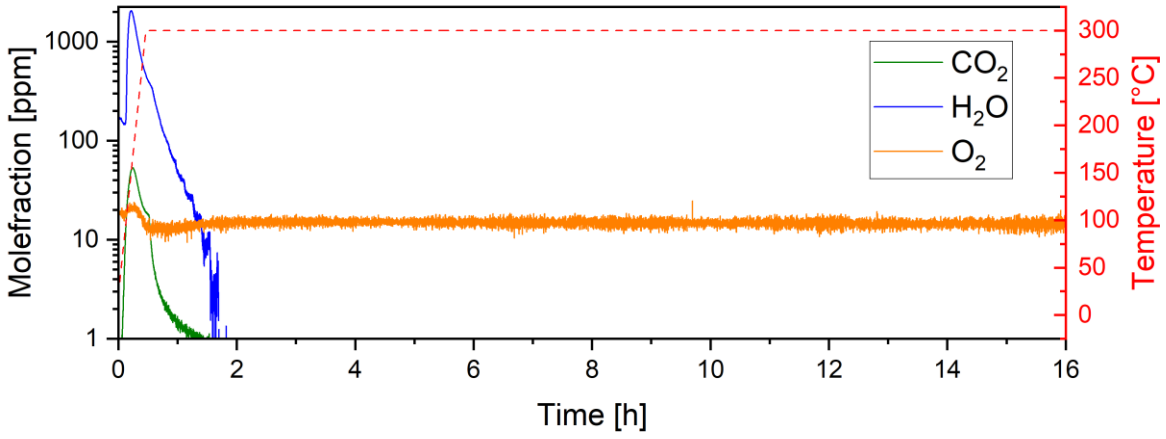

Figure 51: Mass traces of CO_2, H_2O and O_2 recorded by the QMS from the effluent gas stream of Ar during the thermal pre-treatment of the sample.

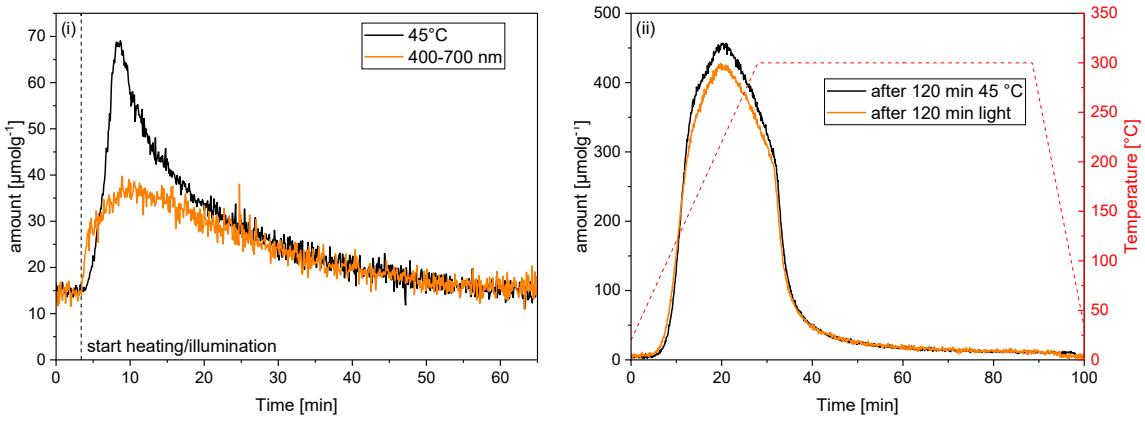

Figure 52: (i) Weight normalized mass traces of CO_2 recorded by the QMS from the effluent gas stream during the illumination with light (orange) of the spectral range 400-700 nm (225 mWcm^{-1}) and thermal treatment in Ar at 45 °C (black); (ii) Weight normalized mass traces of CO_2 recorded during final thermal post treatment after illumination of the pretreated sample with light (orange) or holding the sample at 45 °C for 2 h (black).

is contrary to the assumption that illumination leads to an increased desorption. Since irradiation inevitably leads to an increase in temperature inside the reaction chamber (and especially on the surface of the material) it is assumed that desorption of CO_2 is caused in both cases by increased temperature.

Mass traces of CO_2 recorded during the subsequent thermal post treatment at 300 °C Figure 52(ii) do not show any difference – neither in intensity nor in desorption profile shape, respectively. This indicates that the previous treatment with visible light or low heat do not result in desorption of different species, as it is the case for desorption processes reported on ZnO (s. Figure 13, p. 31) One can therefore conclude that irradiation of the sample with visible light does not lead to light driven desorption, but rather results in thermal driven desorption due to the high degree of thermal radiation of the lamp. This result points out the importance of control experiments for photocatalytic reactions. A blank reaction should be conducted in the dark but with addition of thermal energy equivalent to the thermal radiation of the lamp. This would reduce the probability of false assignment of apparently successful photocatalytic reactions to light driven origins, while not postulating "novel" and "unique" mechanisms.

4 Summary

The main aim of this work to investigate the influence of UV irradiation on the CO_2 adsorption capabilities of metal oxide-based materials succeeded partially. ZnO based materials with different morphologies were synthesized to expand the range of research and include the influence of the nanostructure on the CO_2 adsorption properties. Commercially available ZnO nanoparticle material was chosen as a benchmark material. While solid-state synthesis of a material with large crystal size, as well as hydrothermal synthesis of flakes and flowers was repeatedly successful, synthesis of rods succeeded only once and was not reproducible in numerous further attempts. Qualitative measurements by means of DRIFT spectroscopy were mostly not possible due to the "IR Blackening" effect occurring upon thermal treatment in reductive atmosphere or illumination of the sample. An in-depth search for explanation of the origin of the effect revealed a whole research field from middle of the 20th century in the former Soviet Union but seemingly forgotten among chemists in the western world. Research groups of former pioneers such as Terenin, Lisachenko or Solnitsyn evolved to a point, where modern results often require a background in theoretical solid-state physics for a full understanding. Nevertheless, contemporary experimental set-ups are utilized to confirm results, while providing even more details about processes and events. Therefore, the origins of changes of optical and electrical properties in ZnO due to irradiation with UV-light or thermal treatment in reductive atmosphere or vacuum, and their implications for adsorption processes were outlined in a comprehensive overview. Numerous literature sources show TPD experiments which identified at least three different oxygen species present on the surface of ZnO. Further, illumination with UV-light was reported to initiate desorption of oxygen or an equilibrium between desorption and adsorption in case of a static ^{18}O-rich atmosphere. Thermal and light induced desorption processes result in an accumulation of free electrons in the conduction band or slightly below it. This was found to be the main reason for increased conductivity in ZnO when illuminated or heated. A further excitation into or inside the conduction band during IR-light based experiments was assumed to lead to the IR-blackening effect. Nowadays, the theory of electron-phonon interactions is complementing this assumption. From luminescence experiments adsorption of electronegative gas phase molecules on the surface was assumed to create trap sites leading to quenching of fluorescence.

Quantitative investigations of CO_2 adsorption capabilities of ZnO materials were conducted by means of TPD measurements in the DRIFTS set-up equipped with a high temperature Harrick cell and a subsequent evaluation of effluent gas stream through a QMS. The amount of desorbed CO_2 was dependent on the nanostructure of the investigated material and resulted in the row: SSS<particles<flakes<flowers(<rods). Moreover, irradiation of thermally pretreated samples with UV-light while CO_2 was present in the atmosphere, was found to increase the amount of desorbed CO_2 during the subsequent TPD experiment in Ar. However, repeating the experiments in the custom built and flow optimized photo-TPD set-up did not confirm the results, as no significant difference between desorbed amount of CO_2 after adsorption under illumination and in the dark was found.

A thorough literature analysis in the research field of CO_2 adsorption by means of FTIR Spectroscopy was conducted. This resulted in a critical review of misconceptions around assignments of spectroscopic features to vibrational modes accumulated in recent decades.

Influence of UV illumination on CO_2 adsorption on different TiO_2 based materials was investigated qualitatively by means of DRIFTS. An anatase-based core-shell material prepared in a different work was compared to P25 and pure anatase. While on anatase illumination was found to cause formation of stronger carbonate and bicarbonate surface species, on P25 and m-TiO_2 additional formate species were formed. On the latter, increased number of bicarbonates due to interaction of CO_2 with pre-adsorbed hydroxyl groups is suggested to be the previous step of formate formation, while potentially leading to subsequent formation of methane or methanol. However, possibly predominant participation of residual carbonate species in photocatalytic reactions needs to be kept in mind and must be checked through adsorption experiments with $^{13}CO_2$ for a validation or disproval of suggested mechanisms.

Lastly the influence of illumination on desorption of CO_2 from $Ce_xZr_{1-x}O_2$ material was investigated. As substitution of thermal energy needed for thermal regeneration process of the material was evaluate, the viability of photo activation of desorption processes was evaluated. Unfortunately, irradiation with visible light does not lead to an increased desorption of CO_2. More importantly, the thermal radiation of the irradiation source was found to contribute to the desorption. This points out the need of thermal blank experiments without illumination in order to confirm the origin of photoreactions being the photo-induced effects and not thermal conversion.

5 Outlook

The work at hand gives an overview over different scientific fields and topics and thus offers a range of possible directions for further in-depth research. Origins of "IR-Blackening" can be further investigated utilizing a set-up combining pulsed nsec laser with a step-scan method similar to the experiments conducted by Ben-Refael et al.[136] With that temporal behavior of species, sites and excited states can be outlined, while providing insight into post-excitation processes in a semiconductor material.

In order to pursue the aim of utilization of ZnO as carbon capture material, with potential to direct (photo)catalytic conversion, it might be interesting to implement large surface area supporting material. First steps in this direction have been conducted, including trying different synthesis methods for mesoporous silica such as MCM48.[150-153] Due to its high surface area, but also transparency towards UV-light, it is a good contender for the given task. Moreover, several techniques for deposition of ZnO were investigated. While some resulted in an implementation of Zn in the mesoporous wall structure of SiO_2,[45,150,153,154] other showed formation of isolated ZnO particles.[155]

As ZnO was found to feature accumulation of electrons in conduction band upon illumination (and sometimes already upon thermal pretreatment in reductive atmosphere), doping of nanostructured materials with elements like Au offers a possibility for more directed utilization of excess electrons. As synthesis pathways are well known from literature, Au was successfully deposited on different nanoshaped ZnO materials, such as flakes, rods and spheres. First photocatalytic CO_2 conversion experiments, however, showed poor activity of the material. Further catalyst and reaction design are needed in order to (dis)prove the viability of the concept.

.

6 List of References

1 M. Calvin. in *Solar Energy: Chemical Conversion and Storage*, (eds Richard R Hautala, R Bruce King, & Charles Kutal), p. 1-30 (The Human Press, **1979**)

2 R. B. Bacastow, C. D. Keeling. in *Workshop on the Global Effects of Carbon Dioxide from Fossil Fuels* Vol. 1 (eds William P. Elliot & Lester Machta) 72-90 (Office of Health and Enviromental Research, Miami Beach, Florida, USA, **1979**)

3 *Global Climate Change*, <https://climate.nasa.gov/vital-signs/carbon-dioxide/> (**2020**)

4 D. Tong, Q. Zhang, Y. Zheng, K. Caldeira, C. Shearer, C. Hong, Y. Qin, S. J. Davis, *Nature*, **2019**, *572*, p. 373-377

5 G. Ciamician, *Science*, **1912**, *36*, p. 385-394

6 G. A. Frick, *Cactus and Succulent Journal of the Cactus and Succulent Society of America*, **1938**, *10*, p. 60-61

7 J. R. Bolton. in *Solar Energy: Chemical Conversion and Storage*, (eds Richard R. Hautala, R. Bruce King, & Charles Kutal), p. 31-50 (Humana Press, **1979**)

8 D. O. Hall. in *Solar Power And Fuels*, (ed James R. Bolton), p. 27-52 (Elsevier, **1977**)

9 T. R. Schneider, *Energy Conversion*, **1973**, *13*, p. 77-84

10 J. R. Bolton, *Solar Energy*, **1978**, *20*, p. 181-183

11 A. Fujishima, K. Honda, *Nature*, **1972**, *238*, p. 37-38

12 L. Liu, H. Zhao, J. M. Andino, Y. Li, *ACS Catalysis*, **2012**, *2*, p. 1817-1828

13 S. N. Habisreutinger, L. Schmidt-Mende, J. K. Stolarczyk, *Angewandte Chemie International Edition*, **2013**, *52*, p. 7372-7408

14 Y. He, Y. Wang, L. Zhang, B. Teng, M. Fan, *Applied Catalysis B: Environmental*, **2015**, *168-169*, p. 1-8

15 A. Lüken, M. Muhler, J. Strunk, *Physical Chemistry Chemical Physics*, **2015**, *17*, p. 10391-10397

16 S. Zhu, D. Wang, *Advanced Energy Materials*, **2017**, *7*, p. 1700841

17 A. Gankanda, D. M. Cwiertny, C. H. Grassian, *The journal of Physical Chemistry C*, **2016**, *102*, p. 19195-19203

18 I. B. Freeman. Manufacture of zinc-white. Great Britain patent **1879**

19 I. B. Freeman, *J. Am. Chem. Soc.*, **1881**, *3*, p. 76

20 C. Klingshirn, M. Grundmann, A. Hoffmann, B. Meyer, A. Waag, *Physik Journal*, **2006**, *5*, p. 33-39

21 V. N. Filimonov, Y. D. Pimenov, *Izvestiya Akademii Nauk SSSR*, **1970**, p. 730-736

22 C. Klingshirn, A. Waag, A. Hoffmann, J. Geurts. *Zinc Oxide: From Fundamental Properties towards Novel Applications*, 1 edn, (Springer-Verlag Berlin Heidelberg, **2010**)

23 A. Das, D.-Y. Wang, A. Leuteritz, K. Subramaniam, H. C. Greenwell, U. Wagenknecht, G. Heinrich, *Journal of Materials Chemistry*, **2011**, *21*, p. 7194-7200

24 M. Przybyszewska, M. Zaborski, *Polymer Letters*, **2009**, *3*, p. 542-552

25 G. J. Fosmire, *Am J Clin Nutr*, **1990**, *51*, p. 225-227

26 G. Heideman, R. N. Datta, J. W. M. Noordermeer, B. v. Baarle, *Journal of Applied Polymer Science*, **2005**, *95*, p. 1388-1404

27 S. Thomas, E. Mathew, C. Marykutty, *Journal of Applied Polymer Science*, **2012**, *124*, p. 3009-3107

28 D. Mora-Fonz, T. Lazauskas, M. R. Farrow, C. R. A. Catlow, S. M. Woodley, A. A. Sokol, *Chemistry of Materials*, **2017**, *29*, p. 5306-5320
29 K. M. Lee, C. W. Lai, K. S. Ngai, J. C. Juan, *Water Research*, **2016**, *88*, p. 428-448
30 P. W. Atkins, J. Paula. *Physikalische Chemie*, 5 edn, (Wiley-VCH, **2013**)
31 G. Czycholl. *Theoretische Festkörperphysik Band 1, Grundlagen: Phononen und Elektronen in Kristallen*, 4 edn, (Springer Spektrum, **2016**)
32 V. Ryabchuk, *International Journal of Photoenergy*, **2004**, *6*, p. 582750
33 R. Xu. *X-ray thermal diffuse scattering and its studies of lattice dynamics*, Ph.D. thesis, University of Illinois at Urbana-Champaign, **2011**
34 B. Dawson, W. Cochran, *Proceedings of the Royal Society of London. Series A. Mathematical and Physical Sciences*, **1967**, *298*, p. 255-263
35 S. L. Mair, Z. Barnea, *Acta Crystallographica Section A*, **1975**, *31*, p. 201-207
36 K. Kihara, G. Donnay, *The Canadian Mineralogist*, **1985**, *23*, p. 647-654
37 S. Hayashi, N. Nakamori, H. Kanamori, Y. Yodogawa, K. Yamamoto, *Surface Science*, **1979**, *86*, p. 665-671
38 W. Doerffler, K. Hauffe, *Journal of Catalysis*, **1963**, *3*, p. 156-170
39 P. Amigues, S. J. Teichner, **1966**, p. 362-379
40 A. T. B. Jack W. London, *Journal of Catalysis*, **1973**, p. 32-40
41 H. Wilmer, M. Kurtz, K. V. Klementiev, O. P. Tkachenko, W. Grünert, O. Hinrichsen, A. Birkner, S. Rabe, K. Merz, M. Driess, C. Wöll, M. Muhler, *Physical Chemistry Chemical Physics*, **2003**, *5*, p. 4736-4742
42 M. Kurtz, N. Bauer, H. Wilmer, O. Hinrichsen, M. Muhler, *Chemical Engineering & Technology*, **2004**, *27*, p. 1146-1150
43 M. Kurtz, N. Bauer, C. Büscher, H. Wilmer, O. Hinrichsen, R. Becker, S. Rabe, K. Merz, M. Driess, R. A. Fischer, M. Muhler, *Catalysis Letters*, **2004**, *92*, p. 49-52
44 M. Kurtz, J. Strunk, O. Hinrichsen, M. Muhler, K. Fink, B. Meyer, C. Wöll, *Angewandte Chemie International Edition*, **2005**, *44*, p. 2790-2794
45 M. W. E. van den Berg, S. Polarz, O. P. Tkachenko, K. V. Klementiev, M. Bandyopadhyay, L. Khodeir, H. Gies, M. Muhler, W. Gruenert, *Journal of Catalysis*, **2006**, *241*, p. 446-455
46 R. Naumann d'Alnoncourt, X. Xia, J. Strunk, E. Löffler, O. Hinrichsen, M. Muhler, *Physical Chemistry Chemical Physics*, **2006**, *8*, p. 1525-1538
47 S. P. M. W. E. van der Berg, O. P. Tkechenko, K. Kähler, M. Muhler, W. Grünert, *Catalysis Letters*, **2008**, *128*, p. 49-56
48 J. Strunk, K. Kähler, X. Xia, M. Comotti, F. Schüth, T. Reinecke, M. Muhler, *Applied Catalysis A: General*, **2009**, *359*, p. 121-128
49 I. M. Hegazy, R. A. Geioushy, S. M. El-Sheikh, A. Shawky, S. El-Sherbiny, A.-H. T. Kandil, *Journal of Environmental Chemical Engineering*, **2020**, *8*, p. 103887
50 M. Cao, F. Wang, J. Zhu, X. Zhang, Y. Qin, L. Wang, *Materials Letters*, **2017**, *192*, p. 1-4
51 L.-Y. Lin, S. Kavadiya, B. B. Karakocak, Y. Nie, R. Raliya, S. T. Wang, M. Y. Berezin, P. Biswas, *Applied Catalysis B: Environmental*, **2018**, *230*, p. 36-48
52 Z.-j. Wang, H. Song, H. Pang, Y. Ning, T. D. Dao, Z. Wang, H. Chen, Y. Weng, Q. Fu, T. Nagao, Y. Fang, J. Ye, *Applied Catalysis B: Environmental*, **2019**, *250*, p. 10-16
53 J. H. Lunsford, J. P. Jayne, *American Chemical Society*, **1965**, *7*, p. 2182-2184
54 H. Deng, F. Xu, B. Cheng, J. Yu, W. Ho, *Nanoscale*, **2020**, *12*, p. 7206-7213
55 K. Nakamoto, J. Fujita, S. Tanaka, M. Kobayashi, *Journal of the American Chemical Society*, **1957**, *79*, p. 4904-4908
56 A. M. Turek, I. E. Wachs, E. DeCanio, *The Journal of Physical Chemistry*, **1992**, *96*, p. 5000-5007
57 G. Busca, V. Lorenzelli, *Materials Chemistry*, **1982**, *7*, p. 89-126
58 L. Mino, G. Spoto, A. M. Ferrari, *The Journal of Physical Chemistry C*, **2014**, *118*, p. 25016-25026

59 K. Bhattacharyya, A. Danon, B. K.Vijayan, K. A. Gray, P. C. Stair, E. Weitz, *The Journal of Physical Chemistry C*, **2013**, *117*, p. 12661-12678

60 G. Martra, *Applied Catalysis A: General*, **2000**, *200*, p. 275-285

61 L. F. Liao, C. F. Lien, D. L. Shieh, M. T. Chen, J. L. Lin, *The Journal of Physical Chemistry B*, **2002**, *106*, p. 11240-11245

62 J. Baltrusaitis, J. Schuttlefield, E. Zeitler, V. H. Grassian, *Chemical Engineering Journal*, **2011**, *170*, p. 471-481

63 J. E. J. Rasko, F. Solymosi, *The Journal of Physical Chemistry*, **1994**, *98*, p. 7147-7152

64 B. Xu, A. Hirsch, L. Kronik, Kristin M. Poduska, *RSC Advances*, **2018**, *8*, p. 33985-33992

65 R. Shendrik, E. Kaneva, T. Radomskaya, I. Sharygin, A. Marfin, *Crystals*, **2021**, *11*, p. 280

66 K. H. Hellwege, W. Lesch, M. Plihal, G. Schaack, *Zeitschrift für Physik A Hadrons and nuclei*, **1970**, *232*, p. 61-86

67 M. P. Andersson, C. P. Hem, L. N. Schultz, J. W. Nielsen, C. S. Pedersen, K. K. Sand, D. V. Okhrimenko, A. Johnsson, S. L. S. Stipp, *The Journal of Physical Chemistry A*, **2014**, *118*, p. 10720-10729

68 V. Orofino, A. Blanco, S. Fonti, R. Proce, A. Rotundi, *Planetary and Space Science*, **1998**, *46*, p. 1659-1669

69 R. Ruppin, R. Englman, *Reports on Progress in Physics*, **1970**, *33*, p. 149-196

70 N. V. Chukanov, I. V. Pekov, L. V. Olysych, N. V. Zubkova, M. F. Vigasina, *The Canadian Mineralogist*, **2011**, *49*, p. 1151-1164

71 L. Valenzano, Y. Noël, R. Orlando, C. M. Zicovich-Wilson, M. Ferrero, R. Dovesi, *Theoretical Chemistry Accounts*, **2007**, *117*, p. 991-1000

72 J. Bohr, R. A. Wogelius, P. M. Morris, S. L. S. Stipp, *Geochimica et Cosmochimica Acta*, **2010**, *74*, p. 5985-5999

73 C. J. Keturakis, F. Ni, M. Spicer, M. G. Beaver, H. S. Caram, I. E. Wachs, *ChemSusChem*, **2014**, *7*, p. 3459-3466

74 S. J. Hug, D. Bahnemann, *Journal of Electron Spectroscopy and Related Phenomena*, **2006**, *150*, p. 208-219

75 W. Su, J. Zhang, Z. Feng, T. Chen, P. Ying, C. Li, *The Journal of Physical Chemistry C*, **2008**, *112*, p. 7710-7716

76 K. K. Bando, K. Sayama, H. Kusama, K. Okabe, H. Arakawa, *Applied Catalysis A-general*, **1997**, *165*, p. 391-409

77 W. Wu, K. Bhattacharyya, K. Gray, E. Weitz, *The Journal of Physical Chemistry C*, **2013**, *117*, p. 20643-20655

78 G. Y. Popova, T. V. Andrushkevich, Y. A. Chesalov, E. S. Stoyanov, *Kinetics and Catalysis*, **2000**, *41*, p. 805-811

79 U. Tumuluri, J. D. Howe, W. P. Mounfield, M. Li, M. Chi, Z. D. Hood, K. S. Walton, D. S. Sholl, S. Dai, Z. Wu, *ACS Sustainable Chemistry & Engineering*, **2017**, *5*, p. 9295-9306

80 D. L. Bernitt, K. O. Hartman, I. C. Hisatsune, *The Journal of Chemical Physics*, **1965**, *42*, p. 3553-3558

81 C.-C. Yang, Y.-H. Yu, B. van der Linden, J. C. S. Wu, G. Mul, *Journal of the American Chemical Society*, **2010**, *132*, p. 8398-8406

82 K. O. Hartman, I. C. Hisatsune, *The Journal of Chemical Physics*, **1966**, *44*, p. 1913-1918

83 A. J. Wolfe. *Competing with the Sovjets: science, technology, and the state in Cold War America*, (Johns Hopkins University, **2013**)

84 I. K. Akopyan, M. E. Labzovskaya, A. A. Lisachenko, B. V. Novikov, A. Y. Serov, V. V. Titov, N. G. Filosofov, *Physics of the Solid State*, **2016**, *58*, p. 1767-1771

85 V. V. Titov, A. A. Lisachenko, I. K. Akopyan, M. E. Labzowskaya, B. V. Novikov, *Journal of Luminescence*, **2018**, *195*, p. 153-158

86 A. A. Lisachenko, *Journal of Photochemistry and Photobiology A: Chemistry*, **2018**, *354*, p. 47-60

87 I. K. Akopyan, M. E. Labzovskaya, B. V. Novikov, A. A. Lisachenko, A. Y. Serov, N. G. Filosofov, *Physics of the Solid State*, **2018**, *60*, p. 352-356
88 V. V. Titov, A. A. Lisachenko, M. E. Labzovskaya, I. K. Akopyan, B. V. Novikov, *The Journal of Physical Chemistry C*, **2019**, *123*, p. 27399-27405
89 V. V. Titov, A. A. Lisachenko, I. K. Akopyan, M. E. Labzovskaya, B. V. Novikov, *Physics of the Solid State*, **2019**, *61*, p. 2134-2138
90 V. V. Titov, A. A. Lisachenko, *Kinetics and Catalysis*, **2021**, *62*, p. 68-73
91 A. A. Lisachenko, *Physica B: Condensed Matter*, **2009**, *404*, p. 4842-4845
92 J. A. D. D. G. Rethwisch, *Langmuir*, **1985**, p. 73-79
93 E. Mollwo, F. Stöckmann, *Annalen der Physik*, **1948**, p. 240-254
94 E. Mollwo, F. Stöckmann, *Annalen der Physik*, **1948**, p. 223-229
95 E. Mollwo, *Annalen der Physik*, **1948**, p. 230-239
96 A. N. Terenin, *Vestnik Leningr. Univ.*, **1946**, *1*, p. 13-18
97 A. N. Terenin, *Journal of Physical Chemistry*, **1935**, *6*, p. 189
98 A. N. Terenin, *Problemy Kinetiki i Kataliza*, **1955**, *8*, p. 53-60
99 A. A. Lisachenko, F. I. Vilesov, *Kinetics and Catalysis*, **1972**, *13*, p. 420
100 A. A. Lisachenko, Y. F. Skornyakov, *Surface: Physics, Chemistry, Mechanics*, **1982**, *9*, p. 54-59
101 D. Eger, Y. Goldstein, A. Many, *RCA Review*, **1975**, *36*, p. 508
102 V. I. Veselovskij, *Journal of Physical Chemistry*, **1947**, *21*, p. 983-985
103 N. M. Beekmans, *Chem Soc Faraday Trans*, **1978**, *74*, p. 31
104 V. K. Miloslavskij, N. A. Kovalenko, *Optika i Spektroskopija*, **1958**, *5*, p. 614-617
105 V. N. Filimonov, *Optika i Spektroskopija*, **1958**, *5*, p. 709-710
106 S. Matsushita, T. Nakata, *J. Chem. Phys.* , **1960**, *982*, p. 982-987
107 S. Matsushita, T. Nakata, *J. Chem. Phys.*, **1962**, *36*, p. 665-669
108 T. Uematsu, H. Hashimoto, *Journal of Catalysis*, **1977**, *47*, p. 48-54
109 V. N. Kuznetsov, A. A. Lisachenko, *Journal of Applied Spectroscopy*, **1991**, *54*, p. 176-179
110 N. V. Vdovenko, V. N. Kuznetsov, A. A. Lisachenko, *Zhurnal Prikladnoi Spektroskopii*, **1991**, *54*, p. 627-632
111 L. L. Basov, V. A. Kotelnikov, A. A. Lisachenko, V. L. Rapoport, Y. P. Solnitsyn, *Uspehi Fotoniki*, **1969**, *1*, p. 78-111
112 F. Steinbach, R. Harborth, *Farraday Discussions Chem Soc.*, **1974**, *58*, p. 143-150
113 M. Grunze, W. Hirschwalf, E. Thull, *Thin Solid Films*, **1976**, *37*, p. 351-356
114 Y. Shapira, S. M. Cox, D. Lichtman, *Surface Science*, **1976**, *54*, p. 43-59
115 P. E. Valnev, *Nauch. Zhurnal Leningr. Gos. Univer.*, **1949**, *23*, p. 10
116 V. S. Tkalich, A. A. Lisachenko, A. O. Klimovskii, *Chim. Fiz.*, **1982**, *11*, p. 1525-1528
117 V. S. Tkalich, A. A. Lisachenko, A. O. Klimovskii, *React. Kintet. Catal. Lett.*, **1982**, *20*, p. 317-320
118 A. A. Lisachenko, I. F. Moiseienko, A. A. Glebovskij, *Tekhnicheskaja Fizika*, **1981**, *51*, p. 1721-1723
119 Y. Tokoro, T. Uchijima, Y. Yoneda, *Journal of Catalysis*, **1979**, *56*, p. 110-118
120 A. N. Terenin, Y. P. Solnitsyn, *Disc. Farad. Soc.* , **1959**, *28*, p. 28-37
121 A. A. Lisachenko, F. I. Vilesov, *Nauka: Zhurnal Tekhnicheskoi Fiziki*, **1968**, *39*, p. 590-592
122 Y. P. Solnitsyn, *Kinetika i kataliz*, **1965**, *6*, p. 250-257
123 A. N. Terenin, V. Gachkovskii, *Bull. acad. sci. U. R. S. S., Classe sci. math. nat., Ser. chim.*, **1936**, p. 805-831
124 A. N. Terenin, K. V. Tagancev, *Optika i Spektroskopija*, **1957**, *2*, p. 355-360
125 S. R. Morrison, *Advances in Catalysis*, **1955**, *7*, p. 255-301
126 A. A. Lisachenko, A. M. Aprelev, *Zhurnal Technicheskoj Fiziki*, **1995**, *21*, p. 9-14
127 *The Praying Mantis(TM) User's Manual*, (Harrick Scientific Products, INC., **2009**)
128 X. Xia, J. Strunk, W. Busser, R. Naumann d'Alnoncourt, M. Muhler, *The Journal of Physical Chemistry C*, **2008**, *112*, p. 10938-10942

129 X. Xia, J. Strunk, R. Naumann d'Alnoncourt, W. Busser, L. Khodeir, M. Muhler, *The Journal of Physical Chemistry C*, **2008**, *112*, p. 10931-10937

130 X. Xia, J. Strunk, S. Litvinov, M. Muhler, *The Journal of Physical Chemistry C*, **2007**, *111*, p. 6000-6008

131 H. Noei, H. Qiu, Y. Wang, E. Löffler, C. Wöll, M. Muhler, *Physical Chemistry Chemical Physics*, **2008**, *10*, p. 7092-7097

132 H. Noei, C. Wöll, M. Muhler, Y. Wang, *J. Phys. Chem.*, **2011**, *115*, p. 908-914

133 J. Buckeridge, C. R. A. Catlow, M. R. Farrow, A. J. Logsdail, D. O. Scanlon, T. W. Keal, P. Sherwood, S. M. Woodley, A. A. Sokol, A. Walsh, *Physical Review Materials*, **2018**, *2*, p. 054604

134 J.-H. Zhao, C.-J. Liu, Z.-H. Lv, *Optik*, **2016**, *127*, p. 1421-1423

135 B. Kortewille, I. E. Wachs, N. Cibura, O. Pfingsten, G. Bacher, M. Muhler, J. Strunk, *ChemCatChem*, **2018**, *10*, p. 2360-2364

136 A. Ben-Refael, I. Benisti, Y. Paz, *Catalysis Today*, **2020**, *340*, p. 97-105

137 N. Barsan, U. Weimar, *Journal of Electroceramics*, **2001**, *7*, p. 143-167

138 C. Klingshirn, R. Hauschild, J. Fallert, H. Kalt, *Physical Review B*, **2007**, *75*, p. 115203

139 *Drag-Effekt*, <https://www.spektrum.de/lexikon/physik/drag-effekt/3313> (**1998**)

140 A. F. Gibson, M. F. Kimmitt, A. C. Walker, *Applied Physics Letters*, **1970**, *17*, p. 75-77

141 A. A. Grinberg, *Soviet Physics JETP*, **1970**, *31*, p. 531-534

142 L. V. Lyashenko, Y. B. Gorokhovatskii, *Kinetika i kataliz*, **1968**, *9*, p. 1180-1182

143 J. Saussey, J.-C. Lavalley, C. Bovet, *Faraday Trans*, **1981**, *1*, p. 1457-1463

144 N. G. Moustakas, A. G. Kontos, V. Likodimos, F. Katsaros, N. Boukos, D. Tsoutsou, A. Dimoulas, G. E. Romanos, D. D. Dionysiou, P. Falaras, *Applied Catalysis B: Environmental*, **2013**, *130-131*, p. 14-24

145 G. Ramis, G. Busca, V. Lorenzelli, *Materials Chemistry and Physics*, **1991**, *29*, p. 425-435

146 A. Pougin, M. Dilla, J. Strunk, *Physical Chemistry Chemical Physics*, **2016**, *18*, p. 10809-10817

147 D. C. Sorescu, W. A. Al-Saidi, K. D. Jordan, *The Journal of Chemical Physics*, **2011**, *135*, p. 124701

148 D. C. Sorescu, J. Lee, W. A. Al-Saidi, K. D. Jordan, *The Journal of Chemical Physics*, **2011**, *134*, p. 104707

149 I. Prymak, O. Prymak, J. Wang, V. N. Kalevaru, A. Martin, U. Bentrup, S. Wohlrab, *ChemCatChem*, **2017**, *10*, p. 391-394

150 S. G. H. Gies, M Bandyopadhyay, W. Gruenert, O. P. Tkachenko, K. V. Klementiev, A. Birkner, *Microporous and Mesoporous materials*, **2003**, p. 31-42

151 D. L. C. D. matei, S. Mihai, *Digest Jornal of Nanomaterials and Biostructures*, **2016**, *11*, p. 271-276

152 M. Reichinger. *Poröse Silicate mit hierarchischer Porenstruktur: Synthese von mikro-/mesoporösen MCM41 und MCM48 Materialien aus zeolithischen Baueinheiten des MFI-Gerüststrukturtyps*, PhD thesis, Ruhr University Bochum, **2007**

153 H. R. Pouretedal, M. Ahmadi, *Iranian Journal of Catalysis*, **2013**, *3*, p. 149-155

154 L. Li, T. H. Sun, C. H. Shu, H. B. Zhang, *Journal of Hazardous Materials*, **2016**, *311*, p. 142-150

155 M. Bandyopadhyay, H. Gies, W. Gruenert, M. V. D. Berg, A. Birkner, *Advanced Materials Letters*, **2015**, *6*, p. 978-983

156 S. Brunauer, P. H. Emmett, E. Teller, *Journal of the American Chemical Society*, **1938**, *60*, p. 309-319

157 A. Sáenz-Trevizo, P. Amézaga-Madrid, P. Pizá-Ruiz, W. Antúnez-Flores, M. Miki-Yoshida, *Materials Research*, **2016**, *19*, p. 33-38

7 Appendix

7.1 Characterization methods

7.1.1 Powder X-ray diffraction

Due to the short wavelength of X-rays, which is in the order of magnitude of interatomic distances in crystalline materials, X-ray diffraction is utilized to gather information about three-dimensional structure of the crystal lattice, phases compositions, crystallite sizes and the degree of crystallinity of heterogeneous catalysts. Incident X-ray photons hitting the lattice from a certain direction and at a certain angle are elastically scattered on electron shells of lattice atoms. This results in diffraction of the incident beam while every lattice atom is a diffraction point. Parallel lattice planes reflect incoming X-rays combined, as there is only weak absorbance of the incident beam by the sample. A constructive interference of scattered photons occurs when the path length difference is an integer magnitude of the wavelength of the incident beam. This correlation is described in the following by Bragg's law

$$n\lambda = 2d_{hkl}sin(\Theta) \quad (9)$$

where n is the integer magnitude of the wavelength λ of the incident beam, d_{hkl} the distance between lattice planes and θ the angle between the incident beam and the diffraction lattice plane which is referred to as Bragg's angle.

While single crystal structures offer perfect conditions for X-ray diffraction measurements, in reality one more often deals with polycrystalline powders exposing different surface planes. Nevertheless, X-ray diffraction for powdered samples is viable, as these feature a statistical distribution of lattice planes. Thus, a certain fraction of the entirety of all particles of the sample has a proper orientation for the diffraction including a constructive interaction to occur. Since the angle of the incident beam is varied during the measurement, different planes are being hit resulting in numerous diffraction lines or reflexes in the diffraction pattern. Each of the reflexes refers to a well-defined lattice plane being denoted by the Miller Indices *h*, *k* and *l*. Nowadays Bragg's Law is

often written without magnitude n as it is integrated into the inter-plane distance d and is rather denoted for individual diffraction on planes *nh*, *nk* and *nl*.

Patterns recorded on single crystals with a size larger than 100 nm and perfect long range order feature sharp diffraction lines and are used as reference in order to identify and characterize the crystalline structure of the material at hand. For crystalline structures with a particle size smaller than 100 nm X-rays are more likely to be scattered leading to evanescent out of phase X-rays and thus and incomplete destructive interference with diffracted beams. As a consequence, diffraction lines of small particles are much broader. Luckily this opens the possibility for mean particle size determination, which is done mathematically by the Scherrer equation:

$$l = \frac{K \cdot \lambda}{\beta_{1/2} cos\theta_{hkl}} \quad (10)$$

Here the Scherrer constant K, the wavelength of the incident X-ray λ, the full width of the diffraction line at half maximum height $\beta_{1/2}$ at certain angle θ_{hkl} are utilized to calculate the effective crystallite size l. K is also referred to as the shape factor and depends on the particle shape, size, experimental resolution etc. – parameters of the system which are not always known. Nevertheless, in good approximation a value of 0.9 or 1 has proven to be viable. However, for sharp reflexes the width at half maximum is negligible small and cannot be utilized for the particle size determination. The integral of the breadth of the diffraction line is more suitable and is calculated by the ratio of area and maximum height of the diffraction signal. With this the Scherrer constant is being eliminated as well, which leads to the modified equation

$$\varepsilon_{\beta_{hkl}} = \frac{\lambda}{\beta_{hkl} cos\ \theta_{hkl}} \quad (11)$$

Here the integral-breadth size or the volume-weighted mean particle diameter $\varepsilon_{\beta_{hkl}}$ is calculated by the wavelength of the incident X-ray λ, the integral of the breadth β_{hkl} and the respective angle θ_{hkl} of the diffraction line.

All measurements have been conducted in the analytical department of Leibniz Institute for Catalysis in the *Panalytical X'Pert Pro* diffractometer utilizing the Bragg-Brentano-Geometry. The radiation source was modified by habrid-monochromator to obtain parallel-beam Cu-*K*-$a_{1,2}$-radiation. The device was equipped with an *X'celerator* Semiconductor detector. The evaluation of the measured data was performed in *Panalytical HighScore Plus* Software package using the latest Powder-Diffraction- and single crystal data sets (ICDD pdf2, ICSD).

7.1.2 Surface area determination according to Brunauer-Emmett-Teller (BET) theory

In heterogeneous catalysis the determination of the specific surface area is one of the basic characterization methods. As the overall surface area including the area of the outer shell and the inner pore system is investigated, information about theoretically available area, but also about pore size and volume of a possible porous material is gathered. For this purpose, non-specific, reversible adsorption, i.e. physisorption of mostly inert and non-polar gas molecules is utilized, where N_2 is the usual gas of choice. As the measurement includes observation of different gas pressures and relations, and the boiling temperature of N_2 is around 77 K, this is the temperature at which the measurement is usually conducted. In 1938 S. Brunauer, P. H. Emmett and E. Teller first introduced the method while outlining some assumption which are being made for its successful implementation.[156] While it takes into account multilayer adsorption, the coverage is assumed not to affect the very first adsorption layer so every adsorption site has the same adsorption enthalpy. Further, all gas molecules of one layer interact only with adjacent layers. Moreover, in the case of the vapor pressure p_v of the utilized gas is equal to the equilibrium pressure p_{eq}, the thickness of the multilayer is assumed to be infinite. During the measurement the pressure inside the chamber as well as amount or volume of the added gas are recorded and related to the initial pressure in a so-called adsorption isotherm. For the evaluation of the adsorption isotherm the linearized form of the BET equation is utilized, while considering the set assumptions:

(12)
$$\frac{p_{eq}}{V \cdot (p_v - p_{eq})} = \frac{1}{V_m + C} + \frac{(C-1)}{V_m + C} \cdot \frac{p_{eq}}{p_v}$$

Here V is the volume of the physiosorbed gas at the equilibrium pressure p_{eq} and vapor pressure p_v at the measurement temperature of the adsorbing molecule, while V_m denotes the gas phase volume in regard to monolayer adsorption. For the graphical evaluation of the recorded data $p_{eq}/V \cdot (p_v - p_{eq})$ is plotted against p_{eq}/p_v. Data points in the range of 0.05 to 0.35 for p_{eq}/p_v are used, as the linear section of the isotherm is usually positioned there. V_m as well as the constant C, which gives information about condensation and adsorption enthalpy of the used adsorbate, are being determined from the slope and the intercept of the BET plot and the y-axis, respectively. By utilization of the ideal gas law the monolayer amount n_m can be calculated from the gas phase volume V_m:

(13)
$$n_m = \frac{p \cdot V_m}{R \cdot T}$$

In the last step by utilizing the mass of the catalyst sample m_{cat}, the Avogadro constant N_A ($6.022 \cdot 10^{23}$ mol^{-1}) and the assumed space one N_2-molecule occupies, the specific surface area S_{BET} can be calculated according to BET by

$$S_{BET} = \frac{n_m N_A S_{N_2}}{m_{cat}} \quad (14)$$

All BET measurements have been conducted on *Anton Paar/Quantachrome* Nova 4200e sorption set-up. Prior to a sorption measurement each sample was treated thermally for 1 h at 395 K and subsequently 2 h at 495 K in vacuum. The sorption set-up relied on a static volumetric measurement method. Adsorbate gas (N_2) was dosed into the measurement cell and the physisorbed volume of N_2 was calculated from the drop in pressure.

7.1.3 UV/Vis Spectroscopy

UV/Vis spectroscopy relies on the interaction of the visible (Vis) or ultraviolet (UV) fraction of the electromagnetic radiation in order to investigate electronic properties of a material. When radiation interacts with matter different direct and indirect processes may occur. While reflection, scattering and absorbance are direct responses to incident light, processes like fluorescence, phosphorescence or photochemical reactions are indirect processes as these are a consequence of absorption of a photon. As the photon is considered a quant of light energy, absorption of a photon leads to an increase of the total potential energy of a material. It can be described as a sum of three different energies: (i) rotational, (ii) vibrational and (iii) electronic. Due to quantum mechanical principles the energy of a molecule is not a continuum but features quantized discrete levels. Rotational and vibrational energies feature lower energy levels and may interact with energetically low electromagnetic radiation such as IR radiation. Electronic energy levels require energetically higher radiation, which is mostly in the range of visible or UV light. Consequently, photons of UV and visible light may have sufficient amount of energy to cause transition of electrons inside a molecule to a higher orbital or level. As in metal and semiconductor material a large number of interatomic bonds is present, all molecular orbitals are summarized to bands resulting in valence and conduction bands. Absorption of energy sufficient for an electronic transition also results in weakening of the incident light beam which is reflected or transmitted through the sample (depending on the measurement method) and leaves the sample with lower energy. Thus, absorbance (or extinction) is expressed by a following function:

$$A = -log(I/I_0) \quad (15)$$

where I_0 and I represent the intensity of incident and transmitted light, respectively. Furthermore, the absorbance can be described by the Lambert-Beer law

(16) $$A = c \cdot d \cdot \varepsilon$$

with c being the concentration of the absorbing material, d the thickness of the sample or the cuvette (in case measurements of a liquid) and ε the spectral absorption coefficient. The latter is a material specific constant and may depend on the pH-value or solvent used during the measurement.

7.1.3.1 Diffuse reflectance UV/Vis spectroscopy

Diffuse reflectance UV/Vis spectroscopy (DRS) can be utilized to determine the electronic band gap of a semiconductor material. However, measurements of diffuse reflectance are not suitable for a direct quantification and determination of the bandgap of the material. The Lambert-Beer law describes the correlation between certain material factors like particle size, particle shape and packing density. As it is not possible to assure a reproducible preparation of the powdered sample, the Lambert-Beer law is not applicable here. The Kubelka Munk theory for the case of powdered, intensely scattering, absorbing and thick material offers a good approximation for the evaluation of measured reflection data and further calculations. The value of absorption coefficient α can be calculated for each wavelength by

(17) $$\alpha = \frac{S(1-R_\infty)^2}{2R_\infty}.$$

where S is the scattering coefficient and R_∞ the degree of reflection, measured in a sample of infinite thickness (related to the thickness of a single atomic layer). Further α is used in the Tauc's plot method

(18) $$\alpha E = B(E - E_g)^m,$$

which gives the relationship between the photon energy E, the independent parameter B and the optical band gap E_g.[157] The photon energy is calculated from the wavelength λ of the incident beam according to the well-known relation

(19) $$E = \frac{h \cdot c}{\lambda}$$

In the case of ZnO which is a direct gap semiconductor m is set to ½.[157] By rearranging equation (19) one gets the following relation:

(20) $$(\alpha E)^2 = B^2E - B^2E_g.$$

With this $(\alpha E)^2$ can be plotted against E. The linear part can then be extrapolated and its intercept with the x-axis gives the approximated value of the band gap E_g. Therefore, one can calculate E_g from the datapoints of the linear segment with:

(21) $$E_g = \frac{b}{m}.$$

Here *b* is the y-axis intercept and *m* the slope of the extrapolated straight segment of the graph.
All DRS measurements have been conducted using the *Perkin Elmer Lamba 365* UV/Vis spectrometer. It was equipped with 50 mm *transmission/reflectance sphere* specially designed for DRS measurements. The reflectance was measured against a white standard OP.DI.MA. (ODM98) in the spectral range from 1000 to 200 nm with a stepping of 1 or 0.5 nm.

7.1.4 Infrared Spectroscopy

The main working principle of infrared(IR) spectroscopy is the interaction of electromagnetic radiation with molecular groups while enhancing rotations and vibrations. Depending on the use case IR light with wavenumbers between 10 and 10000 cm^{-1} is utilized. For the characterization of heterogeneous catalysts, the mid-IR region (200–4000 cm^{-1}) is most important, as vibrational transitions of (organic) molecules are excited by electromagnetic radiation in this spectral region. In heterogeneous catalysis IR spectroscopy is being utilized in order to obtain information about mainly three properties of the material at hand: (i) identification of phases, (ii) identification and characterization of adsorbed organic species and (iii) identification of active sites present on the surface of the catalyst. While the first objective is achieved by direct investigation of the material, the latter two require addition of small molecules like CO_2, CO, NO etc. Through the comparison of spectra recorded of gas phase molecules with spectra of the same molecules in adsorbed state one can investigate the influence of the material surface and obtain information about its chemical properties.
The main physical principle of the IR spectroscopy is derived from Hooke's law describing the oscillation force between two spherical masses connected by a spring as a simplified model for a

diatomic molecule. The potential energy V(r) of an oscillation can then be described by adding the deviation of the interatomic distance r from the equilibrium distance r_{eq}

(22) $$V(r) = \frac{1}{2}k \cdot (r - r_{eq})^2$$

Where k is the force constant of the vibrational bond. From the solution of the Schrödinger equation the harmonic oscillator model features equidistant distinct energy levels E_n given by

(23) $$E_n = h \cdot \nu_0 \cdot \left(n + \frac{1}{2}\right), \text{ with } n = 0, 1, 2, \ldots$$

Here h is the Planck constant ($6.626 \cdot 10^{-34}$ Js) and n the vibrational quantum number describing the according energy level. The vibrational frequency ν_0 is calculated by the following equation

(24) $$\nu_0 = \frac{1}{2\pi}\sqrt{\frac{k}{\mu}}$$

Where μ is the reduced mass, which is determined from the respective masses of the atoms in the diatomic molecule

(25) $$\mu = \frac{m_1 \cdot m_2}{m_1 + m_2}$$

According to the uncertainty principle postulated by Heisenberg it is not possible to precisely determine the momentum and the position of a particle at the same time. Knowing the precise position of a particle will be always accompanied by an uncertainty of its energy. When a particle has the vibrational quantum number n = 0 it cannot have an energy equal to zero. Moreover, as the energy cannot have negative values, the total energy i.e., the sum of the kinetic and potential energy results in a value larger than zero as well. This certain energy is called the zero-point energy. As the Schrödinger equation describes the interaction between an oscillator and electromagnetic radiation it can be further utilized to deduce selection rules for vibrational transitions. For the harmonic oscillator transitions between vibration states of $\Delta n = \pm 1$ are allowed. However, this is one of the limitations of the harmonic oscillator model. While it features potential walls of infinite height allowing only finite expansion of the spring or bond, in reality a chemical bond (or spring) can be extended until it breaks and the atoms are separated from each other. Therefore, a more realistic approximation is provides by the model of the anharmonic oscillator given by the Morse potential:

(26) $$V(r) = D_e \cdot \left(1 - e^{-a \cdot (r - r_{eq})}\right)^2$$

Here D_e is the dissociation energy of the molecule and a molecule-specific constant describing the rigidity of the molecule. Further distinct energy levels are no longer equidistant and transitions over several states are possible, which result in the selection rule for transitions in an anharmonic oscillator $\Delta n = \pm 1, 2, 3,..$ Additionally, with increasing vibrational quantum number the energy

difference between vibrational states decreases. The probability of a transition decreases as well with increasing Δn.

While in Raman spectroscopy a general selection rule for the detection of a vibration is a change of polarizability of the molecule during vibration, in IR spectroscopy change of the dipole moment is required. Thus, homoatomic molecules like N_2 or O_2 cannot be detected by IR spectroscopy.

7.1.4.1 Diffuse reflectance infrared Fourier-transform spectroscopy (DRIFTS)

While IR measurements of solid materials are often conducted in transmission mode with previously prepared pellets, there are some limitations to this technique. The thickness of the pellet must be adjusted in order to assure a transmission of the IR beam through the sample. Some materials, however, might feature higher IR absorption properties resulting in not sufficient signal intensity reaching the detector. Further, to avoid scattering events the size of the solid particles must be smaller than the wavelength of the incident light. Diffuse reflectance infrared Fourier-transform spectroscopy (DRIFTS) offers an attractive alternative. Besides the fact that no pellets need to be prepared it also offers the possibility of comparatively simple *in situ* measurements. Depending on the texture and nature of the powdered sample several overlapping events may occur during the irradiation: (i) absorption, (ii) transmission, (iii) diffraction or reflection. While in this work the events of absorption and reflection are both of major importance, only the processes occurring during reflection are being outlined here in detail. For more information on absorption of IR light through the (semiconductor)material and the resulting effects please refer to chapter 2.2.5 and chapter 2.5.4.

In general, the incoming IR beam may undergo two different kinds of reflection on powdered samples: (i) direct or regular reflection and (ii) diffuse reflection. Direct reflection interacts with the sample to a very low degree so the evanescent IR beam carries hardly any information about the sample and may result in artefacts or shifts as well as distortions of features in the IR spectrum having a negative effect on the resolution of the IR spectrum. Diffuse reflection, on the other hand, intrudes the sample interacting with it via absorption, transmission, and reflection. It contains sufficient amount of information about the surface (and bulk material close to surface) of the sample and is thus most useful for analytical purposes. Since the presence of direct reflection during a measurement is inevitable special measurement geometries have been developed to minimize its influence. Consequently, diffuse reflectance measurements with small contribution of direct reflectance result in similar spectra to transmission measurements.

While in transmission and absorbance mode UV/Vis and FT-IR spectroscopy offer the possibility of quantitative analysis of the sample, with DRIFTS (and DRS) it is not possible. Similar to DRS (Chapter 7.1.3.1) the Lambert-Beer law is not applicable for DRIFTS. While Kubelka Munk theory

is being utilized for the evaluation of DRS data, for DRIFTS measurements the function log(1/R) was found to be more appropriate. It shows higher proportionality regarding concentration and thus offers some possibility of quantitative evaluation.

All FT-IR measurements were performed on the Nicolet iS50r Advanced FT-IR spectrometer manufactured by Thermo Scientific. It is equipped with a Polaris^{TM} high stability, long lifetime mid-IR source, a KBr beamguide, and a liquid nitrogen cooled MTC-A detector allowing measurements in the range from 12 000 to 400 cm^{-1} with a resolution of down to 0.125 cm^{-1}.

7.1.5 Scanning electron microscopy

Due to the resolution limitations of regular light microscopy the characterization of material structures with nanometer scaled morphology, different approaches are needed. Scanning electron microscopy (SEM) relies on the interaction of a beam of focused high-energy electrons with the surface of the material. As electrons are decelerated on the surface of the sample, different events may occur such as creation of secondary electrons, normal or diffracted backscattering of electrons, emission of X-ray or visible light photons and finally emission of heat. Each of these events is utilized solely or combined in different measurement techniques to characterize numerous properties of the sample including crystalline structure, orientation, and chemical composition. Secondary and backscattered electrons are commonly used to reveal the morphology and topography of the material as well as contrast in multiphase samples, respectively. Mostly data is recorded over a certain area of the sample surface and depicted as a two-dimensional image showing variations of properties mentioned above. Depending on the equipment areas up to 5 μm can be imaged and a resolution of up to 100 000x can be achieved resulting in a spatial resolution of about 10 nm.

All SEM images were recorded using the Zeiss Merlin VP compact Field Emission Scanning Electron Microscope operated at a range from 500 V to 30 kV. Utilizing different detectors such as HE-SE2, BSE, In-lensDuo SE/BSE, VPSE or Bruker Quantax X-Ray detector a resolution of down to 1 nm is possible.

7.1.6 Temperature programmed desorption

Temperature programmed desorption (TPD) belongs to the group of transient temperature-programmed measurement methods including temperature-programmed oxidation (TPO), reduction (TPR), adsorption (TPA), desorption (TPD) and surface reaction (TPSR). All methods feature mostly a constant heating rate in a specific gas stream appropriate for the applied method. In TPD a desorption of certain compound is being investigated while heating the sample. Thus, the basic principle of this method can be compared to Thermogravimetry (TG), however the

characterization is being done not by gravimetric changes, but by analysis of the effluent gas stream. Further prior to a TPD measurement, the material is brought in contact with a certain adsorbate e.g., CO, CO_2 or CH_3OH, whereby the coverage of the material might be varied. After purging the measurement or reaction chamber with an inert gas to minimize the amount of adsorbate present in the gas phase, a constant heating ramp is being applied during a constant flow of an inert gas. The evaluation of the changes in the effluent gas stream is done time-resolved by detectors like TCD, which is sensitive to changes in heat capacity, or by a separate analytical device such as Mass Spectrometer. Events like readsorption, transfer limitations and axial backmixing may disturb the measurement. However, flow optimized set-ups as well as appropriate gas flow minimize negative contribution. Therefore, the partial pressure of desorbates in effluent gas stream may be used for further calculations like desorption kinetics, as it is proportional to the desorption rate of the adsorbates.

A commercially available BelcatII by MicrocatBEL equipped with a thermal conductivity detector was utilized for preliminary TPD experiments. It is operated in atmospheric pressure offering flow regulation of up to 6 different gases at temperatures of up to 1000 °C. The recorded data was evaluated using the ChemMaster Software package. Further TPD experiments were performed in self-made set-ups which are discussed in detail in Chapter 3.1.

7.1.7 Mass spectrometry

Mass spectrometry (MS) is a powerful tool for qualitative, but also quantitative analysis of organic and inorganic compounds. It relies on the principle of separation of ionized parts of molecules by their mass-to-charge ratio (m/z) and detection of those quantitatively and qualitatively by their respective m/z and amount. Molecules (and atoms) are ionized by techniques like electron ionization (EI), electrospray ionization (ESI) or inductively coupled plasma (ICP) etc. After that the separation of accelerated ionized segments is being achieved by application of static or dynamic electric or magnetic fields. The main purpose here is to separate, and store charged segments depending on their polarities. Common separation devices or analyzers feature quadrupoles, ion traps or time-of-flight (TOF) instruments. Quadrupole separators feature zones with differently strong electric fields. This results in differently charged ions following a stable or unstable flight track depending on whether the charge of the ion match the electric field or not. With this a fast and very sensitive separation is achieved. While ion traps are mostly used for qualitative studies and structural work, for quantitative studies quadrupoles are more common choice. The detection of charged ions is achieved by multiplying the signal of incident ions using photon multipliers or

dynodes. Commonly electron multipliers, Faraday cups and scintillators are utilized for this purpose.

Mass spectrometry measurements were conducted utilizing a GAM 400 spectrometer by In Process Instruments (IPI). It is equipped with a quadrupole analyzer head including a cross beam ion source (Yttrium filament) and a SEM detector operated at 1200 V. The evaluation of collected data was done using the QuadStar 32 software package by IPI.

7.2 Supporting DRIFT spectra

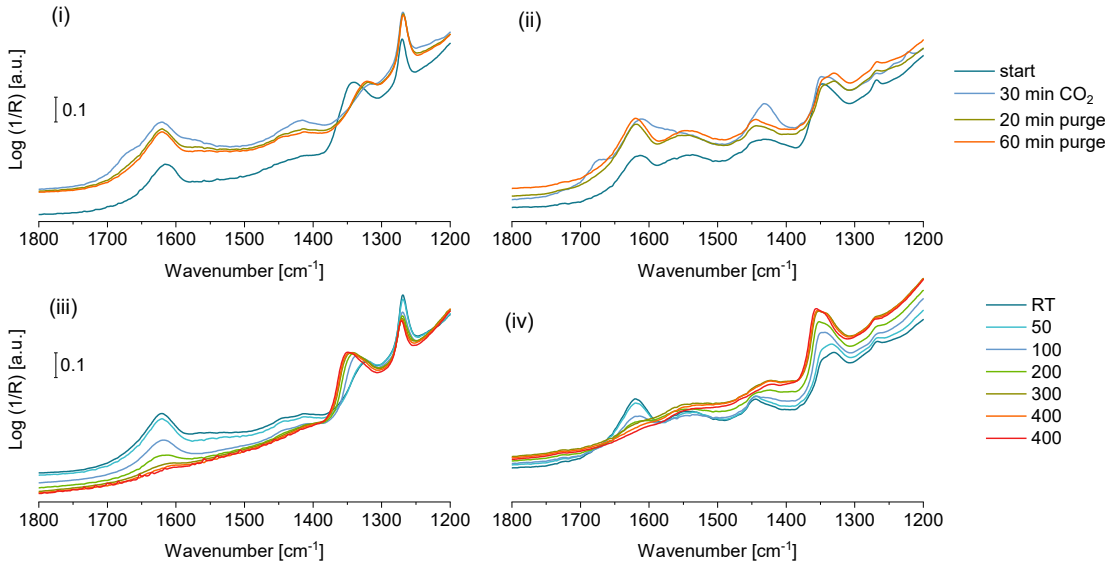

Figure A. 1: DRIFT spectra of CO_2 adsorption in dark(i) and under illumination(ii) as well as the subsequent thermal treatment(iii)(iv) of the anatase sample. The last spectra of the top depictions (red) is the first spectrum of the bottom depictions (dark teal).

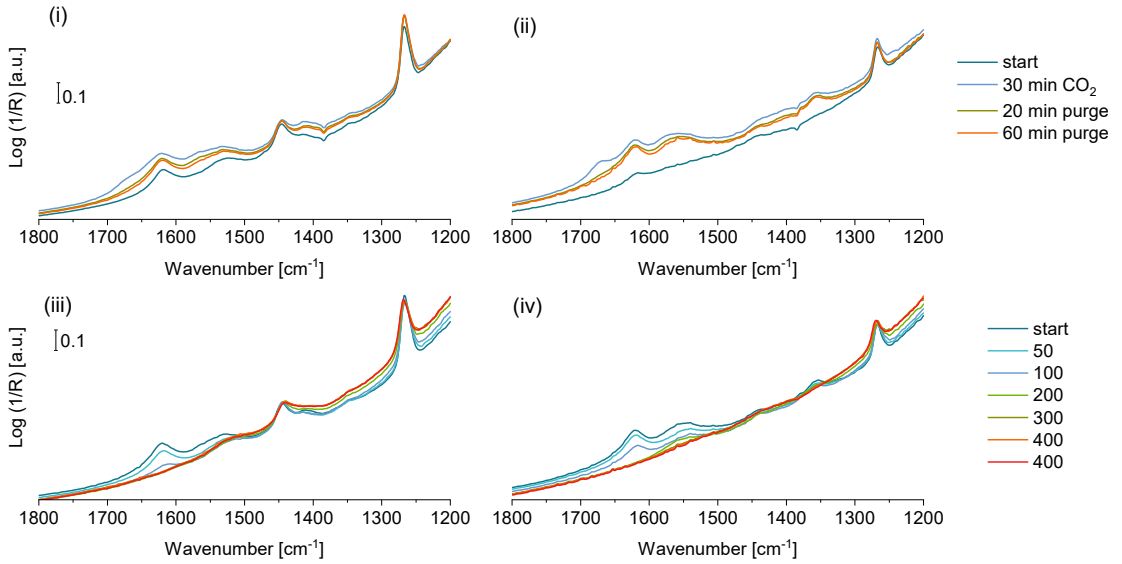

Figure A. 2: DRIFT spectra of CO_2 adsorption in dark(i) and under illumination(ii) as well as the subsequent thermal treatment(iii)(iv) of the P25 sample. The last spectrum of the top depictions (red) is the first spectrum of the bottom depictions (dark teal).

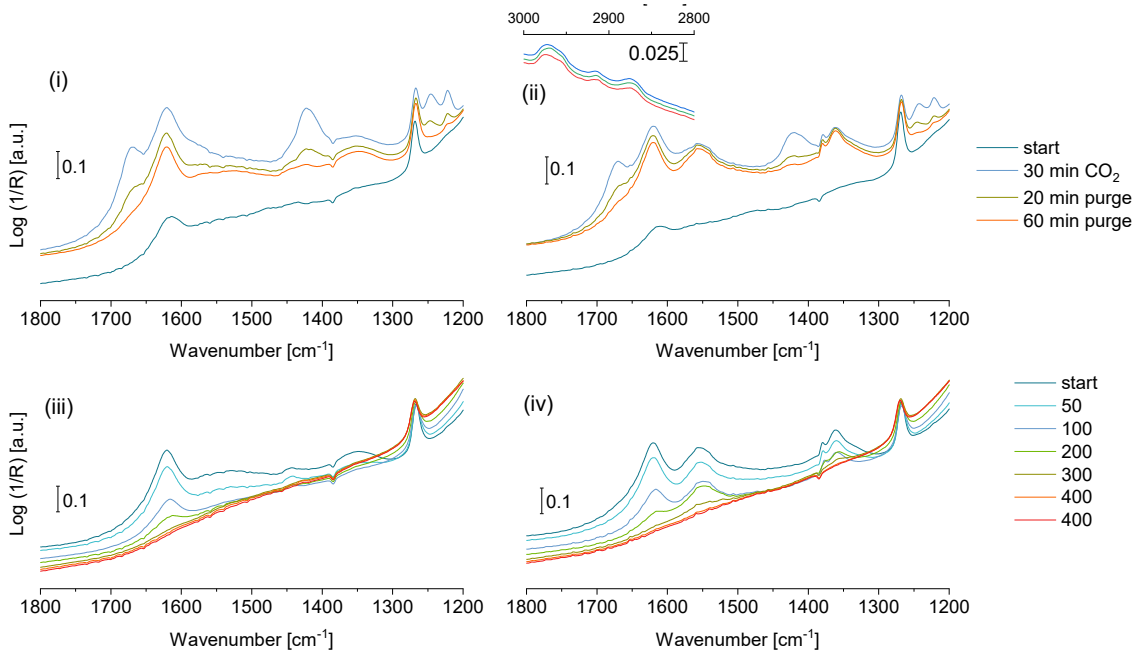

Figure A. 3: DRIFT spectra of CO_2 adsorption in dark(i) and under illumination(ii) as well as the subsequent thermal treatment(iii)(iv) of the m-TiO_2 sample. The last spectrum of the top depictions (red) is the first spectrum of the bottom depictions (dark teal).

Curriculum Vitae

Pawel Naliwajko, M. Sc.

Born on the 28th of September 1991 in Sumy, Ukrain

PhD

04/2018 – 04/2022	Leibniz Institute for Catalysis e.V. at University Rostock
	Topic: "*Influence of light on ad- and desorption processes on oxidic semiconductor surfaces*" supervised by Prof. Dr. Jennifer Strunk, Department of Heterogeneous Photocatalysis(LIKAT)

University Studies

10/2015 – 3/2018	Master of Science (Chemistry), Ruhr University Bochum
	Topic: "*Investigation of liquid-phase CO adsorption on Pd nanoparticles supported on doped TiO_2*" supervised by Prof. Dr. Martin Muhler, Department of Industrial Chemistry (RUB)
08/2016 – 12/2016	Studies in Polymer Chemistry, University of Helsinki ERASMUS, in-depth internship
	Topic: "*Synthesis of poly(glyceryl glycerol) and studies on its interactions with boronic acids*" supervised by Heikki Tenhu, Laboratory of Polymer Chemistry
11/2012 – 9/2015	Bachelor of Science (Chemistry), Ruhr University Bochum
	Topic: "*Untersuchungen zur Hydrierung von Phenylacetylen*" supervised by Prof. Dr. Martin Muhler, Department of Industrial Chemistry (RUB)
10/2010 – 10/2012	Studies in Biochemistry, Ruhr University Bochum

School

06/2010	A-Level, Lessing Gymnasium, Bochum

Scientific Contributions

Oral presentations

1. Pawel Naliwajko, Tobias Rath, Tim Peppel, Jennifer Strunk, Martin Muhler, „*Investigation of liquid-phase CO adsorption on Pd nanoparticles supported on doped TiO_2*", 2nd RoHan DAAD SDG Workshop on "*Catalysis towards Sustainable Chemical Industry*" at Hanoi University of Science and Technology, Hanoi (Vietnam), 17.– 21. September 2018
2. Pawel Naliwajko, Tim Peppel, Jennifer Strunk, „*Neue Einsichten in photokatalytische Reaktionen mittles in situ DRIFTS unter Bestrahlung*", 35. Thermo Fisher Scientific Users meeting on FT-IR and Raman in Research and Industry, Nürnberg, 26. – 27. Semptember 2018.

Poster Presentations

1. Pawel Naliwajko, Tobias Rath, Tim Peppel, Jennifer Strunk, Martin Muhler, „*Investigations on CO adsorption over Pd/TiO_2*", 21. Norddeutsches Doktorandenkolloquium (NDDK) der technischen Universität Braunschweig, Brauchschweig, 03. – 04th September 2018
2. Tobias Rath, Pawel Naliwajko, Alexander Lüken, Sascha Stürmer, Jennifer Strunk, Martin Muhler, „*CO adsorption from the gas and liquid phase on Pd/TiO_2*", 52. Jahrestreffen Deutscher Katalytiker, Weimar, 13. – 15. March 2019
3. Pawel Naliwajko, Tim Peppel, Jennifer Strunk, „*Influence of illumination with UV/Vis-light on the sorption of CO_2 on ZnO-based materials*", 7th International COnfernce on Semiconductor Photochemistry, Milano(Italy), 11. – 14. September 2019
4. Pawel Naliwajko, Tim Peppel, Jennifer Strunk, „*Influence of illumination with UV/Vis-light on the sorption of CO_2 on ZnO-based materials*", 53. Jahrestreffen Deutscher Katalytiker, Weimar(Online), 28. May 2020